EQUILIBRIUM AND DYNAMICS OF STRUCTURAL TRANSITIONS

THESIS SUBMITTED FOR THE DEGREE OF DOCTOR OF PHILOSOPHY (SCIENCE) OF THE JADAVPUR UNIVERSITY

JAYEE BHATTACHARYA
SATYENDRANATH BOSE NATIONAL CENTRE
FOR BASIC SCIENCES
BLOCK-JD, SECTOR III, SALT LAKE
KOLKATA 700 098, INDIA

2009

CERTIFICATE FROM THE SUPERVISOR(S)

This is to certify that the thesis entitled **"Equilibrium and Dynamics of Structural Transitions"** submitted by **Smt. Jayee Bhattacharya**, who got her name registered on **8th June, 2006** for the award of **Ph.D. (Science) degree** of **Jadavpur University**, is absolutely based upon her own work under the supervision of **Prof. Surajit Sengupta** and that neither this thesis nor any part of it has been submitted for either any degree/diploma or any other academic award anywhere before.

DATE :

PROF. SURAJIT SENGUPTA
SATYENDRA NATH BOSE NATIONAL
CENTRE FOR BASIC SCIENCES,
BLOCK-JD, SECTOR-III, SALT LAKE,
KOLKATA - 700098,
INDIA.

Dedicated to my parents and my son Imon

ACKNOWLEDGEMENTS

It all started in the year 2004 when my supervisor Prof. Surajit Sengupta offered me this interesting and challenging problem of microstructure selection in solid state structural transitions. This thesis is a result of about five years of work. During this period, I was accompanied by many people without whose help and support this work would not have been accomplished. Hence I take this opportunity to express my sincere gratitude towards them and thank them all.

The first person I would like to thank is my supervisor Prof. Surajit Sengupta. He was very enthusiastic and had a typical way of working out problems. He always insisted on making me think since he believed that it paved the way for my future research work. However, he was always there to listen and advise. Interactions with him were always friendly which gave me ample opportunity to express my views. He introduced me to the collaborative way of research which helped me to lift up my level of confidence and give my best. He showed me various ways to approach a research problem and insisted on staying focussed and working hard. I owe him my sincere regards for inspiring me to work and develop my interest in research. He also supported me in many difficult situations which I went through during this period. He was always there to lend out his help in any situation, be it academic and non-academic. I am really lucky to have him as my supervisor and come to know him in my life.

I would also like to express my sincere gratitude to Prof. Madan Rao for an active collaboration. I have come to know him during his visit to the S. N. Bose centre and also during my visit to NCBS, Bangalore. His integral view on research impressed me highly. Valuable discussions with him helped me a lot in conducting my research work. He was also very friendly and co-operative. I would also like to thank Prof. Srikanth Sastry of JNCASR, Bangalore. Interactions with him helped me in solving energy minimization and instantaneous normal mode problems.

I have enjoyed working with Arya Paul on the elastoplastic theory of microstructure selection. Discussions with him during the work was very helpful.

It was a pleasant experience to work with Malay Bandyopadhyay on the magnetic and caloric properties of nanoparticles. It led me to explore another area of research other than that of my thesis. I share with him many valuable moments, both scientific and non-scientific. I express my heartiest thanks to him for his neverending help and becoming a close friend of mine.

During my work at the S. N. Bose centre, I was accompanied by good friends like Abhishekda, Mukulda, Soumen, Subarna, Himadri and Tamoghna. I thank them all for their help and support.

The person without whose unconditional care and support I could not have done and completed this work is my husband Mr. Suman Sinha. He always encouraged me to work hard and go forward in acquiring my Ph.D degree. Besides being my husband, he is a friend, philosopher and guide for me.

Next I would like to express my regards for my parents Mr. Himadri Bhattacharya and Mrs. Kanak Bhattacharya. It was their dream for their daughter to pursue the research work for a Ph.D degree. I also express my gratitude for my parent-in-laws, Mr. Amaresh Sinha and Mrs. Swapna Sinha for giving me the freedom and support to do my research work successfully.

Last but not the least, I acknowledge my son Imon Sinha. He was born in May, 2008 when my first paper got published. Even at this little age he helped me to finish and complete my work undisturbed. He is too cute and God's boon to me.

List of Publications

Publications in refereed journals :

1. **Jayee Bhattacharya**, Arya Paul, Surajit Sengupta and Madan Rao.
   Non-affine deformation in microstructure selection in solids : I. Molecular dynamics.
   Journal of Physics : Condensed Matter, 20, 365210 (2008).

2. Arya Paul, **Jayee Bhattacharya**, Surajit Sengupta and Madan Rao.
   Non-affine deformation in microstructure selection in solids : II. Elastoplastic theory for the dynamics of solid state transformations.
   Journal of Physics : Condensed. Matter, 20, 365211 (2008).

3. **Jayee Bhattacharya**, Surajit Sengupta and Madan Rao.
   Non-affine deformations and shape recovery in solids undergoing martensitic transformations in two dimensions.
   Journal of Statistical Mechanics: Theory and experiment, P06003 (2008).

4. Malay Bandyopadhyay and **Jayee Bhattacharya**.
   Magnetic and caloric properties of superparamagnetic particles: An equilibrium study
   Journal of Physics : Condensed Matter, 18, 11309 (2006).

Preprints :

1. Surajit Sengupta, **Jayee Bhattacharya** and Madan Rao.
   Space-time approach to microstructure selection in solid-solid transitions.
   To be submitted to Proc. Natl. Acad. Sci. U.S. A.

ABSTRACT

Structural transitions in solids have always generated interest among physicists and material scientists. Most properties of cyrstals are closely related to the crystal structure and bonding. During structural transitions such equilibrium properties of cyrstalline solids may change abruptly as a control parameter (e.g temperature) is tuned leading to many possible technological applications. Even more useful perhaps is the dynamics of such structural changes. In solids, the diffusion of atoms is slow and this generates a variety of interesting long-lived metastable states with useful properties.

In this thesis, we make a detailed study of such metastable states and microstructures for a simple square to rhombus structural transition in model two-dimensional systems. We use molecular dynamics simulations of a series of model systems to obtain the equilibrium phase diagram and the thermodynamic parameters. Once the equilibrium properties of these systems are well established, we carry out dynamical studies by quenching from one phase to the other and watching the development of the microstructure. We classify metastable states using several dynamical and structural criteria.

One of the results of our study is that we show that there exist atleast two well-defined, distinct dynamical states, which we identify as the *ferrite* and the *Martensite* borrowing terminology from the physical metallurgy of steels. The ferrite state consists of rounded isotropic grains and exists at high temperature where there is considerable atomic diffusion, whereas at low temperature we obtain a Martensitic microstructure consisting of anisotropic grains consisting of aligned crystallites sharing a twin boundary. These distinct dynamical states are separated by a well-defined boundary in a dynamical phase diagram.

We attempt to understand this dynamical transition in terms of dynamical variables that we define in our simulations. These variables are related to the amount of non-affineness or irreversible plastic flow involved while creating regions of the product phase within the matrix of the parent. This non-affine field remains confined to the parent product interface and determines the structure of the growing grain of product. We look at the detailed time evolution of this and related fields which we define using the trajectories of the particles available from our simulations. We obtain numerical evidence that the dynamics of these fields is related to structural properties of the growing product nucleus.

Lastly, we attempt to understand the phenomenon of shape memory by simulating a model two-dimensional solid undergoing a structural transition using free boundary con-

ditions where there is a possibility of a coupling between the external characteristics of the grain and its microstructure. We monitor the external shape change of the system as the structural change progresses and classify the various dynamical states that arise as the temperature and other external parameters are changed.

Contents

Chapter 1

Introduction

1.1 Structural transitions in solids

Materials science deals with the intimate relation between structure and properties. Materials exhibit structures at many different length scales [1, 2]. Hence it is essential to identify the length scale when referring to structure and properties. Structural phase transitions [2, 3] observed in solids have attracted great deal of interest for over a century, both for their conceptual importance as symmetry-changing phase transitions and also for their role in inducing technologically useful properties in materials. During solid state structural transitions materials respond to external stimuli which alters the underlying microstructures [1]. Our main focus is to study such microstructures and microstructural changes. We analyze the temporal evolution of these microstructures from a theoretical perspective.

The importance of microstructures lies in the fact that for many features of materials, certain properties are not intrinsic. For instance both the yield strength and fracture toughness of a material depend upon its internal constitution. Hence the measured material response might depend on microstructural features such as the grain size, the porosity, etc. Depending on the extent to which the material has been subjected to prior working and annealing *i.e.* the thermomechanical history, properties ranging from the yield strength to the thermal and electrical conductivity can be varied considerably. Microstuctual features such as grain boundaries, dislocations, point defects can alter the macroscopic properties of a material. Therefore the analysis of structure is a prerequisite to understanding properties.

The richness of the microstructures that result due to various thermomechanical pro-

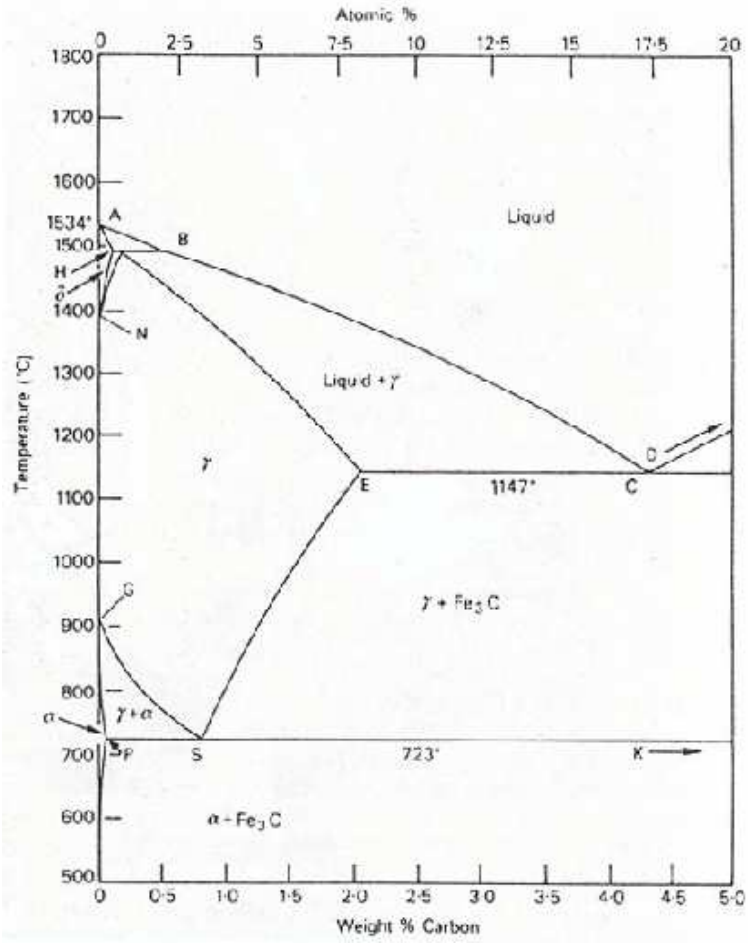

Figure 1.1: Phase diagram for the iron-carbon system.

cessing histories is illustrated from the example of steel. Figure 1.1 shows the equilibrium phase diagram for the iron-carbon system. At temperatures below roughly $720°C$, the equilibrium constitution of an $Fe - C$ alloy in the low carbon concentration limit is a two-phase alloy consisting of both $\alpha - Fe$ (ferrite in the bcc structure) and Fe_3C. This description reveals about the crystal structures present. The microstructure that attends the presence of these structures is termed as pearlite and consists of alternating plates of $\alpha - Fe$ and Fe_3C. Each phase boundary in the phase diagram seperates distinct structural outcomes. Also, there are a wide variety of metastable microstructures that can be

attained which feature the different phases revealed in the phase diagram.

1.2 Nonequilibrium structures in solids

Nonequilibrium or metastable microstructures in solids are obtained due to fast quench across a freezing or structural transition. The determination of the final microstructure of the solid under changes of temperature or pressure is a complex phenomena. A dense and rigid solid finds it difficult to flow along its free energy landscape and settle into a unique equilibrium structural configuration. Solids often get stuck in long-lived metastable or jammed states because the energy barriers that are requied to be surmounted in order to get unstuck are much larger than k_BT. The microstructures obtained as a result of quenching from the liquid phase across a freezing transition are different from those obtained from cooling from the solid state across a structural transition in a way that the latter appears to be nongeneric and dependent on details of processing history.
A particular example of such nonequilibrium solid-solid transformations are "Martensites". Martensitic transitions [4] illustrates a rich variety of temperature/stress induced microtextures [5, 6]. A martensitic transformation is a nonequilibrium solid state structural transition from the parent austenite phase to the metastable martensite consisting of alternating twinned arrays. It is observed that alloys such as $FePd$ and $NiTi$, that also show shape memory effect [7], transform on cooling from a higher symmetry phase "austenite" through "tweed" textures, to equal width mesoscale "twins" below a transition temperature. Martensites are commercially important as the hard constituent in steel or in shape memory alloys like Nitinol. The properties of these materials depend on the amount of transformed martensite.

1.2.1 Types of nonequilibrium solid state microstructures

Metallurgical studies has helped to classify some of the more generic nonequilibrium microstructures obtained from parent to the product depending on the kind of shape change and the mobility of atoms. Some of them are,

- *Martensites* - are obtained as a result of solid state transformations involving shear and no atomic transformation. Thus the transformations are distinctive since they occur in a diffusionless manner, also termed as displacive transformation. Martensites are found in a wide variety of alloys, polymeric solids and ceramics. They exhibit plate-like structures built from twinned variants of the product.

- *Polycrystalline ferrite* - of the product phase is obtained from a slower quench across a structural transition. It shows macroscopic regions of ordered configurations of atoms seperated by grain boundaries.

- *Pearlites* - are an eutectic mixture of bcc Fe (ferrite) and carbide consisting of alternating stripes in steels.

- *Bainites* - represent a structure similar to martensites, but in addition possess a small concentration of impurities *e.g.* carbon in iron which diffuses and preferentially dissolves in the parent phase.

- *Widmanstätten ferrites* - are formed due to structural transformations involving shape changes and are accompanied by short-range atomic diffusion.

- *Amorphous alloys* - are produced as a result of fast quenches and typically possess some short-range ordering of atoms.

1.3 Types of solid state transformations

Solid-solid structural transformations give rise to various microstructures which are obtained either by the phenomena of diffusion or in a diffusionless manner.

1.3.1 Diffusive transformation

Many processes in materials are mediated by diffusion in which mass is transported from one part of the material to another. When viewed from the atomic scale, these diffusive processes may be seen as a conspiratorial effect resulting from the repeated microscopic hopping of particles over time. Diffusion is an atomic level process. It is characterized

by the jiggling motion of atoms within their local energy wells, now and then punctuated by substansive motions from one well on the potential energy surface to another. The sum total of these motions constitutes what is macroscopically observed as diffusion. An example of solid-solid structural transtion resulting due to diffusive transformation is the formation of ferrite. As the temperature is reduced, Fe with less than $0.02\%C$ undergoes an equilibrium structural transition from the fcc austenite to the bcc ferrite at a temperature of $910°C$. However, the diffusion which occurs in a transforming solid is fundamentally different from that occuring in, say, particles or molecules in a fluid medium.

1.3.2 Diffusionless transformation

Diffusionless transformations are those in which the atoms undergo only local rearrangements while preserving the same distribution of near neighbours. A characteristic of this type of transformation is that the velocity of the transformation front is much larger than typical diffusion speeds of atoms. A well-known example of such transformations is the formation of martensite from the austenite phase in steel. On nucleation, martensite plates grow rapidly with a constant front velocity of the order of 10^5 cm/s, comparable to the speed of sound. Similar transformations occur in other intermetallic systems such as the cubic-tetragonal transformation in the $Ni - Al$ system and the cubic-orthorhombic transformation in the $Al - Cu - Ni$ system.

1.4 Time-temperature-transformation curves

As observed, the morphology of a solid depends on the dynamics across a solid-solid transformation. Over the years, various empirical [4, 8] and theoretical [9, 10, 11, 12] studies regarding the kinetics of these transformations have been done. A convenient representation extensively used by metallurgists is the time-temperature-transformation or TTT diagram [13]. The TTT diagram (fig. 1.2) is a family of curves parametrized by the fraction δ_{frac} of the transformed product. Each curve is a plot of the time required to obtain δ_{frac} versus temperature of the quench. The TTT curves of an alloy of fixed composition may be regarded as a kinetic phase diagram and helps to determine the heat

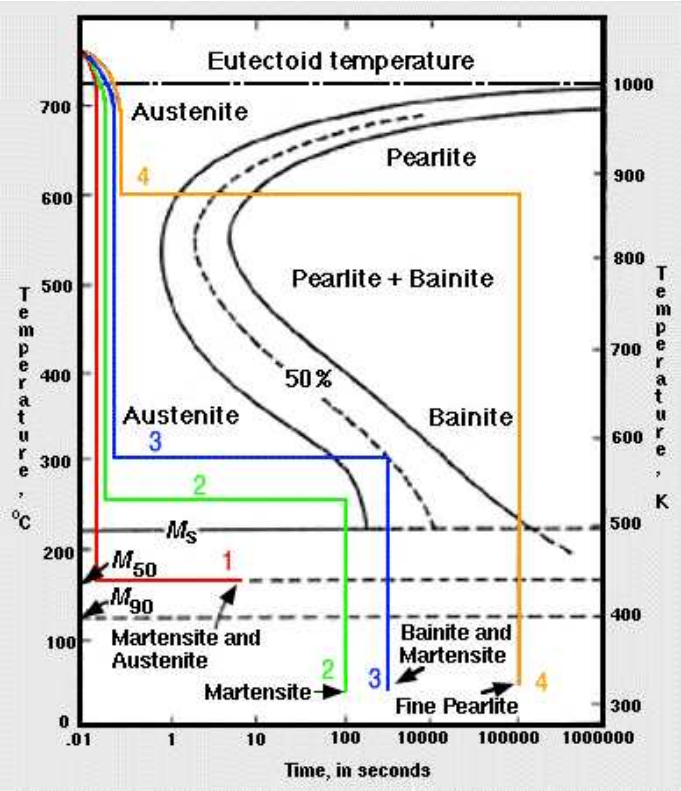

Figure 1.2: A typical Time-temperature transformation graph for steel showing several microstructural phases.

treatment schedules. Starting from a hot alloy at $t = 0$ which is equilibrated above the transition temperature, it is possible to avoid the nose of the curve and go directly into the martensitic region depending on the rate of quenching. When cooled slowly it is possible to obtain a mixture of ferrite and carbide. The quench rate is determined from the slope of the line $T(t)$.

It is clear from fig. 1.2 that the shape of the curves are qualitatively different for the ferrite and the martensite products. There are two important features regarding the TTT curves for martensites. They are,

(1) The transformation curves lie below a temperature T_{MS} called the "martensite start" temperature. This implies that martensites are not obtained at temperatures above T_{MS} even if the quench rates are infinitely high.

(2) The curves are horizontal *i.e.* parallel to the time axis. This means that the martensitic

transformation is completed immediately following the quench. Such martensites are called *athermal* martensites.

These curves have been obtained empirically in the absence of a unified nonequilibrium theory for both the martensite and ferrite nucleation. The curves were later derived within the first passage time formalism [14] using the mode-coupling theory [15] for the morphology and nucleation kinetics of the equilibrium ferrite and twinned martensite.

The other curves in the TTT family correspond to the transformation of a fixed amount of the product. This requires a detailed knowledge of the dynamics of patterning generated by the nucleation and growth of grains [16, 17, 18], together with the shape and size of the individual grains.

1.5 Need for a more complete theory: Unification & intermediate structures

Considering the facts provided in the prior studies, we observe that several qualitative features of the kinetics and morphology of microstructures are common to a wide variety of materials. This implies that there must be a set of general principles underlying such nonequilibrium solid-solid structural transformations. Since most of the solid state microstructures are featured at length scales ranging from 100 angstrom to 100μm, it seems reasonable to describe the phenomenon at the mesoscopic scale where the solid is treated as a continuum. Such coarse-grained theories are based on symmetry principles, conservation laws and broken symmetry.

In this thesis, we concentrate on the structural and dynamical features of a class of solid-solid transformations where two types of microstructures, namely "*Martensites*" and "*Ferrite*", are obtained from the parent austenite depending on the depth and rate of quenching. Because of its commercial importance, martensitic transformations [4, 19] are a well studied field in metallurgy and materials science. The work mainly deals with the phenomenology of nucleation and growth of martensite and ferrite microstructures highlighting the generic features that need to be explained by a nonequilibrium theory of solid state transformations.

The problem in its simplest form is described as follows. Consider a solid state phase

diagram (fig. 1.3) exihibiting two different equilibrium cystalline phases seperated by a first order boundary. An adiabatically slow quenching schedule from $T_{initial} \rightarrow T_{final}$

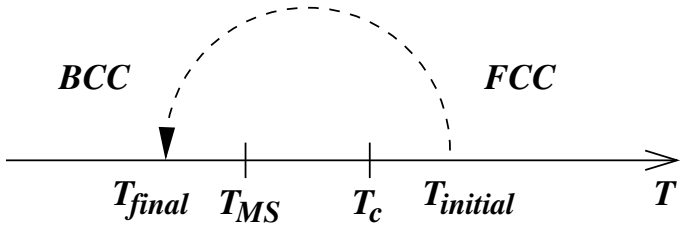

Figure 1.3: A schematic representation of the $Fe - C$ phase diagram showing the structural transition from the fcc to the bcc phase. $T_{initial}$ and T_{final} are the initial and final temperatures for the transformation. T_c is the transition temperature and T_{MS} is the *martensite start* temperature.

across the phase boundary where the cooling rate is so small that at any instant of time, the solid is in equilibrium corresponding to the instantaneous temperature, results in an equilibrium final product at T_{final}. Referring back to the $Fe - C$ phase diagram, this transformation from the fcc austenite nucleates a grain of the ferrite which grows isotropically leading to a polycrystalline bcc solid. On the other hand, an instantaneous quench across the transition temperature *i.e* from $T_{initial} > T_c \rightarrow T_{final} < T_{MS} < T_c$ results in a metastable product bearing some specific relation to the parent phase. With reference to the $Fe - C$ phase diagram this rapidly transformed phase is the martensite microstructure which is formed preempting the formation of the equilibrium ferrite phase. Again at intermediate temperatures, the mechanism of formation of both types of microstructure proceeds in such a fashion that it operates either at different regions of the sample or at the same region at different times. Such a phenomena gives rise to intermediate structures in materials. Hence a unified understanding of solid state nucleation of the different morphological structures in the product phase is neccesary. The task is to develop a comprehensive theory of solid state transformations regarding nucleation and microstructure selection. It should essentially relate the nature of the final arrested state and the dynamics leading to it to the type of structural change, the quench rate and the mobility of atoms.

1.5.1 Microcrostructure in martensites

The characteristic feature of a martensitic transformation is the microstructure it produces. In a typical transformation, the high temperature austenite phase has greater crystallographic symmetry than the low temperature martensite phase. This gives rise to multiple symmetry-related variants of martensite. The variants thus obtained form complex patterns at a length scale much smaller than the size of the specimen. Electron

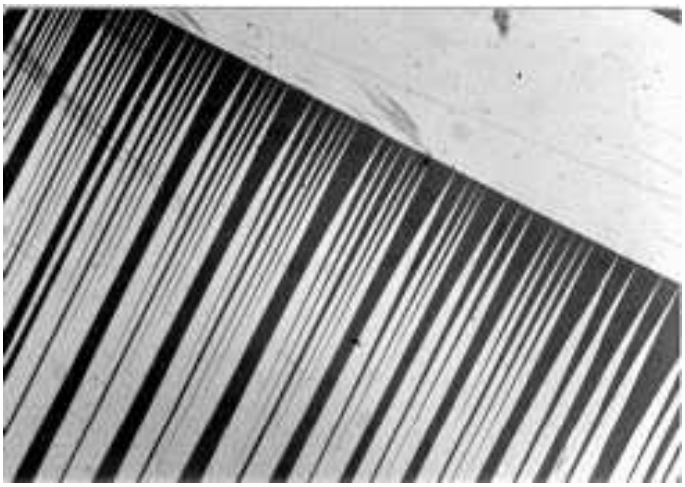

Figure 1.4: Fine structure at martensite interface. The alternating light and dark regions correspond to different variants seperated by twin boundaries.

microscopy reveals (fig. 1.4) that each plate consists of an alternating array of twinned or slipped bcc regions of size ≈ 100 angstrom. These are known as acicular martensites. The plates grow to a size of about $1\mu m$ before they collde with other plates and stop. Since the amount of martensite nucleated at any temperature is independent of time, there is always some retained fcc partitioned by the martensite plates. Optical micrographs reveal that the jammed plates lie along specific directions called habit planes. Martensites formed from such jammed plates are long lived since the elastic energy barriers for reorganizaion are much larger than $k_B T$. These microstructure endows the material with its properties. In a martensitic microstructure there is a partnership between the different variants and the parent phase as well. This is illustrated in fig. 1.5, which depicts a transformation between the cubic parent (austenite) to the tetragonal product (martensite).

It shows the presence of multiple degenerate realizations of the product martensite. This

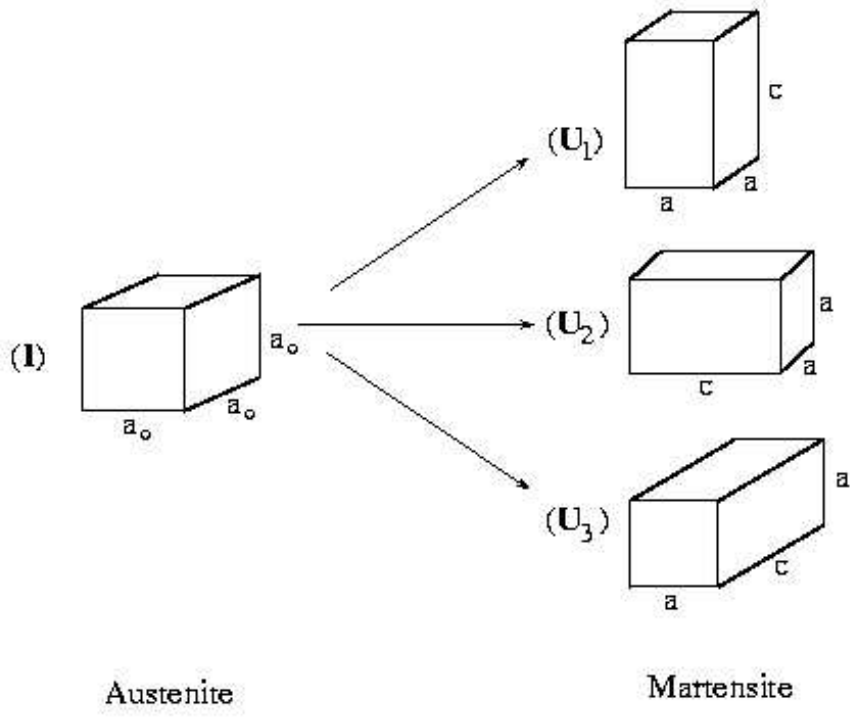

Figure 1.5: The three variants of martensite in a cubic to tetragonal transformation. U_1, U_2 and U_3 are the matrices that map the original cubic Bravais lattice into the three tetragonal variants.

degeneracy arises because of the fact that any of the choices of the original cubic axes serves, by symmetry, as an appropriate axis along which the tetragonal distortion might be done. The transformation matrices which map the original Bravais lattice vectors onto the transformed Bravais lattice vector are denoted by U_1, U_2 and U_3. The coexistence of these variants results in the richness of structures at the microstructure level.

Fig. 1.6 is a schematic representation of the symmetries present in the energy landscape. Considering an affine deformation characterized by the deformation gradient $\mathbf{F}$, the nature of the energy landscape $\mathbf{E}(F, T)$ is analysed on the basis of the known transformation strains and the invariances implied by crystal symmetry and overall rotational symmetry.

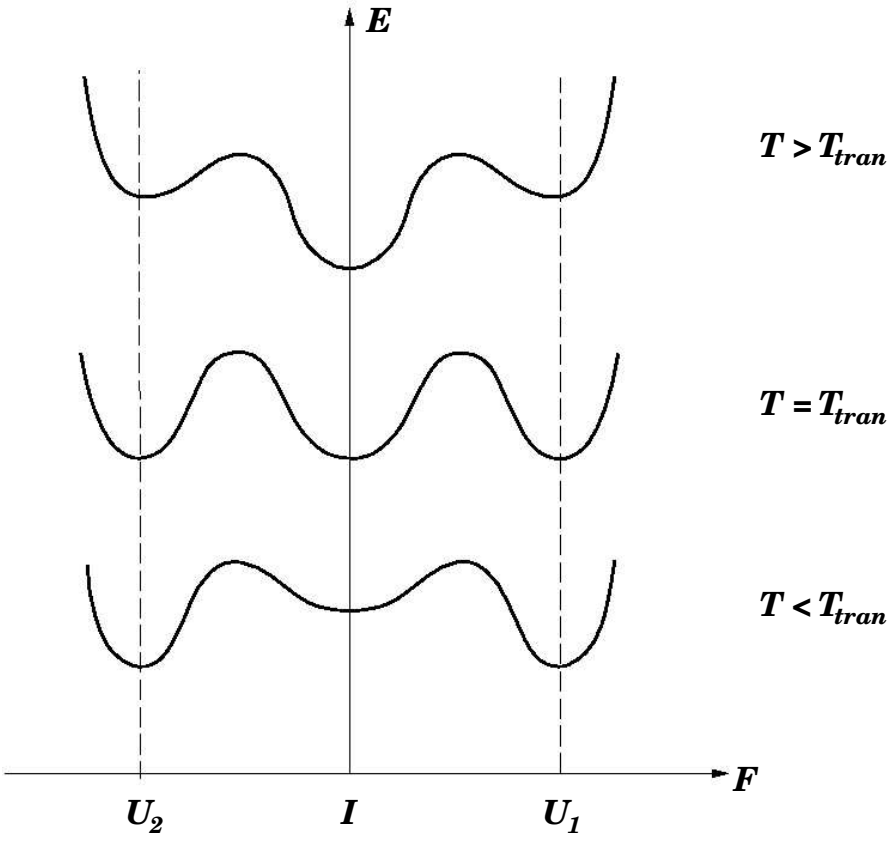

Figure 1.6: Schematic representation of the energy density $\mathbf{E}(F,T)$ for the martensitic transformation as a function of temperature. U_1 and U_2 are the deformation gradients associated with the two martensite variants while the identity $\mathbf{I}$ is associated with the austenite.

It can be evaluated through microscopic calculations. At high temperatures, the energy density is characterized by a global minimum denoting the austenite as the most stable structure *i.e.* $\mathbf{F} = \mathbf{I}$. Below the transition temperature $T = T_{tran}$, there are a number of degenerate wells corresponding to the different variants of martensite *i.e.* $\mathbf{F} = \mathbf{U_i}$. Therefore the energy density satisfies the following:

$$\begin{aligned} \mathbf{E}(\mathbf{I},T) &\leq \mathbf{E}(\mathbf{F},T) && T > T_{tran} \\ \mathbf{E}(\mathbf{I},T_{tran}) = \mathbf{E}(\mathbf{U}_i,T_{tran}) &\leq \mathbf{E}(\mathbf{F},T_{tran}) && T = T_{tran} \\ \mathbf{E}(\mathbf{U}_i,T) &\leq \mathbf{E}(\mathbf{F},T) && T < T_{tran} \end{aligned}$$

Thus the existence of microstructures is the presence of multiple wells in the energy landscape. It is the degeneracy of different martensitic variants that makes it possible for one region of the microstructure to have selected one variant and some other region to have selected another. Alloys like $In-Tl$, $In-Pb$ and $Mn-Fe$ are the simplest examples of martensitic transformations with only two twin variants.

1.5.2 Bain or Transformation matrix

A martensitic phase transformation is a first order, diffusionless, solid to solid transformation. The lattice has one structure at high temperature and a different structure at low temperature obtained as a result of a sudden deformation. Geometrically, a martensite results from the requirement that the product structure is obtainable from the parent lattice of the austenite at any time t using a locally affine transformation given by ;

$$\mathbf{R}' = \mathbf{T}(\mathbf{R}, t)\mathbf{R} \tag{1.1}$$

where $\mathbf{R}$ and $\mathbf{R}'$ are lattice vectors in the parent and product structures respectively. The matrix $\mathbf{T}$ is called the Bain or transfromation matrix. Typically, both the lattice vectors depend on temperature T as a consequence of thermal expansion. However thermal expansion is much smaller than the distortion due to transformation in the range of temperatures considered. An example of the structural tranformation is shown in fig. 1.7 where $Cu-Al-Ni$ undergoes a cubic to orthorhombic transformation. $Cu-Al-Ni$ is an ordered lattice having an fcc cubic structure in the austenite state and bcc orthorhombic in the martensite state.

A theoretical analysis of the dynamics of the martensitic transformation in $Fe-C$ is complicated because of the presence of three dimensional Bain strain deformation with three twin variants of the bcc phase. $In-Tl$ alloys undergo a tetragonal to ortghorhombic transformation when cooled below $72°C$. The orthorhombic structure is obtained from the tetragonal structure by using a two dimensional transformation matrix. This essentially relates to a square to rhombus transition. Experimental verification reveals that all along the kinetic pathway, the local configurations are obtained from the two dimensional deformation of the tetragonal parent lattice. This implies that the movement atoms are highly anisotropic and confined to the $ab-$plane with no variation along the $c-$axis.

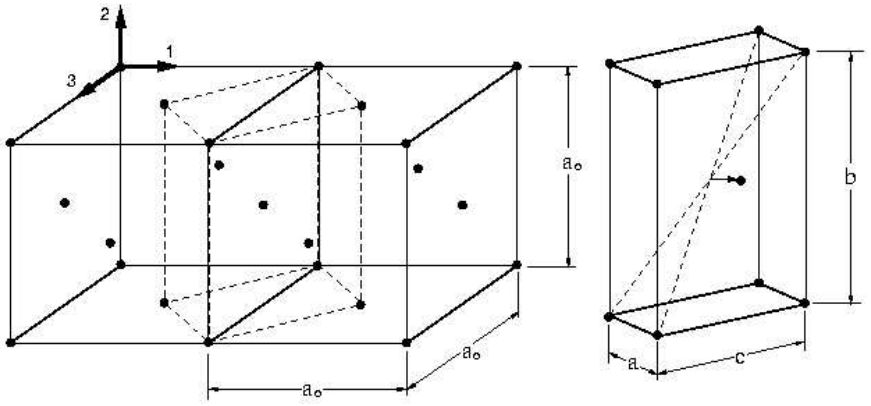

Figure 1.7: The martensitic transformation in $Cu - Al - Ni$ takes the cubic austenite lattice on the left to the orthorhombic martensite on the right.

In this thesis we discuss solid-solid structural transformation for the square to rhombic lattice transformations in two dimensions in a model system.

1.5.3 Elastic compatibility and twinning

The emergence of the microstructures in martensites are related with kinematic constraints. It determines the types of interfaces between the austenite and martensite as well as between different variants of the martensite itself. Considering the deformation shown in fig. 1.8, the regions Ω_1 and Ω_2 of the same solid are sheared in different ways by the deformation gradients $\mathbf{F}$ and $\mathbf{G}$ respectively. The transformed body remains unbroken with the straight line in the reference configuration becoming kinked after deformation. Although the deformation is continuous, the deformation gradient (strains) jumps across the interface. The existence of such invariant planes result in coherent interfaces. However, since the body remains unbroken, the jump in the deformation gradient across the surface cannot be arbitrary. Therefore, following [3], the physical requirement for the coherent interface such that the transformation on the plane obtained from both $\mathbf{F}$ and $\mathbf{G}$ gives the same result needs to satisfy the following condition:

$$\mathbf{F} - \mathbf{G} = \mathbf{a} \otimes \hat{\mathbf{n}} \tag{1.2}$$

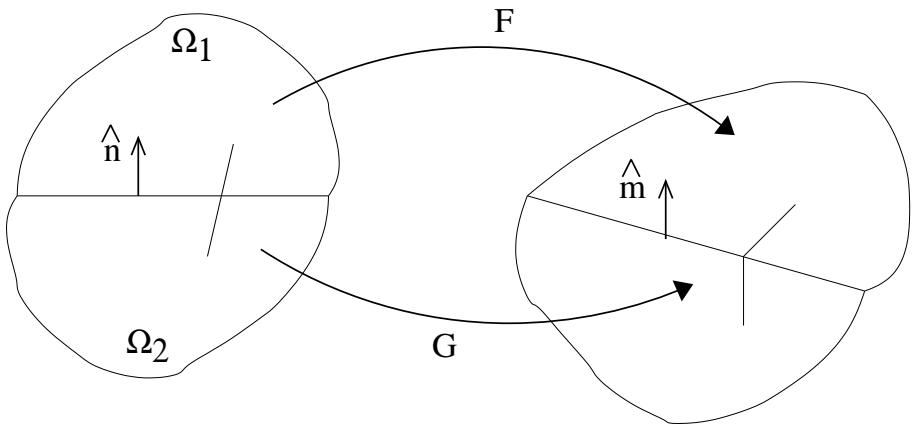

Figure 1.8: Illustration of the deformation satisfying the kinematic rank-one compatibility condition. **F** and **G** are the deformation gradients, Ω_1, Ω_2 are two distinct parts of the solid and $\hat{n}, \hat{m}$ are the reference normal vectors. Equivalently, it depicts that coherent interfaces require the satisfaction of an invariant plane condition.

where $\hat{\mathbf{n}}$ is the normal to the putative invariant plane in the reference configuration and $\mathbf{a}$ is a vector to be determined. Eqn. 1.2 is known as Hadamard jump condition or kinematic compatibility condition. In fig. 1.9 (a), the deformation in the I^{th} martensite variant is $\mathbf{Q_I U_I}$ whereas in the J^{th} variant it is $\mathbf{Q_J U_J}$ for constant rotations $\mathbf{Q_I}$ and $\mathbf{Q_J}$. Therefore, the elastic rank-one compatibility condition is written as:

$$\mathbf{Q_I U_I} - \mathbf{Q_J U_J} = \mathbf{b} \otimes \hat{\mathbf{n}} \tag{1.3}$$

where $\mathbf{b}$ is a vector and $\hat{\mathbf{n}}$ is the normal to the interfacial plane in the reference configuration. Multiplying eqn. 1.3 by $\mathbf{Q_J^T}$ and setting $\mathbf{Q_t} = \mathbf{Q_J^T Q_I}$ and $\mathbf{a} = \mathbf{Q_J^T b}$ we get,

$$\mathbf{Q_t U_I} - \mathbf{U_J} = \mathbf{a} \otimes \hat{\mathbf{n}} \tag{1.4}$$

Eqn. 1.4 is the "twinning equation". A twin is interpreted as a visible coherent interface satisfying the following :
(1)the lattice on one side can be obtained by a simple shear of the lattice on the other,
(2) the lattice on one side can also be obtained by a rotation of the lattice on the other.
The solution of the twinning equation [20] is obtained by solving the matrix $\mathbf{C_t} = \mathbf{U_J^{-T} U_I^T U_I U_J^{-1}}$. If $\mathbf{C_t} = \mathbf{I}$, then there is no solution. If $\mathbf{C_t} \neq \mathbf{I}$, then the eigenvalues are $\lambda_t^i, i = 1, 2, 3$ for

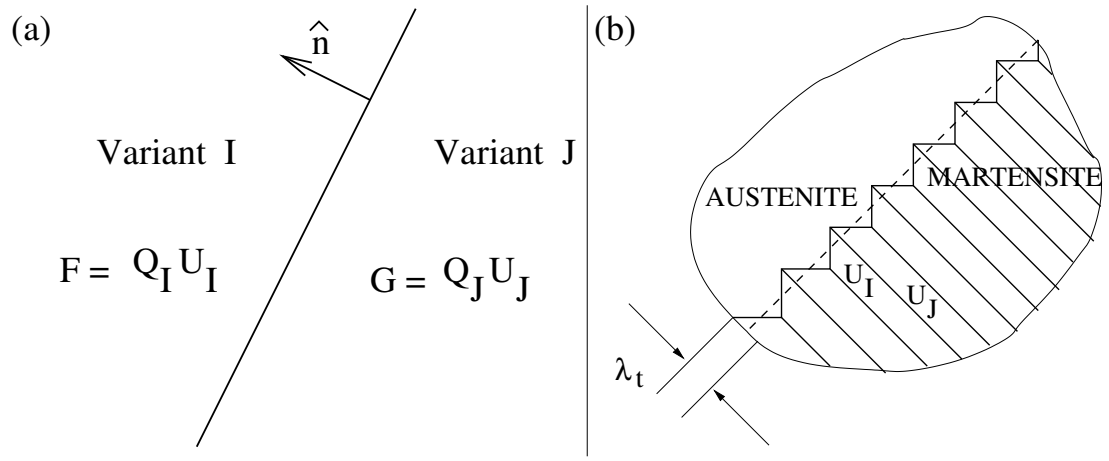

Figure 1.9: (a)Illustration of deformation with two variants or a twin. $\hat{\mathbf{n}}$ is normal to the interface between structures characterized by deformation gradients $\mathbf{F} = \mathbf{Q_I U_I}$ and $\mathbf{G} = \mathbf{Q_J U_J}$. (b) The planar interface (dashed line) between the austenite and martensite for variants $\mathbf{U_I}$ and $\mathbf{U_J}$ produced as a result of the affine transformations $\mathbf{T}$ and $\mathbf{T}'$ respectively. Elastic compatibility is restored at the interface when the atomic coordinates implied by this diagram are coarse grained over distances of order of λ_t, the width of the twin variants.

$\lambda_t^1 \leq \lambda_t^2 \leq \lambda_t^3$. Eqn. 1.4 has a solution if and only if $\lambda_t^1 \leq 1, \lambda_t^2 = 1$ and $\lambda_t^3 \geq 1$. In such conditions, there are exactly two solutions given by ;

$$\mathbf{a} = c_t \left(\sqrt{\frac{\lambda_t^3(1-\lambda_t^1)}{\lambda_t^3 - \lambda_t^1}} \hat{\mathbf{e}}_\mathbf{1} \pm \sqrt{\frac{\lambda_t^1(\lambda_t^3 - 1)}{\lambda_t^3 - \lambda_t^1}} \hat{\mathbf{e}}_\mathbf{3} \right) \tag{1.5}$$

$$\hat{\mathbf{n}} = \frac{\sqrt{\lambda_t^3} - \sqrt{\lambda_t^1}}{c_t \sqrt{\lambda_t^3 - \lambda_t^1}} \left(-\sqrt{1-\lambda_t^1} \mathbf{U_J^T} \hat{\mathbf{e}}_\mathbf{1} \pm \sqrt{\lambda_t^3 - 1} \mathbf{U_J^T} \hat{\mathbf{e}}_\mathbf{3} \right) \tag{1.6}$$

where $c_t \neq 0$ such that $|\hat{n}| = 1$ and $\hat{\mathbf{e}}_\mathbf{i}$ are the eigenvectors of $\mathbf{C_t}$ corresponding to the eigenvalues $\lambda_t^i, i = 1, 2, 3$. The rotation $\mathbf{Q_t}$ is obtained by substituting $\mathbf{a}, \hat{\mathbf{n}}$ in eqn. 1.4. There are various types of twins *e. g.* parallel twins, zig-zag twins and crossing twins.

1.5.4 Geometrical theory of Martensite

The constraint that the martensite product smoothly develops from the parent austenite requires that they coexist on either side of a locally planar interface. This relates to

the rank one compatibility condition which is usually impossible to satisfy by any single affine transformation. It is possible to obtain an approximate planar interface when two or more degenerate variants of the transformation are used (fig. 1.9 (b)). The interface in such cases possess average rank one compatibility [19, 21]. Crystallographic theories of martensite microstructure list all possible interfaces of average rank one compatibility or invariant plane strain. At distances smaller than λ_t (fig. 1.9 (b)), the interface is not planar. Hence at such scales, the transformed region is in general not obtainable by an affine transformation of the parent. Therefore, from their very nature, geometrical theories cannot predict anything about the dynamical evolution of the microstructure.

1.5.5 Strain-only theories

A parallel approach to the study of martensitic microstructures was initiated by Barsch and Krumhansl [9, 22] and further developed by other authors [10, 11, 23, 24, 25, 26, 27]. They proposed a dynamical theory which describes the martensite microstructure resulting from the minimization of a non-linear, coarse-grained, elastic free energy functional. A component of the elastic strain tensor is used as the order parameter distinguishing the parent and the product. The driving force for the nucleation of martensite from the austenite is derived from the same free energy functional written in terms of a dynamical elastic strain tensor. The free energy functional supports several degenerate minima corresponding to the different variants of the product. Unlike the geometrical theories, these strain-only theories impose "exact elastic compatibility" at "all space and time" restricting the elastic displacements to smooth, single valued functions. This local constraint automatically disallows all configurations with defects and regions of plasticity and assumes that the transformation is affine over all length and time scales. Integrating out the degrees of freedom corresponding to those components of strains which are not involved in the transformation, introduces non-local interactions between regions with different variants of the product, leading to complex twinned microstructure.

The constraint of exact elastic compatibilty at all space and time is an additional externally imposed restriction on the space of allowed configurations. Hence the transforming solid has no choice but to be a martensite. Thus there are several drawbacks of the strain-only theories. First, the transformation regions are inevitably accompanied by local and

transient regions of plastic deformation [4]. Experimental micrographs of the interfcae between the austenite and the martensite do not show evidence for elastic compatibility over all length scales [28, 29, 30]. Only average compatibility as prescribed by crystallographic theories are observed. Secondly, among the number of configurations of atomic coordinates connecting the austenite and martensite lattices, only a small fraction correspond to those which are affine over all length and time scales. The critical nucleation time scales are of the order of tens of picoseconds. It is unlikely that over this time interval, the atoms in the vicinity of the transformation front have sufficient time to select out such configurations, even if they are of low energy. Thirdly, such strain-only theories are, almost by definition, incapable of describing the dynamics of ferrite or a host of other microstructures wth intermediate charasteristics where non-affine transformations are involved. Elastic compatibility, and only on the average, should emerge from a dynamical theory unifying the nucleation and growth of a martensite and ferrite.
Thus a proper theory of microstructure selection must include the dynamical effects of non-affine distortions of the parent lattice.

1.6 Plan of the thesis

In this thesis, we have developed a dynamical theory of microstructure selection in solid state transformations which include non-affine deformations. The unified theory describes the nucleation and growth for the martensite, ferrite and other intermediate microstructures. The thesis is organized as follows.
We begin our study by first describing the two dimensional model system introduced earlier [31, 32, 33, 34] in chapter 2. The two dimensional system comprising of N particles interacts via an effective potential consisting of a purely repulsive two-body short ranged anisotropic potential parametrized by an anisotropy coefficient α and a three-body potential of strength v_3. The model represents a square to rhombic (triangular in case of isotropic potential *i.e* $\alpha = 0$) lattice transition. The transformation is controlled by the model parameters, density and temperature. Depending on the values of the model parameters, we obtain the sqaure or triangular lattice as the stable phase. We perform both Monte Carlo and molecular dynamics simulations using the model potential. At the

end of chapter 2, we briefly discuss these simulation methods and its applications on the model system.

Chapter 3 deals with zero temperature properties of the system. The geometry regarding the structural transition provides the transformation matrix for both the square to rhombus and triangle to square transformations. The shear strain is identified as the order parameter for the former transition while the order parameters for the latter are both the deviatoric and the shear strains. Using the transformation matrix we calculate the values of v_3 where the transition occurs and hence evaluate the zero temperature phase diagram for the system in the $v_3 - \alpha$ plane. The stability of the different phases are assured by the normal mode analysis. Lastly, in chapter 3 we describe the Landau theory for such solid state transformations.

The three dimensional phase diagram in the $\alpha - v_3 - T$ planes is evaluated in chapter 4. Using the phase diagram quenching schedules are performed at constant temperatures leading to the nucleation and growth of various microstructures inside the parent lattice. Molecular dynamics simulations helps to identify the non-affine zones (NAZs) during the solid state transformation. The dynamics of these NAZs decides the selection of microstructure. Internal stresses generated during the transformation create local NAZs beyond a stress threshold. Thus local yielding is associated with the change in the resulting microstructure. The state of these regions are reversible and the product grows as a result of sequential jamming-unjamming transitions. In chapter 5, we analyse the outcomes of the simulations and derive four phenomenological "laws" or principles of microstrucrure selection involving the interplay of both elastic (affine) and in-elastic (non-affine) strains. When the dynamics of the NAZs are slow, they are restricted to the growing interface and we obtain a martensite. On the other hand, when the dynamics is fast, the NAZs cover the entire growing nucleus and we obtain a ferrite. The four generic principles are further used to construct an elastoplastic theory of solid state transformation. The many approaches to the study of non-affine deformation include the phenomenological elastoplastic theories [35, 36] and the non-affine field theories due to Falk, Langer [37, 38, 39] and Lemaî**i**tre [40]. Central to these approaches, is the decomposition of the total strain into elastic and plastic parts. A plastic strain develops once the local stress exceeds a yield stress. The elastoplastic theory is constructed in terms

of a non-order parameter plastic strain describing the viscoplastic nature of the NAZs. It successfully describes both the ferrite and the martensite nucleation and microstructure along with a nonequilibrium phase diagram. While describing the dynamics towards a martensite microstructure, our theory reduces to a variant of the strain-only theory [22, 23, 24], when the austenite-martensite interface is coarse grained over a length scale of the order of the typical size of the NAZs. In this way, average compatibility emerges from the dynamics describing the martensite.

In chapter 6 we show that the dynamics of these NAZs is determined by an underlying space-time dynamical transition [41, 42] of individual particle trajectories. We show that this dynamical transition is a direct consequence of the change in the shape of the local free energy landscape. Further we infer that the physics of microstructure selection is related to that of jamming-unjamming in granular materials and the glass transition.

Finally, in chapter 7, we look at transitions in the overall shape of a solid undergoing a structural transformation. We show that the reversibility of this shape transition depends on the nature of the NAZs produced during the transition. We verify as well as modify a geometrical law derived in [43] determining the conditions for which shape reversibility is realized in martensites.

Chapter 2

The model system and simulation methods

2.1 Introduction

In the last chapter we have presented a short introduction to structural transitions in solids. We have shown that a solid often gets arrested in long lived metastable states with specific structural and mechanical properties depending on processing history. We have also remarked that a general theory for the formation of such arrested states or "microstructures" is lacking, especially the specific conditions which influence the selection of microstructure is not known, within a non-equlibrium, statistical mechanical framework. In order to make progress in this direction, it is necessary to perform controlled experiments and measure structural and thermodynamic quantities in microscopic detail. We believe that the level of detail necessary for the formulation of an unified understanding of microstructure selection, nucleation and growth may be obtained only from accurate "computer experiments" of model solids. In this chapter, therefore, we construct a suitable model solid which gives rise to the different microstructures or arrested states when subjected to varying transformation protocols. Next, we deal with the computational techniques *viz.* the simulation methods carried out using the two dimensinal model. Finally, we discuss the details of the simulations like the typical system sizes used and the time scales probed – with relation to real systems.

2.2 The 2D model

Atomistic modeling of alloy system showing "Martensitic" transitions are difficult because often the microscopic interactions are poorly known and/or computationally expensive to implement. Also such models, which are necessarily wedded to a particular alloy, are too specialised so that it is not practical to vary model parameters beyond strict bounds making it impossible to study the evolution of properties as the strength of the first order transition, or the transition temperature is varied at will. We believe, that there is, therefore, some use in developing intermediate level atomistic models which are general enough to mimic the behaviour of large classes of systems at the same time preserving the details of the particle trajectories.

There are many real two dimensional systems which show structural transitions. These include confined molecular and colloidal solids [44, 45, 46, 47, 48], flux lattices [49, 50, 51, 52, 53], skyrmions in fractional quantum Hall systems [54, 55, 56], magnetic colloidal particles [57] and colloids in electric fields [58, 59]. Our aim is not to mimic any of these systems in detail, but to construct a generic model which is able to describe such lattice transformations in two dimensions using a coarse-grained potential. In addition, we would like to be able to tune the jump in the order parameter strain across the transition by varying the parameters of the model potential.

Our effort is directed towards a detailed study of structural and dynamic properties of this solid through variation of the control parameters of the model which may be mapped to temperature, pressure, and/or magnetic & electric fields, etc. The model system we use shows a simple structural transition from square to rhombic (a special case of the more general *oblique*) lattices in two dimension. It is an accurate representation of the generic three dimensional tetragonal to orthorhombic transformation observed in many substances *e.g.* $In-Tl, In-Pb, Mn-Fe$ and $YBa_2Cu_3O_7$ where the essential transformation is restricted to a single plane with only two twin variants.

It is known that isotropic purely repulsive pair potentials in two dimensions stabilize a triangular lattice while a square lattice is usually stabilized by a quartic anisotropy which may result from *effective* many-body interactions mediated by several coupled microscopic degrees of freedom. The potential form is motivated to provide an effective Hamiltonian coarse grained over the more microscopic and consequently faster electronic degrees of

freedom. Following the methodology of coarse graining as given in [60, 61], we construct our effective potential for "point particle" interactions.

We consider a system of N particles confined in a two dimensional box of area L^2 with periodic boundary conditions on both directions. The particles inside interact via an effective potential which has only two distinct solid equilibrium phases *i.e.* square and rhombic. The total interaction energy [33, 34] between particles comprising our model system has specific two-body and three body interactions, *viz.*

$$V = 1/2 \sum_{i \neq j} V_2(\mathbf{r}_{ij}; \alpha) + 1/6 \sum_{i \neq j \neq k} V_3(\mathbf{r}_{ij}, \mathbf{r}_{jk}, \mathbf{r}_{ki}; v_3), \tag{2.1}$$

where $r_{ij} \equiv |\mathbf{r}_{ij}| \equiv |\mathbf{r}_j - \mathbf{r}_i|$ and $\mathbf{r}_i$ is the position vector of particle i. The factor $1/2$ ensures the interactions between distinctly different pair particles. The *anisotropic* two-body potential [34], is purely repulsive and short ranged in nature and is given by,

$$V_2(\mathbf{r}_{ij}; \alpha) = v_2 \left(\frac{\sigma_0}{r_{ij}} \right)^{12} \{1 + \alpha \cos^2 2(\theta_{ij} - \phi)\} \tag{2.2}$$

where σ_0 and v_2 set the units of length and energy respectively, α is an 'anisotropic lock-in' parameter, and $\theta_{ij} = \sin^{-1}(y_{ij}/|r_{ij}|)$ is the angle between $\mathbf{r}_{ij}$ and an arbitrary external axis (fig. 2.1). The two-body interaction favours a rhombic ground state. It yeilds a triangular lattice for $\alpha = 0$. As α increases, the anisotropy of the interaction deforms the ground state away from the triangular and towards the square lattice. The angle ϕ is the orientation of the anisotropic particles with respect to the same external axis used to measure θ_{ij} (fig. 2.1). Inclusion of the two-body anisotropic lock-in parameter α is a device to vary the jump in the order parameter (*e.g* the elastic strain connecting the square and the rhombic phases) from strongly first order ($\alpha = 0$) to a continuous transition for $v_3 = 0, \alpha \sim 1.5$. The physical justification of the anisotropy is as follows. The origin of this feature is easy to imagine once it is realized that the basic interacting entities in our model are not single atoms but motifs consisting of more than one atom. Fluctuations of ϕ therefore model internal coordinates of the basis motif (optical modes). In this work, however we consider only the case when the particles are all orientated in the same way and hence ϕ may be taken as zero without any loss of generality.

The short-ranged three-body interaction,

$$V_3(\mathbf{r}_{ij}, \mathbf{r}_{jk}, \mathbf{r}_{ki}; v_3) = v_3 \left[f_{ij} f_{jk} \sin^2 4\theta_{ijk} + f_{jk} f_{ik} \sin^2 4\theta_{jki} + f_{ik} f_{ij} \sin^2 4\theta_{kij} \right] , \tag{2.3}$$

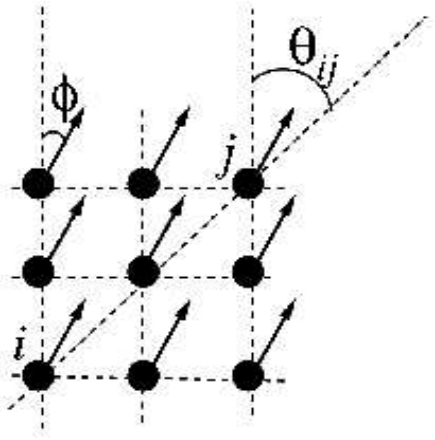

Figure 2.1: The meanings of the angles θ_{ij} and ϕ. While θ_{ij} is the angle of the position vector $\mathbf{r}_{ij}$ between the molecules i and j measured with respect to the crystal axis $\{01\}$ in the reference square lattice, ϕ is the orientation of the basis molecule measured with respect to the same axis [34].

where the function

$$\begin{aligned} f_{ij} \equiv f(r_{ij}) &= (r_{ij} - r_0)^2 \text{ for } r_{ij} < r_0 \\ &= 0 \text{ otherwise} \end{aligned}$$

The angle θ_{ijk} is the angle between the vectors $\mathbf{r}_{ij}$ and $\mathbf{r}_{jk}$ (fig. 2.2). The range is determined by r_0 which acts as the cut-off for the three-body potential. We take $r_0 = 1.8\sigma_0$ for all our calculations reported in this thesis. The three body part is designed such that for every triplet i, j, k within r_0, the bond angle θ_{ijk} gives lowest energy for $\theta_{ijk} = 0, \pi/4, \pi/2$. The three body term therefore favours a square lattice. The tuning parameters in the above microscopic model are thus v_3, α, temperature T and density $\rho = N/L^2$.

It may appear that the three body potential calculations requires a large investment in terms of computer times because one may need to take account of triplets. We show, however, in the Appendix that this is not so since, the special form for V_3 allows one to write the energy and the forces as summations over pair terms alone. Similar potentials have been used by Weber and Stillinger in [62].

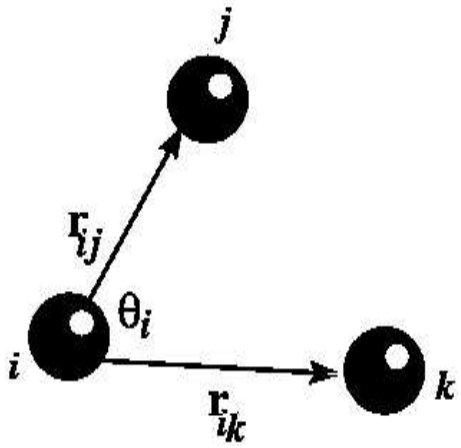

Figure 2.2: Definition of angles and distances used in the three body potential.

2.3 Simulation methods

We shall now describe briefly the computational techniques used on our specific atomistic model. We have used both Monte Carlo and molecular dynamics methods to study our model system. While the former is useful for studying equilibrium properties, the latter is needed to obtain the dynamics. As both of these methods are quite well known and established, we refer to a number of good text books available for details [63, 64, 65, 66].

2.3.1 The Monte Carlo method

To describe this method we consider a system of N particles. The classical expression for the thermal average of an observable $\mathcal{J}$ expressed as a function of coordinates, $\mathbf{r}^N$ and momenta, $\mathbf{p}^N$ is given as,

$$\langle \mathcal{J} \rangle = \frac{\int d\mathbf{p}^N \, d\mathbf{r}^N \mathcal{J}(\mathbf{p}^N, \mathbf{r}^N) \exp[-\beta \mathcal{H}(\mathbf{p}^N, \mathbf{r}^N)]}{\int d\mathbf{p}^N \, d\mathbf{r}^N \exp[-\beta \mathcal{H}(\mathbf{p}^N, \mathbf{r}^N)]} \tag{2.4}$$

where $\beta = 1/k_B T$ and k_B is the Boltzmann constant. Here $\mathbf{r}^N$ and $\mathbf{p}^N$ represent the coordinates and momenta for all N particles. The function $\mathcal{H}(\mathbf{p}^N, \mathbf{r}^N)$ is the Hamiltonian of the system comprising of the kinetic energy $\mathcal{T}$ and the potential energy $\mathcal{U}$. As $\mathcal{T}$ can be expressed as a quadratic function of the momenta the integration over momenta can be carried out analytically. The part which is a function of coordinates is difficult to

compute and can only be obtained approximately and/or numerically for most systems of interest. One such numerical technique for evaluating such thermal averages is the Monte Carlo method comprising of the Monte Carlo importance sampling algorithm introduced by Metropolis *et al* [67].

Basic Monte Carlo algorithm

The basic algorithm as proposed by Metropolis *et al* consists of the following scheme:

- Select a particle at random at a particular point $\mathbf{r}^N$ and calculate its energy $\mathcal{U}(\mathbf{r}^N)$.
- Give the particle a small random displacement Δ such that $\mathbf{r}' = \mathbf{r} + \Delta$ and again calculate its energy $\mathcal{U}(\mathbf{r}'^N)$ at the new position.
- Accept the move from $\mathbf{r}^N$ to $\mathbf{r}'^N$ with the probability,

$$acc(o \rightarrow n) = min(1, \exp\{-\beta[\mathcal{U}(\mathbf{r}'^N) - \mathcal{U}(\mathbf{r}^N)]\}) \tag{2.5}$$

Here the trial move takes the system from an old (o) configuration to a new (n) configuration. In order to make the decision that the trial move is accepted or rejected, a random number is generated. It is denoted by "$RANF$" and the random number is produced from an uniform distribution in the interval $[0, 1]$. We accept the trial move if $RANF < acc(o \rightarrow n)$ and reject it otherwise. The above rule guarantees the fact that the probability to accept a trial move from o to n is indeed equal to $acc(o \rightarrow n)$. The Monte Carlo samling process is highly dependent on the random number generator which should definitely generate numbers uniformly in the interval $[0, 1]$. We have used the random number generator $RAN2$ [68] which we have tested independently and found to be adequate for our purpose.

We make use of a such a Monte Carlo algorithm in computing the equilibrium properties of our model solid, for example the free energy calculations required to obtain the phase diagram for the system as described in chapter 4.

2.3.2 The molecular dynamics method

Unlike Monte Carlo simulations which are mainly used to study static properties, molecular dynamics simulations help to extract dynamical features of the system even when it is

driven far away from equilibrium. Basically the two methods are related by the "Ergodic Hypothesis". If we wish to compute the average of a function of coordinates and momenta of a many-particle system, we can do it by either taking the time average or the ensemble average. The former is related to the molecular dynamics approach while the latter is the Monte Carlo approach. In equilibrium, the hypothesis states that the two procedures give identical results. For systems far from equilibrium, ensemble averaging and consequently Monte Carlo simulations become meaningless although the molecular dynamics method is still applicable.

As in real experiments where we perform a series of measurements during a certain time interval and then determine the time average of these measurements, in molecular dynamics simulations we study the average behaviour of a many-particle system by computing the time evolution of the system numerically and averaging the quantity of interest over a sufficiently long time interval. Hence, the average of an observable $\mathcal{J}$ in this case is given by,

$$\overline{\mathcal{J}(r)} = Lt_{t\to\infty}\frac{1}{t}\int_0^t dt'\mathcal{J}(r,t') \tag{2.6}$$

Basic molecular dynamics algorithm

The basic molecular dynamics scheme may be described as follows:

Essentially we need to solve the following equations for all particles i,

$$\begin{aligned}\frac{d\mathbf{x_i}}{dt} &= \frac{\mathbf{p_i}}{m}\\ \frac{d\mathbf{p_i}}{dt} &= \mathbf{F_i}\end{aligned}$$

where, $\mathbf{x_i}, \mathbf{p_i}, \mathbf{F_i} = \frac{\partial \mathbf{V}(\mathbf{r^N})}{\partial \mathbf{r_i}}$ denotes the particle positions, momenta and forces respectively. These variables consists of two body and three body parts.

- First we read in the parameters that specify the conditions of the run. They can be *e.g.* number of particles, starting temperature, density, time steps, time intervals, lattice parameters, etc.

- We then assign initial positions and velocities to all particles in the system. The particle positions are chosen such that they are compatible with the specific structure that we are aiming to simulate.

- We compute the forces on all particles.

- We integrate Newton's equation of motion using a suitable scheme depending on the accuracy desired and the ensemble used. The basic steps of our simulations are in the two dimensional NAT ensemble. The integration is performed with the help of the velocity Verlet scheme [63] where the position and velocities are updated in two stages by the following equations;

$$r(t+\Delta t) = r(t) + v(t)\Delta t + \frac{1}{2m} f(t)\Delta t^2 \tag{2.7}$$

$$v(t+\frac{1}{2}\Delta t) = v(t) + \frac{1}{2m} f(t)\Delta t \tag{2.8}$$

$$v(t+\Delta t) = v(t+\frac{1}{2}\Delta t) + \frac{1}{2m} f(t+\Delta t)\Delta t \tag{2.9}$$

  The acceleration $f(t+\Delta t)$ is calculated as follows:

$$f(t+\Delta t) = -\frac{1}{m}\nabla V\left(r(t+\Delta t)\right) \tag{2.10}$$

  After getting the new positions and velocities, the energies are again evaluated. As the instantaneous temperature is calculated from the kinetic energy per particle, it is seen to fluctuate. This fluctuation is controlled by appropriate rescaling of the temperature or connecting the system to proper heat reservoirs. For our simulations we have used the Nosé-Hoover thermostat to ensure that the temperature remains fixed to within 1 part in 10^5. Computation of the forces and integration of the Newton's equations form the main part of the simulation. These are repeated until we compute the time evolution of the system for the desired length of time.

- After completion of the central loop, we compute and write out the averages of measured quantities and finally stop.

2.4 Constant temperature molecular dynamics

Our results obtained from simulations are in two dimensions and in the constant number, area (shape), and temperature (NAT) ensemble with periodic boundary conditions using a Nosé-Hoover thermostat [63]. In chapter 7 we describe some of the results obtained from

extensive simulations in the constant stress ($N\sigma T$) ensemble ($\sigma_{\alpha'\beta'}$ is the stress tensor). This is done in order to study shape reversibility in Martensites. Using an additional glue potential along with open boundaries allows for changes of overall shape of the crystal during the transformation.

The equations of motion for the particles coupled to the thermostat while performing a molecular dynamics (MD) simulation are given by,

$$\frac{d\mathbf{x_i}}{dt} = \frac{\mathbf{p_i}}{m} \tag{2.11}$$

$$\frac{d\mathbf{p_i}}{dt} = \mathbf{F_i} - \xi\mathbf{p_i} \tag{2.12}$$

$$\frac{d\xi}{dt} = \frac{2N-3}{Q}(T_{kinetic} - T) \tag{2.13}$$

where $\mathbf{x_i}$ and $\mathbf{p_i}$ are the positions and momenta of the ith particle respectively and the mass m has been taken to be unity. $\mathbf{F_i}$ is the total force acting on the ith particle due to all other particles and is derivable from the two and three body potentials. The equations of motion for upto $N = 20000$ particles are integrated using a velocity Verlet scheme [63] with a time step $\Delta t = 10^{-3}$. The relaxation time of the Nosé-Hoover thermostat Q determines how fast the system relaxes to the ambient temperature. The role of Q is such that a small value of Q corresponds to a low inertia of the heat bath and leads to rapid temperature fluctuations. A large value of Q leads to a slow, ringing response to the temperature jump. Equilibrium properties are unaffected by this parameter, which is chosen to produce fast relaxation, at the same time avoiding numerical instabilities. On the other hand, dynamical properties can be sensitive to this parameter, however, our results are robust to changes of Q within reasonable limits. The variable ξ is the thermodynamic friction coefficient and it parametrizes the coupling between the system and the heat bath. It acts as a force maintaining the kinetic temperature $T_{kinetic} = (1/N)\sum_i(p_i^2/2m)$ at the temperature T of the bath. To ensure convergence, the value of Q is chosen as 0.1. The choice of Δt for the molecular dynamics simulations using the velocity Verlet scheme along with the Nosé-Hoover thermostat is very crucial. Application of the thermostat changes the total Hamiltonian of the system from $\mathcal{H}$ to $\mathcal{H}_{Nose}$ [63] which is dependent on ξ and Q. To determine the reasonable value of Δt, we look at the conservation of both $\mathcal{H}$ and $\mathcal{H}_{Nose}$. This is done by switching off the thermostat (*i. e.* using $\xi = 0$). We find that with $\Delta t = 10^{-3}$ the Hamiltonian is conserved with an error of 10^{-6}. The unit of time is

$\sigma_0\sqrt{m/v_2}$, where m is the particle mass. Using typical values for unit particle mass, this translates to an simulation time unit *i.e.* one MD step equal to $1ps$.

We have used typical equilibrium times of order 2×10^4 MD steps and above. Our system sizes were typically of $N = 120 \times 120 = 14400$ particles. A detailed comparison of MD simulations of our model system in various conditions, starting from a variety of initial states and for the full range of the potential parameters is discussed in Chapter 5.

2.5 Appendix A

In this appendix, we reproduce the formulæ used to calculate the energy, forces and stresses for the three-body potential used. The form of the three-body potential ensures that these quantities are computable using pairwise functions alone[62]. This greatly speeds up the computation.

Energy : The three-body part of the energy is given by

$$\begin{aligned} E_3 &= \frac{1}{6}\sum_{i\neq j\neq k}\psi_3(r_{ij},r_{jk},r_{ki}) \\ &= \frac{1}{2}\sum_{i\neq j\neq k}\frac{v_3}{4}f_{ij}\sin^2(4\theta_{jik})f_{ik} \\ &= \sum_{i\neq j\neq k}2\Big(\sin^2(\theta_{jik})\cos^2(\theta_{jik}) \\ &- 4\sin^4(\theta_{jik})\cos^4(\theta_{jik})\Big)f_{ij}f_{ik}. \end{aligned} \tag{2.14}$$

Now define $\tilde{x}_{ij} = x_{ij}/r_{ij}$ and $\tilde{y}_{ij} = y_{ij}/r_{ij}$, so that $\sin\theta_{jik} = \tilde{x}_{ik}\tilde{y}_{ij} - \tilde{x}_{ij}\tilde{y}_{ik}$ and $\cos\theta_{jik} = \tilde{x}_{ij}\tilde{x}_{ik} + \tilde{y}_{ij}\tilde{y}_{ik}$. Using the above definitions and the quantities

$$\begin{aligned} g_{ij}(1) &= \tilde{x}_{ij}^2\tilde{y}_{ij}^2 f_{ij}, \\ g_{ij}(2) &= \tilde{x}_{ij}^2\tilde{y}_{ij}^2(\tilde{x}_{ij}^2 - \tilde{y}_{ij}^2)f_{ij}, \\ g_{ij}(3) &= \tilde{x}_{ij}^4\tilde{y}_{ij}^4 f_{ij}, \\ g_{ij}(4) &= \tilde{x}_{ij}^2\tilde{y}_{ij}^2(\tilde{x}_{ij}^2 - \tilde{y}_{ij}^2)^2 f_{ij}, \\ g_{ij}(5) &= \tilde{x}_{ij}^3\tilde{y}_{ij}^3(\tilde{x}_{ij}^2 - \tilde{y}_{ij}^2)f_{ij}, \end{aligned}$$

we get $E_3 = v_3\sum_i S_i$ with

$$\begin{aligned} S_i &= 4\Big[G_i(1)F_i - 4G_i(1)^2 - G_i(2)^2\Big] \\ &- 16\Big[G_i(3)F_i + 32G_i(3)^2 + 2G_i(4)^2 \\ &+ G_i(1)^2 - 16G_i(3)G_i(1) \\ &- 4G_i(5)G_i(2) + 16G_i(5)^2\Big] \end{aligned}$$

where $G_i(n) = \sum_{j\neq i} g_{ij}(n)$ and $F_i = \sum_{j\neq i} f_{ij}$.

Force: The three-body forces can be found by taking derivatives of E_3 which can be cast into similar forms. Remembering that $\tilde{y}_{ij}$ implicitly depends on x_{ij} through r_{ij} and evaluating the quantities

$$\begin{aligned}
\frac{\partial g_{ij}(1)}{\partial x_{ij}} &= 2\left[\tilde{x}_{ij}\tilde{y}_{ij}^2(1-\tilde{x}_{ij}^2)\right. \\
&- \left.\tilde{x}_{ij}^3\tilde{y}_{ij}^2\right] f_{ij}/r_{ij} \\
&+ 2\tilde{x}_{ij}^3\tilde{y}_{ij}^2(r_{ij}-r_0), \\
\frac{\partial g_{ij}(2)}{\partial x_{ij}} &= \left[(3\tilde{x}_{ij}^2\tilde{y}_{ij}-\tilde{y}_{ij}^3)(1-\tilde{x}_{ij}^2)\right. \\
&- \left.\tilde{x}_{ij}\tilde{y}_{ij}(\tilde{x}_{ij}^3-3\tilde{x}_{ij}^2\tilde{y}_{ij}^3)\right] f_{ij}/r_{ij} \\
&+ 2\tilde{x}_{ij}^2\tilde{y}_{ij}(\tilde{x}_{ij}^2-\tilde{y}_{ij}^2)(r_{ij}-r_0), \\
\frac{\partial g_{ij}(3)}{\partial x_{ij}} &= \left[4\tilde{x}_{ij}^3\tilde{y}_{ij}^4(1-\tilde{x}_{ij}^2)-4\tilde{x}_{ij}^5\tilde{y}_{ij}^4\right] f_{ij}/r_{ij} \\
&+ 2\tilde{x}_{ij}^5\tilde{y}_{ij}^4(r_{ij}-r_0), \\
\frac{\partial g_{ij}(4)}{\partial x_{ij}} &= \left[(6\tilde{x}_{ij}^5\tilde{y}_{ij}^2+2\tilde{x}_{ij}\tilde{y}_{ij}^6\right. \\
&- 8\tilde{x}_{ij}^3\tilde{y}_{ij}^4)(1-\tilde{x}_{ij}^2)-(6\tilde{y}_{ij}^5\tilde{x}_{ij}^2 \\
&+ \left.2\tilde{y}_{ij}\tilde{x}_{ij}^6-8\tilde{y}_{ij}^3\tilde{x}_{ij}^4)\tilde{x}_{ij}\tilde{y}_{ij}\right] f_{ij}/r_{ij} \\
&+ 2\tilde{x}_{ij}^3\tilde{y}_{ij}^2(\tilde{x}_{ij}^2-\tilde{y}_{ij}^2)^2(r_{ij}-r_0), \\
\frac{\partial g_{ij}(5)}{\partial x_{ij}} &= \left[(5\tilde{x}_{ij}^4\tilde{y}_{ij}^3-3\tilde{x}_{ij}^2\tilde{y}_{ij}^5)(1-\tilde{x}_{ij}^2)\right. \\
&- \left.(3\tilde{x}_{ij}^5\tilde{y}_{ij}^2-5\tilde{x}_{ij}^3\tilde{y}_{ij}^4)\right] f_{ij}/r_{ij} \\
&+ 2\tilde{x}_{ij}^4\tilde{y}_{ij}^3(\tilde{x}_{ij}^2-\tilde{y}_{ij}^2)(r_{ij}-r_0),
\end{aligned}$$

the force acting on the particle 'i' in the x-direction owing to the three-body interaction can be written as

$$F_i^x = \sum_{j\neq i} H_{ij}^x \tag{2.15}$$

where

$$H_{ij}^x = 4v_3\left[\frac{\partial g_{ij}(1)}{\partial x_{ij}}\sum_{k\neq i} f_{ik} + 2\tilde{x}_{ij}(r_{ij}-r_0)\sum_{k\neq i} g_{ik}(1)\right.$$

$$
\begin{aligned}
- \quad & 8\frac{\partial g_{ij}(1)}{\partial x_{ij}}\sum_{k\neq i} g_{ik}(1) - 2\frac{\partial g_{ij}(2)}{\partial x_{ij}}\sum_{k\neq i} g_{ik}(2)\Bigg] \\
- \quad & 16V_3\Bigg[\frac{\partial g_{ij}(3)}{\partial x_{ij}}\sum_{k\neq i} f_{ik} + 2\tilde{x}_{ij}(r_{ij}-r_0)\sum_{k\neq i} g_{ik}(3) \\
+ \quad & 64\frac{\partial g_{ij}(3)}{\partial x_{ij}}\sum_{k\neq i} g_{ik}(3) + 4\frac{\partial g_{ij}(4)}{\partial x_{ij}}\sum_{k\neq i} g_{ik}(4) \\
+ \quad & 2\frac{\partial g_{ij}(1)}{\partial x_{ij}}\sum_{k\neq i} g_{ik}(1) - 16\frac{\partial g_{ij}(1)}{\partial x_{ij}}\sum_{k\neq i} g_{ik}(3) \\
- \quad & 4\frac{\partial g_{ij}(5)}{\partial x_{ij}}\sum_{k\neq i} g_{ik}(2) - 4\frac{\partial g_{ij}(2)}{\partial x_{ij}}\sum_{k\neq i} g_{ik}(5) \\
+ \quad & 32\frac{\partial g_{ij}(5)}{\partial x_{ij}}\sum_{k\neq i} g_{ik}(5)\Bigg].
\end{aligned}
$$

Similarly, the y-component of the force

$$F_i^y = \sum_{j\neq i} H_{ij}^y, \tag{2.16}$$

where H_{ij}^y is evaluated using expressions similar to that for H_{ij}^x given above.

Finally, we give the expression for the contribution of the three-body interaction to the virial stress which, can now be calculated using the force components,

$$\sigma_{\alpha'\beta'} = \frac{1}{2}\sum_{i,j} r_{ij}^{\alpha'} H_{ij}^{\beta'} \tag{2.17}$$

where $\alpha', \beta', = x, y$. The pressure is given by

$$P = \sigma_{\alpha'\alpha'} \tag{2.18}$$

Chapter 3

Properties at zero temperature

3.1 Introduction

In the last chapter we presented, in detail a model system which undergoes a square to rhombus structural transition. Several properties of this transformation *e.g* the transition temperatures, the order parameter discontinuities etc. can be tuned at will, using the parameters of the potential. In this chapter, we obtain the properties of this model solid for vanishing temperatures. Extension to non-zero temperatures will be taken up in chapter 4.

In the next section, we begin by discussing the geometry of the square to rhombus and the triangle to square transformation. We show that the elastic strain can be used as an order parameter for these transformatiuons. The expected changes in the strains going from one structure to another is then determined. This is followed in section 3.3 with a calculation of the energetics of the transformations at $T = 0$ and a determination of the $T = 0$ phase diagram. Part of these results are from previously published work which we have included for completeness. In section 3.4 we investigate the stability of these phases using a detailed normal mode analysis. We show that both first order and continuous transitions are possible in this system depending on the choice of parameters. Finally, we show that these results can be summarized within a phenomenological Landau theory with coefficients which depend on our potentials. The form of the Landau theory is derived for each of the transitions encountered.

3.2 Structural transitions : geometry

At zero temperature, the equilibrium configuration is a solid which minimizes the potential energy V (eqn. 2.1). Geometrically, we consider the case when a product structure is obtainable from the parent lattice using an affine transformation of the form,

$$\mathbf{R}' = \mathbf{T}\mathbf{R} \tag{3.1}$$

where $\mathbf{R}$ and $\mathbf{R}'$ are lattice vectors in the parent and product structures, respectively. Here $\mathbf{T}$ is the transformation matrix given by,

$$\mathbf{T} = \begin{bmatrix} e_1/2 + e_2/2 & e_3 \\ e_3 & e_1/2 - e_2/2 \end{bmatrix} \tag{3.2}$$

The parameters e_1, e_2 and e_3 are related to the Lagrangian strain tensor components as follows. Since all distortions and energies are measured with respect to the undistorted lattice, the microscopic displacement $\mathbf{u_R}$ is given by,

$$\mathbf{u_R} = \mathbf{R}' - \mathbf{R} \tag{3.3}$$

defined at every $\mathbf{R}$. The full non-linear Lagrangian strain tensor, ϵ_{ij} [69, 70] is given as follows,

$$\epsilon_{ij} = \frac{1}{2}\left(\frac{\partial u_i}{\partial r_j} + \frac{\partial u_j}{\partial r_i} + \frac{\partial u_k}{\partial r_i}\frac{\partial u_k}{\partial r_j}\right) \tag{3.4}$$

where the indices i, j go over x, y. If non-linearities are neglected , then the parameters in eqn. 3.2 are represented as the *volumetric, deviatoric* and *shear* strains having the following definitions respectively,

$$e_1 = \epsilon_{xx} + \epsilon_{yy} \tag{3.5}$$

$$e_2 = \epsilon_{xx} - \epsilon_{yy} \tag{3.6}$$

$$e_3 = \epsilon_{xy} \tag{3.7}$$

The above strain components e_1, e_2 and e_3 characterize the general solid state structural transition.

At $T = 0$, a perfect square lattice is transformed to a perfect rhombic lattice by the transformation,

$$\mathbf{R}_R = (1 + \mathbf{T})\mathbf{R}_S \tag{3.8}$$

where $\mathbf{R}_R$ and $\mathbf{R}_S$ are the position vectors for the perfect rhombic and square lattices respectively. The square lattice can be transformed to the rhombic lattice in two different ways referring to the two variants of the transformation. The rhombic lattice is a special case of the general oblique lattice - one of the five possible two dimensional Bravais lattice [70]. In general, we need two order parameters (OP) to describe the transition between square and oblique lattices, i.e., between the space groups $p4mm \rightarrow p2$. These are the affine shear strain $e_3 = \epsilon_{xy} = \epsilon_{yx}$ and the deviatoric strain $e_2 = (\epsilon_{xx} - \epsilon_{yy})$. Thus from symmetry considerations alone, we would expect to obtain four symmetry related product phases [71]. However, the microscopic model used by us obtains a rhombic lattice for which e_2 identically vanishes and the four equivalent variants merge in pairs to give *two* symmetry related products. In addition, the density $\rho = N/A$ is a constant in the NAT ensemble. Due to the fixed density constraint, e_1 is related to e_3 as follows,

$$e_1 = \sqrt{1 + e_3^2} - 1 \approx \frac{e_3^2}{2} \tag{3.9}$$

Now, if we set the value of $e_1 = 0$, then the rhombic lattice is represented by a single order parameter e_3. The two possible variants of the rhombic phase are denoted by $\pm e_3$. The value of the sole order parameter for a perfect square is zero and it is non-zero for the rhombic lattice. Thus e_3 becomes a good order parameter representing the square to rhombic structural transition.

Finally, we consider the reverse transformation from a triangular lattice to the square lattice. The triangular phase is a special case obtained at $\alpha = 0.0$ and $v_3 = 0.0$. The symmetry group $p6$ of the triangular lattice is not a subgroup of $p2$ *i.e.* rhombic lattice. So the $p6 \rightarrow p4mm$ transformation needs to be treated separately.

In the triangular configuration, the lattice vectors are in three different directions *i.e* $\theta = 0^\circ, 120^\circ, 240^\circ$. The transformation relation for the triangle to square for $\theta = 0^\circ$ at $T = 0$ is given by,

$$\mathbf{R}_S = (1 - \mathbf{T})\mathbf{R}_T \tag{3.10}$$

$\mathbf{T}$ is the same transformation matrix as in eqn. 3.2 and $\mathbf{R}_S$ and $\mathbf{R}_T$ are the lattice vectors in the square and triangular lattices respectively. Eqn. 3.10 is obtained assuming the fact that the strains are small. Therefore for $\theta = 0^\circ, 120^\circ, 240^\circ$ we have,

$$\mathbf{R}_S = (1 - \mathbf{R_o}^{-1}\mathbf{T}\mathbf{R_o})\mathbf{R}_T \tag{3.11}$$

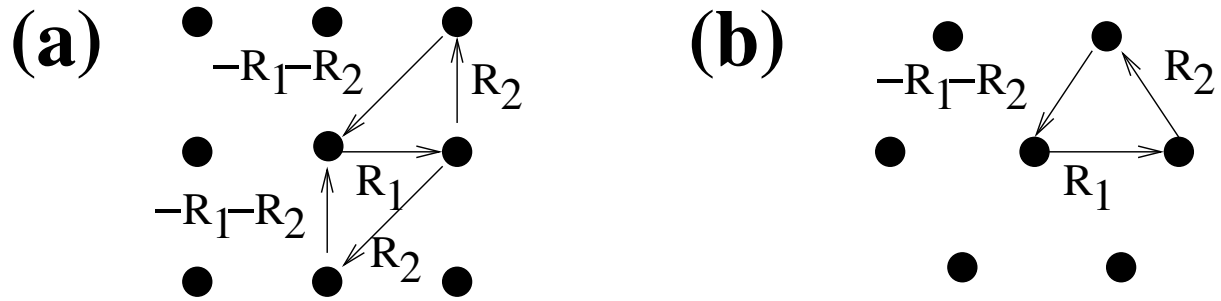

Figure 3.1: Three body interactions shown with the help of the lattice vectors for (a) square lattice and (b) triangular lattice .

where $\mathbf{R_o}$ is the rotation matrix. Hence the expanded form of eqn. 3.10 is given by,

$$\mathbf{R}_S = \begin{bmatrix} 1 - \frac{e_1}{2} - \frac{e_2}{2}\cos 2\theta + e_3 \sin 2\theta & -e_2 \sin\theta\cos\theta - e_3\cos 2\theta \\ -e_2 \sin\theta\cos\theta - e_3\cos 2\theta & 1 - \frac{e_1}{2} + \frac{e_2}{2}\cos 2\theta - e_3 \sin 2\theta \end{bmatrix} \mathbf{R}_T \tag{3.12}$$

Putting the values of θ we get three different matrices as follows,
For $\theta = 0°$,

$$M_1 = \begin{bmatrix} 1 - \frac{e_1}{2} - \frac{e_2}{2} & -e_3 \\ -e_3 & 1 - \frac{e_1}{2} + \frac{e_2}{2} \end{bmatrix} \tag{3.13}$$

For $\theta = 120°$,

$$M_2 = \begin{bmatrix} 1 - \frac{e_1}{2} + \frac{e_2}{4} - \sqrt{3}\frac{e_3}{2} & \frac{e_3}{2} + \sqrt{3}\frac{e_2}{4} \\ \frac{e_3}{2} + \sqrt{3}\frac{e_2}{4} & 1 - \frac{e_1}{2} - \frac{e_2}{4} + \sqrt{3}\frac{e_3}{2} \end{bmatrix} \tag{3.14}$$

For $\theta = 240°$,

$$M_3 = \begin{bmatrix} 1 - \frac{e_1}{2} + \frac{e_2}{4} + \sqrt{3}\frac{e_3}{2} & \frac{e_3}{2} - \sqrt{3}\frac{e_2}{4} \\ \frac{e_3}{2} - \sqrt{3}\frac{e_2}{4} & 1 - \frac{e_1}{2} - \frac{e_2}{4} - \sqrt{3}\frac{e_3}{2} \end{bmatrix} \tag{3.15}$$

The above three matrices M_1, M_2, M_3 correspond to three degenerate minimas of the energy. Considering the triangular lattice as the reference lattice, there are two order parameters required to decribe the triangle to square phase transition. The triangular phase has a higher symmetry than the square phase, there being three symmetry axes. We set $e_1' = 0$ and hence e_2' and e_3' become the two order parameters for the transition.

3.3 Structural transitions : energetics

3.3.1 Calculations at $T = 0$ with $\alpha = 0$

The energetics for both the square to rhombus and the triangle to square structural transitions at $T = 0$ are done by using the two dimensional microscopic model described in chapter 2. We first consider the square lattice as the reference configuration and deform it according to eqn. 3.8. The variation of the energy per particle with the order parameters in fig. 3.2 shows that there is a single minima at $e_3 = 0, e_2 = 0$ reperesenting the perfect square lattice and two degenerate minimas equispaced from the metastable square minima representing the two variants of the rhombic lattice obtained by deforming the square. Therefore we find that e_2 identically vanishes for the square to rhombus transition. The four equivalent variants of the oblique lattice merge in pairs to give the two symmetry related products of the rhombic lattice. The value of v_3 at which the transition takes place

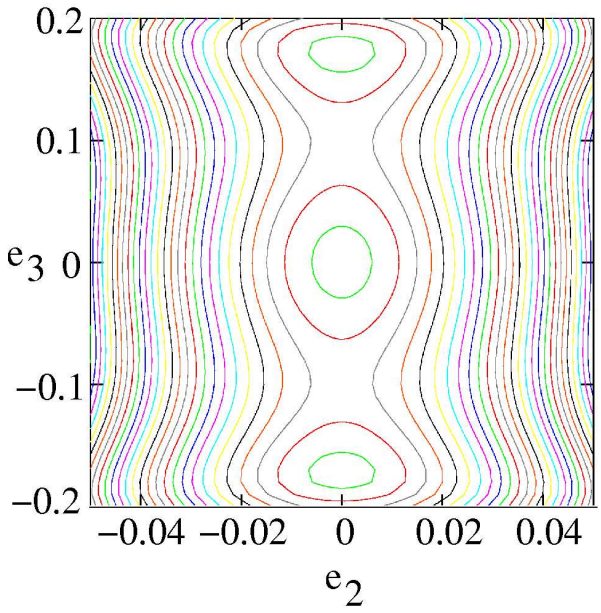

Figure 3.2: Contour plot of the zero temperature energy per particle for square to rhombus transition at $\rho = 1.05, \alpha = 0$ and $v_3 = 0.408$ as a function of the OP strains (e_2, e_3) showing a metastable square minimum at $(0, 0)$ and two degenerate, stable rhombic (*oblique*) minima at $(0, \pm 0.17)$.

for the isotropic potential ($\alpha = 0$) is 0.408. The energy per particle is plotted for various values of v_3 in fig. 3.3 below. The values of the order parameter e_3 at which the two variants of the rhombic lattice are obtained are ± 0.17. This proves that the transition is first order with the order parameter jumping discontinuously, *i.e.* $\Delta e_3 = \pm 0.17$. Referring

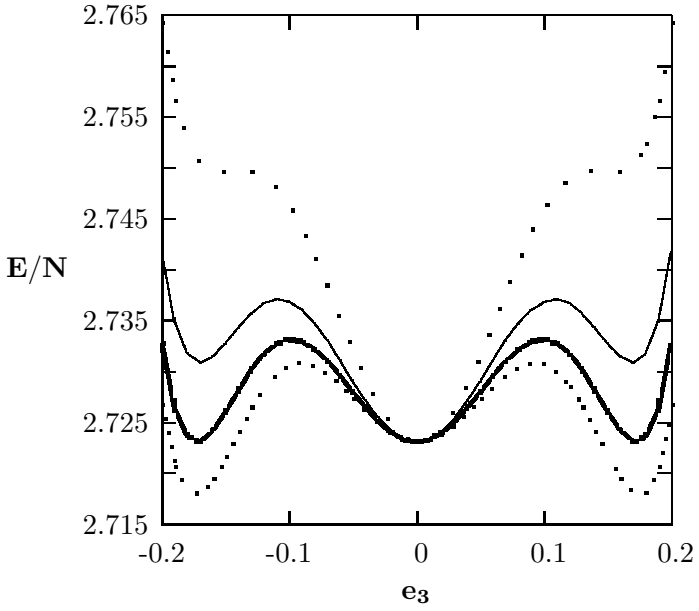

Figure 3.3: Energy per particle (E/N) for square to rhombus transition at $\rho = 1.05, \alpha = 0$ as a function of the order parameter e_3 for various values of v_3 *i.e* $v_3 = 0.4$ (densely dotted line), $v_3 = 0.408$ (thick line), $v_3 = 0.42$ (thin line) and $v_3 = 0.45$ (dotted line).

to fig. 3.3, we find that for higher values of v_3, there is a single minima at $e_3 = 0$ depicting the square lattice as the only stable phase. Decreasing v_3 gradually beyond the transition point shows two degenerate minimas depicting the rhombic lattice as the stable phase.

For the triangle to square transformation, the reference triangular lattice is subjected to the potential V in eqn. 2.1 with $\alpha = 0, \rho = 1.05$ and lattice parameter $a' = 1.0486$. There are two order parameters for the triangle to square transition *viz.* e_2' and e_3'. We set $e_1' = 0$ and measuring the strains from the triangular lattice, we find that the strain energy now has four minima (fig. 3.4). The central minima at $e_2' = e_3' = 0$ corresponds to the traingular lattice while it is surrounded by three degenerate square minima. To get the value of v_3 at which the transition takes place, we plot the energy per particle as

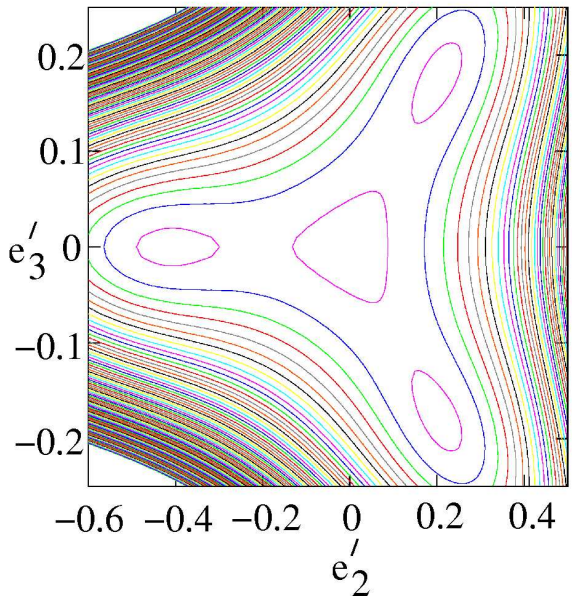

Figure 3.4: Contour plot of the energy per particle (E/N) as a function of e_2' and e_3' for triangle to square transition at $\rho = 1.05, \alpha = 0$. There is a single minima at $e_2' = e_3' = 0$ corresponding to the triangular phase and three degenerate square minimas surrounding it. The strains are now calculated from the triangular phase and the transition takes place at $v_3 = 3.034$.

a function of e_2' (fig. 3.5). As we increase v_3, the minimum corresponding to the square phase becomes stable. The transition takes place at $v_3 = 3.034$ where the two minima are at the same value of E/N.

We also compute the static properties like pressure and elastic moduli considering the triangular lattice as the reference lattice. This can be done by evaluating the derivatives of energy to its appropriate power. In the NAT ensemble with constant density $\rho = 1.05$, pressure is defined as $P = \sigma_1 = \partial E/\partial e_1'$. But for the triangle to square transition $e_1' = 0$. Note that we deal with a repulsive system and it is always under a hydrostatic pressure. Hence we calculate pressure for such transitions from the slope of the curve showing the variation of energy with density. Therefore,

$$P = \frac{\partial E}{\partial \rho} \tag{3.16}$$

Evaluating the slope at $\rho = 1.05$ gives the pressure at a particular density. Fig. 3.6 (a)

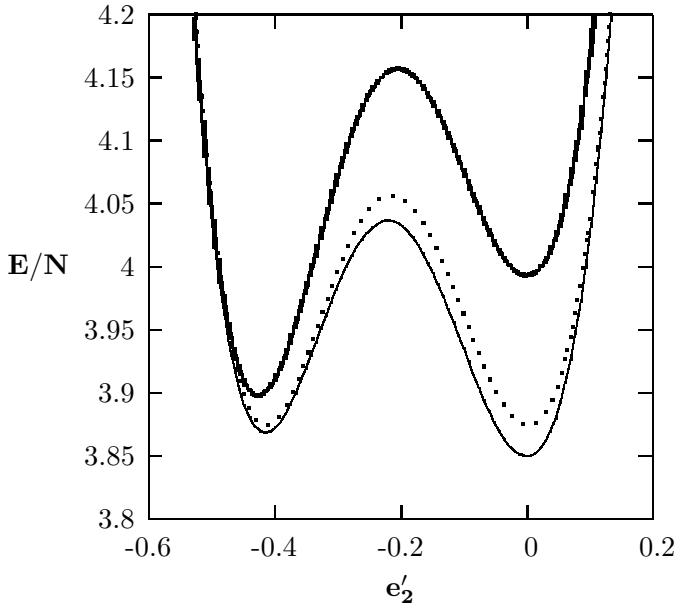

Figure 3.5: Energy per particle (E/N) for triangle to square structural transition at $\rho = 1.05, \alpha = 0$ as a function of the order parameter e_2' for various values of v_3 *i.e* $v_3 = 3.0$ (thin line), $v_3 = 3.034$ (dotted line), $v_3 = 3.2$ (thick line).

shows the variation of P with v_3 at $\rho = 1.05$. Pressure increases with the increase in v_3 for the triangular lattice. The bulk modulus is related to the pressure as $\mathcal{K} = \rho(\frac{\partial \mathcal{P}}{\partial \rho})$. As P is already known from the slope, $\mathcal{K}$ is obtained from the expression,

$$\mathcal{K} = \rho(\frac{\partial^2 E}{\partial \rho^2}) \tag{3.17}$$

The plot of the variation in $\mathcal{K}$ with v_3 is shown in fig. 3.6 (b). We find that $\mathcal{K}$ also increases with increasing v_3. The effective shear modulus for the triangular solid is defined as $\mu = C_{33} + P$ with $C_{33} = \partial^2 E/\partial {e_3'}^2$. When μ is plotted against v_3, (fig. 3.6 (c)), we find that there is a change of sign from positive to negative values as v_3 is increased for the triangular lattice during the transformation. All the above behaviour of $P, \mathcal{K}$ and μ accounts for the fact that the triangular lattice is unstable at high values of v_3. Negative values of μ supports the unstability.

Similar calculations for pressure P, bulk modulus $\mathcal{K}$ and effective shear modulus μ for the square to rhombus structural transition has been described in detals in [34]. We include them here for the sake of completeness. Fig. 3.7 shows the variation of the above

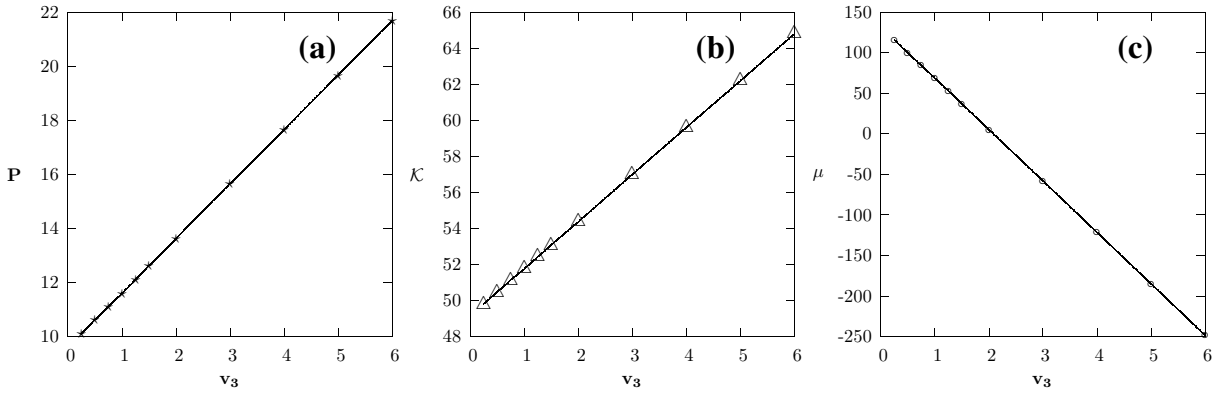

Figure 3.6: Variation of pressure P (a), bulk modulus $\mathcal{K}$ (b) and shear modulus μ (c) with the three body potential parameter v_3. The reference lattice is a perfect triangle at $T = 0, \rho = 1.05$ and $\alpha = 0$. Pressure and bulk modulus show positive increase in their values with the increase in v_3 while the shear modulus goes from positive to negative values with a similar increase in v_3.

mentioned static quantities as a function of the order parameter strain e_3.

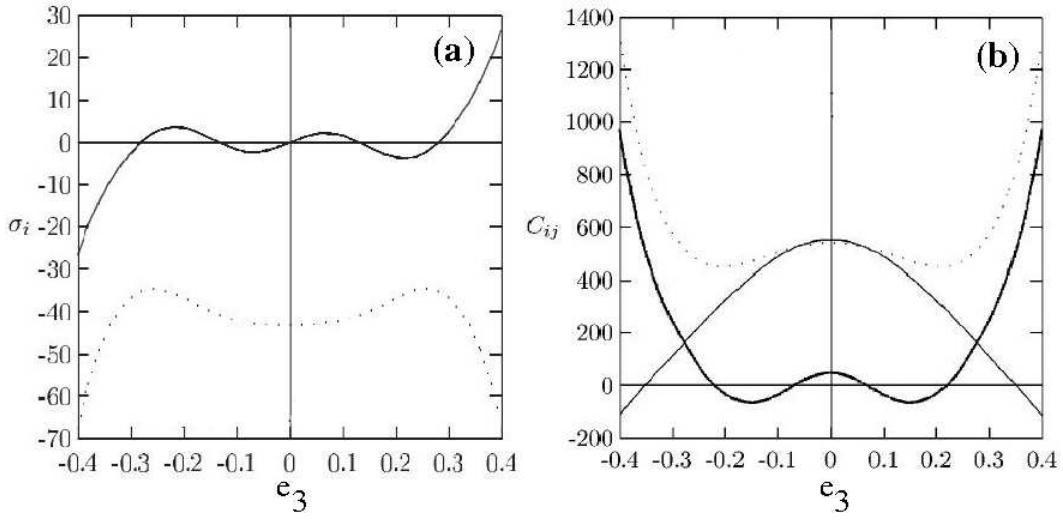

Figure 3.7: Plots for the square to rhombus transition from [34] showing (a) the pressure $P = \sigma_1$ (dotted line) and the effective shear stress $\partial E/\partial e_3 = \sigma_3 + Pe_3$ (solid line) as a function of e_3 for $\rho = 1.1$ and $v_3 = 1.5$; (b) the second order elastic moduli C_{11} (bulk) (dotted line), C_{22} (thin line) and $C_{33} + P$ (thick line) as a function of e_3 for $\rho = 1.1$ and $v_3 = 1.5$. Note that for the triangular lattice, $C_{22} = C_{33} + P$ as required by symmetry.

3.3.2 Calculations at $T = 0$ with $\alpha \neq 0$

Exploring the range of potential parameters we now consider the case when the anisotropy parameter α has a non-zero value. When $\alpha = 0$, the product rhombic lattice is close to being triangular, corresponding to a strongly first order structural transition with a large jump in the order parameter with $\Delta e_3 = \pm.24$ for $\rho = 1.1$ (fig. 3.8) and a relatively large volume change [33, 34]. However comparing the results with experiments on real

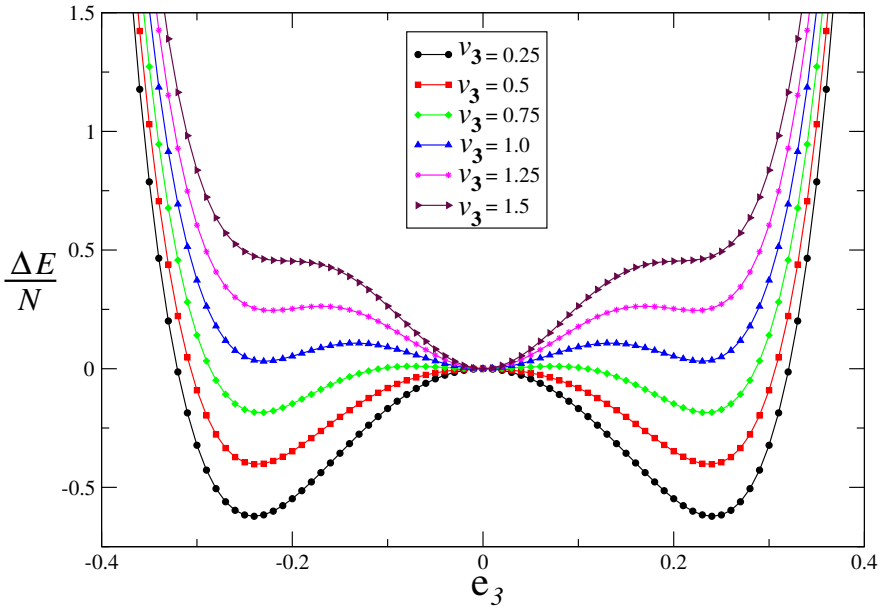

Figure 3.8: Energy difference per particle ($\Delta E/N$) as a function of the shear strain for the structural transition at $\rho = 1.1, \alpha = 0$ for various values of v_3. The transition from the square to triangle (rhombic) takes place at $v_3 = 0.964$ and the two degenerate minimas lie at $e_3 = \pm 0.24$.

systems, we find that there is an anomaly. Most solids undergoing a typical tetragonal to orthorhombic structural transition *viz.* $YBa_2Cu_3O_7$, have a complex basis with several atoms per unit cell. In such cases the jump in the shear strain at the transition point is much smaller compared to the Δe_3 obtained.

A possible qualitative discrepancy between the model with $\alpha = 0$ and real systems is that changes in temperature or pressure (hydrostatic or chemical) might lead to a local

structural rearrangement (optical modes) coupling to the strain tensor. The jump due to the transition might therefore vary along the boundaries, even going to zero (phonon softening) at a critical point [72]. These issues can be dealt with by including an anisotropic variant in the model potential which incorporates the complex basis into an effective Hamiltonian between the "point" particles. This jump in the OP at the structural tran-

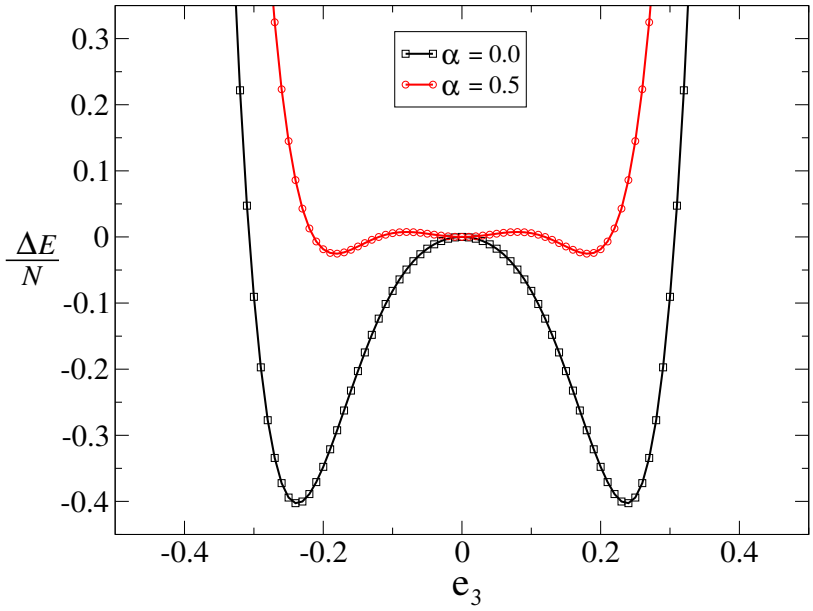

Figure 3.9: Energy difference per particle ($\Delta E/N$) as a function of the shear strain at $\rho = 1.1, v_3 = 0.5$ for $\alpha = 0$ and 0.5. As α increases from its zero to non-zero value, the jump in the order parameter reduces from ± 0.24 to ± 0.18.

sition can be made arbitrarily small by taking $\alpha > 0$. The jump in e_3 reduces from ± 0.24 to ± 0.18 when $\alpha = 0 \rightarrow 0.5$ (fig. 3.9). Our qualitative results are exactly the same, as long as $\Delta e_3 > 0$ at the transition.

3.3.3 $T = 0$ phase diagram in $v_3 - \alpha$ plane

The $T = 0$ phase diagram (fig. 3.10) is computed by starting with an initial square lattice and then deforming it using eqns. 3.8 and 3.2. Considering various values of α, we evaluate the value of v_3 at which the transtion takes place. As discussed earlier, Δe_3 reduces as α

increases weakening the first order transtion. It ultimately vanishes at $\alpha = 1.511, v_3 = 0$ where we get a continuous structural transition. Thus we denote $\alpha = 1.511, v_3 = 0$ and $T = 0$ as the tricritical point α_c.

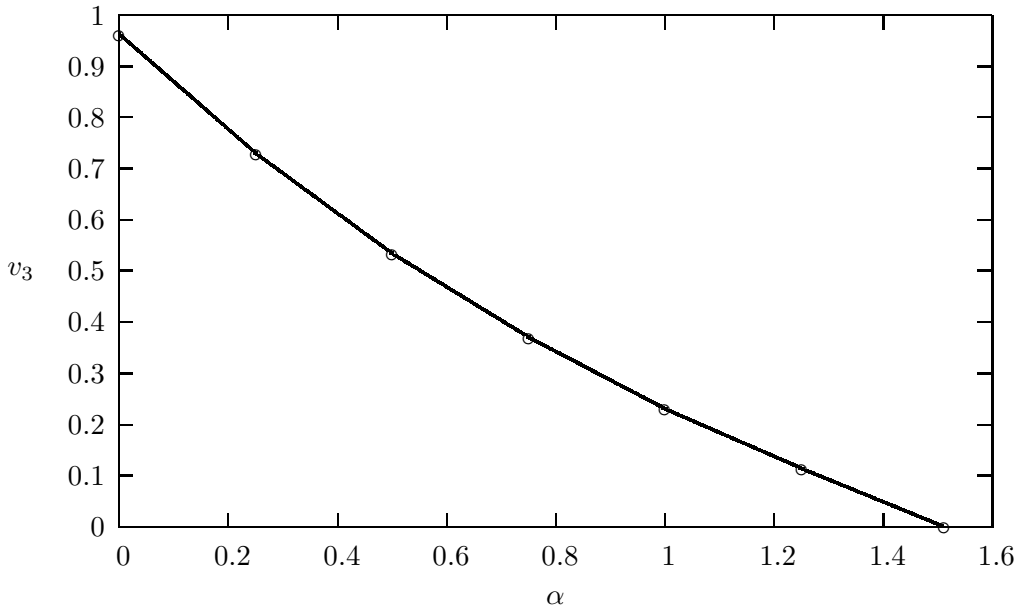

Figure 3.10: The zero temperature phase diagram in the $v_3 - \alpha$ plane at $\rho = 1.1$. The point $v_3 = 0, \alpha = 1.511$ is the tricritical point where the jump in the order parameter vanishes at $T = 0$.

3.4 Structural transitions : stability and normal mode analysis

Normal mode analysis at $T = 0$ temperature are performed on a perfect square and triangular lattice. The normal mode calculations obtains the dispersion curves *i.e.* the variation between ω vs. k_a as one travels along the high symmetry points and directions on the first Brillouin zone in the reciprocal vector space. The anisotropy parameter α in the two body potential V_2 controls the nature of the transition as it varies from zero to higher positive values.

As the particles in our system interact via an effective pair potential, we proceed by first

calculating the force constant or the Hessian matrix defined as,

$$K_{ij}^{pq} = \frac{\partial^2 V}{\partial \mathbf{r}_{ip} \partial \mathbf{r}_{jq}} \tag{3.18}$$

In our case, the potential consists of both two-body and a three-body intercation terms. Note that the triplet terms have been written in Appendix A of chapter 2 as summations over pair terms. Hence, eqn. 3.18 requires the evaluation of derivatives of the interatomic potential. Here (p,q) runs for both the (x,y) cartesian components giving the four terms of the Hessian. i, j represent the particle indices. Once K_{ij}^{pq} is obtained, we determine the dynamical matrix as a function of the wave vector k_a from the relation,

$$D_{pq}(k_a) = -2 \sum_{j \neq 0} K_{ij}^{pq} \sin^2 \frac{\vec{k_a}.\vec{\mathbf{r}_j}}{2} \tag{3.19}$$

To get the dispersion curves we need to solve the eigen value equation,

$$[D_{ij}^{pq}(k_a) - m\omega^2 \mathbf{I}]\mathbf{u}(k_a) = 0 \tag{3.20}$$

by substituting the two dimensional dynamical matrix. The plot of the eigen values of ω as a function k_a gives the final spectrum of vibrational frequencies for the solid.
If we start with an initial perfect square lattice at $v_3 = 0$ and decrease alpha, we get the dispersion curves as shown in fig. 3.11. In fig. 3.11(d) a square lattice is shown with the inner shaded region being the Brillouin zone for the square lattice in the reciprocal vector space. The high symmetry points are again represented by Γ, M and X traversed as $\Gamma \rightarrow$ M $\rightarrow$ X $\rightarrow \Gamma$. When $\alpha = 2$, the non-zero ω values imply a stable square lattice. On the other hand, at $\alpha = 1.511$, we find that at M, the curve shows a minimum nearing $\omega = 0$. Also the value of the curve in the X $\rightarrow \Gamma$ region decreases. This is due to the fact that the square lattice at this point becomes unstable and transition from the square to a rhombic lattice takes place. Finally with $\alpha = 0$, there is a discontinuity at M and the curve in the X $\rightarrow \Gamma$ region vanishes completely with another discontinuity at X. Thus there is a continuous transition at the tricritical point, α_c where $v_3 = 0, \alpha = 1.511$ and $T = 0$.

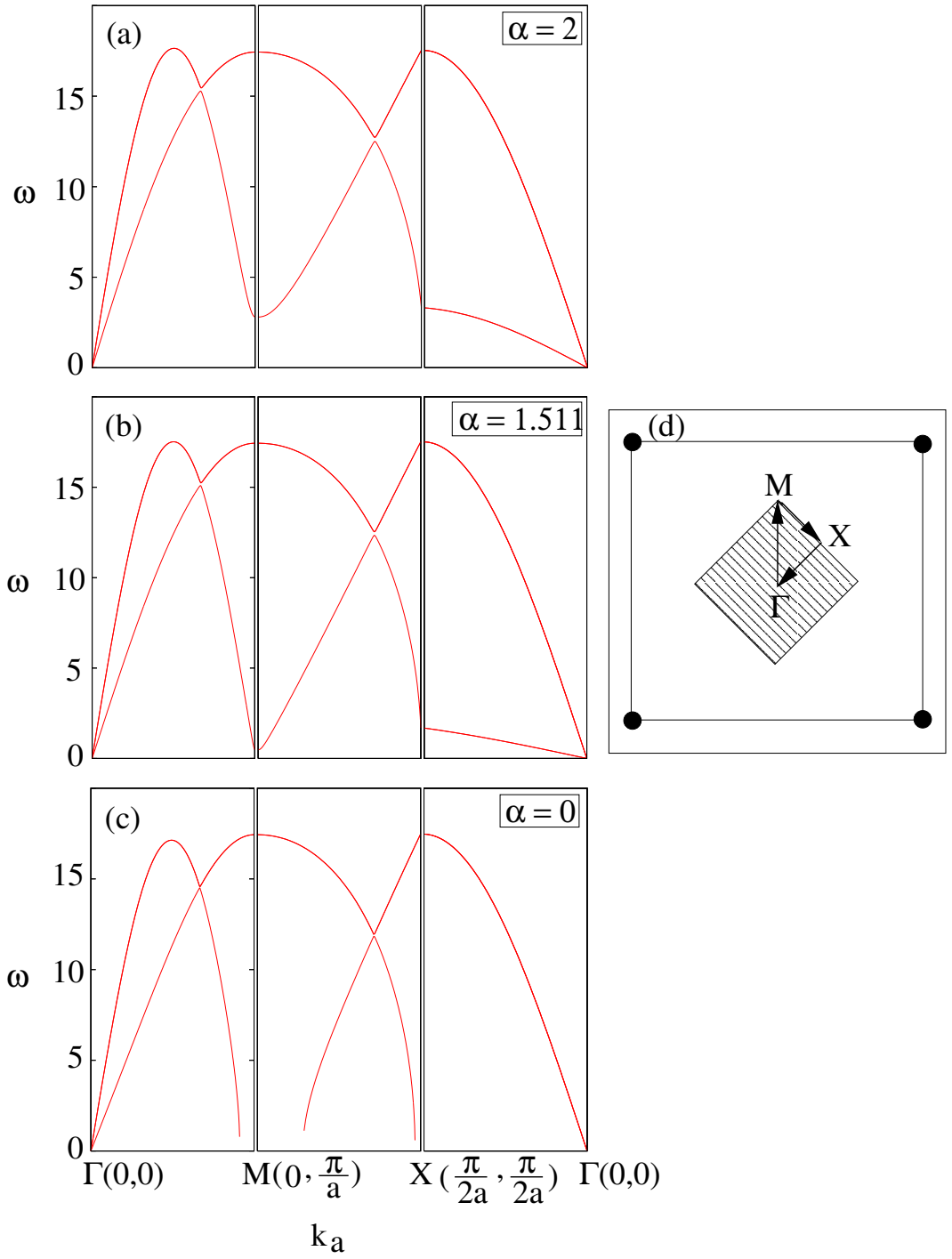

Figure 3.11: Dispersion curves [ω (frequency) vs. k_a (wave vector)] obtained for an initial square lattice with (a) $\alpha = 2$, (b) $\alpha = 1.511$ and (c) $\alpha = 0$. The potential parameters are: $v_3 = 0, \rho = 1.1, T = 0$. The curves show that the square lattice is stable for $\alpha > 1.511$ and there is a structural transition from the square to rhombic lattice at $\alpha = 1.511$. Below this value it is highly unstable. The coordinates of the respective high symmetry points are given in brackets beside each point. (b) The square lattice with the first Brillouin zone is represented by the shaded region. Γ, M, X are the high symmetry points and arrows show the direction in which the points are traversed during the calculations shown in (a).

Fig. 3.12 (a) shows the dispersion curves for the perfect triangular lattice at $\alpha = 0, v_3 = 0$ with $\rho = 1.1$, where it is the thermodynamically stable structure. Γ, M and X are the symmetry points on the first Brillouin zone. Our calculations for ω vs. k_a are done as we move along the direction $\Gamma \rightarrow \mathrm{M} \rightarrow \mathrm{X} \rightarrow \Gamma$ as shown in fig. 3.12 (b).

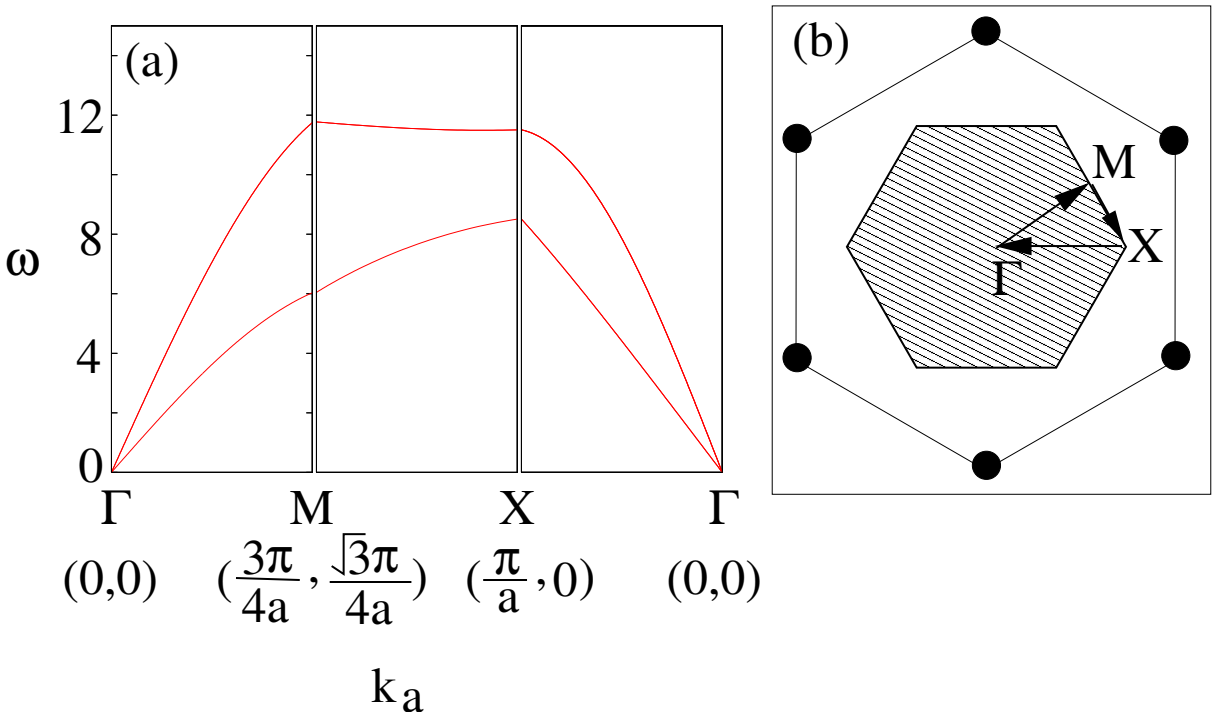

Figure 3.12: (a) Dispersion curves [ω (frequency) vs. k_a (wave vector)] for the uniform triangular lattice with the following potential parameters: $v_3 = 0, \alpha = 0, \rho = 1.1, T = 0$. The curves show that the triangular lattice is stable for the above set of parameters. The coordinates of the respective high symmetry points are given in brackets below each point. (b) The triangular lattice with the first Brillouin zone is represented by the shaded region. Γ, M, X are the special points and arrows show the direction in which the points are traversed for the calculations shown in (a).

3.5 Landau theory for the square to rhombus and triangle to square transitions

The square to rhombus structural transition represented by the $p4mm \rightarrow p2$ group transformation is controlled by a single order parameter strain e_3. The transformation can be

described by the Landau Φ^6 theory. The free energy density function f_1 for the transition can thus be written as,

$$f_1 = A_1 {e_3}^2 - B_1 {e_3}^4 + C_1 {e_3}^6 \tag{3.21}$$

A detailed discussion of the continuum Landau theory with the inclusion of the density fluctuations is given in [33]. On tuning the parameter A_1, there is a first order square to rhombus transition.

Next we talk about the triangle to square phase transition. This is a transition between the space groups $p6 \rightarrow p4mm$. The transition is controlled by two order parameters, the deviatoric strain e'_2 and the shear strain e'_3. Considering these homogenous strains of the lattice, the free energy density function f_2 is written as a polynomial in terms of e'_2 and e'_3 as follows,

$$f_2 = A_2(e'^2_2 + e'^2_3) + B_2 e'_2(e'^2_2 - 3e'^2_3) + C_2(e'^2_2 + e'^2_3)^2 \tag{3.22}$$

The presence of the third order term implies the first order transition. The coefficients A_2, B_2, C_2 are to be determined from the minima criterion. To evaluate A_2, B_2, C_2 we consider a triangular lattice at $\rho = 1.05$ and lattice parameter $a = 1.0486$. Assuming $e'_1 = 0$ and applying the conditions for the equality of lenghts of the sides and diagonals on a rhombic lattice, we obtain the following values of e'_2 and e'_3 from the three matrices M_1, M_2 and M_3 given in eqns. 3.13, 3.14 and 3.15 respectively ;

$$\begin{aligned} \text{For} \quad \theta = 0^\circ, e'_2 = 0.267, e'_3 = 0.232 \\ e'_2 = 3.732, e'_3 = 3.232 \end{aligned} \tag{3.23}$$

$$\begin{aligned} \text{For} \quad \theta = 120^\circ, e'_2 = -7.464, e'_3 = 0 \\ e'_2 = -0.5358, e'_3 = 0 \end{aligned} \tag{3.24}$$

$$\begin{aligned} \text{For} \quad \theta = 240^\circ, e'_2 = 0.267, e'_3 = -0.232 \\ e'_2 = 3.732, e'_3 = -3.232 \end{aligned} \tag{3.25}$$

These values of e'_2 & e'_3 correspond to the three degenerate minimas of the free energy density. The values A_2, B_2 and C_2 are obtained by finding the minima of the free energy function f_2 and equating the same to the values of e'_2 & e'_3 in eqns. 3.23, 3.24 and 3.25.

Now in case of a two variable function, the minimum is determined by the following method. For a function say f(x,y), the critical points are solutions of the equations $f_x(x,y) = 0$ & $f_y(x,y) = 0$ which are solved simultaneously. The second derivative test is, $D_e(x_c, y_c) = f_{xx}(x_c, y_c) f_{yy}(x_c, y_c) - [f_{xy}(x_c, y_c)]^2$ where if

i) $D_e > 0$ & $f_{xx}(x_c, y_c) < 0$, $f(x,y)$ has a relative maximum at (x_c, y_c);

ii) $D_e > 0$ & $f_{xx}(x_c, y_c) > 0$, $f(x,y)$ has a relative minimum at (x_c, y_c) ;

iii) $D_e < 0$, $f(x,y)$ has a saddle point at (x_c, y_c) ;

iv) $D_e = 0$, the second derivative is inconclusive.

Therefore the two equations to be solved simultaneously are,

$$\begin{aligned} 2A_2 e_2' + 3B_2 e_2'^2 - 3B_2 e_3'^2 + 4C_2 e_2' (e_2'^2 + e_3'^2) = 0 \\ 2A_2 e_3' - 6B_2 e_2' e_3' + 4C_2 e_3' (e_2'^2 + e_3'^2) = 0 \end{aligned} \tag{3.26}$$

We give the solutions of eqn. 3.26 in Apendix B at the end of this chapter. Thus we get seven pairs of roots among which four pairs correspond to minimas and the remaining three correspond to the saddle points. Scaling one of the coefficients to 1, we assume $B_2 = 1$. Equating the roots in eqns. 3.28 and 3.29 to -7.464 and -0.5358 of eqn. 3.24 we obtain $A_2 = 0.749871$ and $C_2 = 0.093752$. Putting the values of A_2, B_2 and C_2 in the expressions for the roots we get the values of e_2' and e_3' for the Landau theory as follows :

(i) $e_2' = 0, e_3' = 0$

(ii) $e_2' = -7.464, e_3' = 0$

(iii) $e_2' = -0.5358, e_3' = 0$

(iv) $e_2' = 0.267, e_3' = -0.469$

(v) $e_2' = 0.267, e_3' = 0.469$

(vi) $e_2' = 3.732, e_3' = -6.464$

(vii) $e_2' = 3.732, e_3' = 6.464$

Calculation of D_e and f_{xx} shows that the pairs $(i), (ii), (vi)$ and (vii) represent the minimas while $(iii), (iv)$ and (v) correspond to the saddle points (fig. 3.13 (a)). This is further seen in fig. 3.13 (b) where we plot f_2 as a function of e_2' and e_3' by incorporating the values of A_2, B_2 and C_2 along with the various pairs of roots. Fig. 3.13 shows one triangle minima at zero and three degenerate square minimas. Thus we obtain the required result from the Landau theory for the triangle to square transformation.

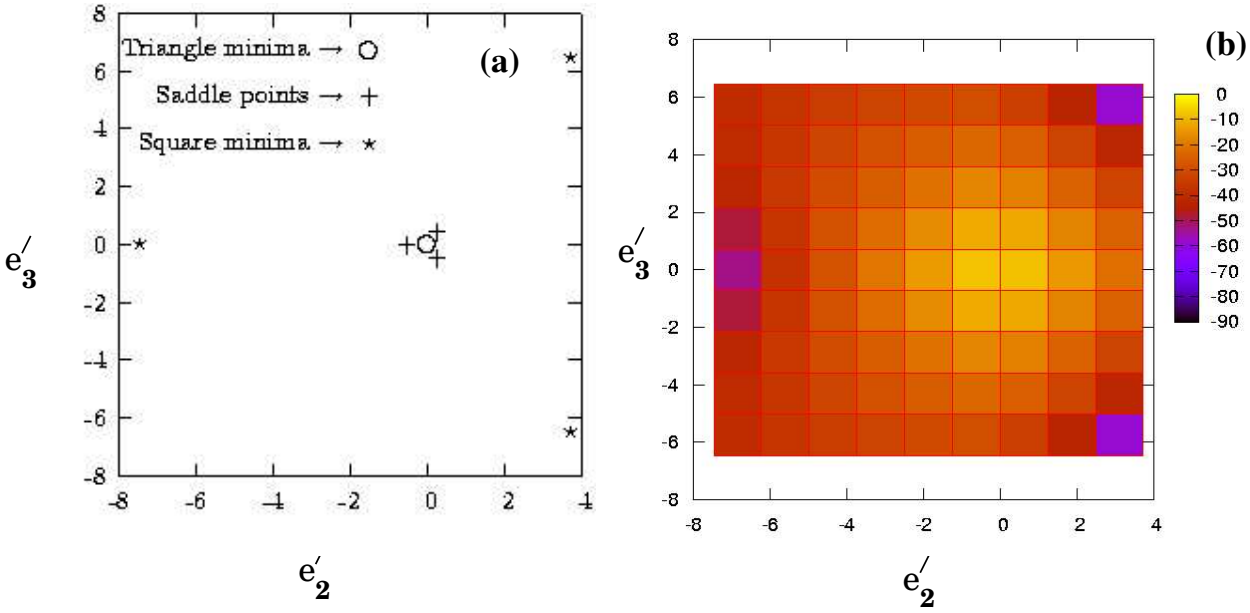

Figure 3.13: (a) Figure shows the different pairs of roots obtained for the triangle to square transformation with the nature of the roots denoted in the figure.(b) Plot for the Landau free energy density f_2 for the triangle to square transition as a functional of e_2' and e_3' for various pair of roots. Here $A_2 = 0.749871$, $B_2 = 1$ and $C_2 = 0.093752$.

3.6 Appendix B

The solution for eqn. 3.26 gives the following pairs of roots.

$$i)\ \ e_2' = 0, e_3' = 0 \tag{3.27}$$

$$ii)\ \ e_2' = \frac{-3B_2 - \sqrt{9B_2^2 - 32A_2C_2}}{8C_2}, e_3' = 0 \tag{3.28}$$

$$iii)\ \ e_2' = \frac{-3B_2 + \sqrt{9B_2^2 - 32A_2C_2}}{8C_2}, e_3' = 0 \tag{3.29}$$

$$iv)\ \ e_2' = \frac{3B_2 - \sqrt{9B_2^2 - 32A_2C_2}}{16C_2},$$

$$e_3' = -\frac{[(-3A_2/4) + (27B_2^2/64C_2) - (9B_2\sqrt{9B_2^2 - 32A_2C_2}/64C_2)]^{1/2}}{\sqrt{2C_2}} \tag{3.30}$$

$$v)\ \ e_2' = \frac{3B_2 - \sqrt{9B_2^2 - 32A_2C_2}}{16C_2},$$

$$e_3' = \frac{[(-3A_2/4) + (27B_2^2/64C_2) - (9B_2\sqrt{9B_2^2 - 32A_2C_2}/64C_2)]^{1/2}}{\sqrt{2C_2}} \tag{3.31}$$

$$vi)\ \ e_2' = \frac{3B_2 + \sqrt{9B_2^2 - 32A_2C_2}}{16C_2},$$

$$e_3' = -\frac{[(-3A_2/4) + (27B_2^2/64C_2) + (9B_2\sqrt{9B_2^2 - 32A_2C_2}/64C_2)]^{1/2}}{\sqrt{2C_2}} \tag{3.32}$$

$$vii)\ \ e_2' = \frac{3B_2 + \sqrt{9B_2^2 - 32A_2C_2}}{16C_2},$$

$$e_3' = \frac{[(-3A_2/4) + (27B_2^2/64C_2) + (9B_2\sqrt{9B_2^2 - 32A_2C_2}/64C_2)]^{1/2}}{\sqrt{2C_2}} \tag{3.33}$$

To find the values of A_2, B_2 and C_2 we equate these expressions for the roots to the values obtained from the microscopic theory in eqns. 3.23, 3.24, 3.25.

Chapter 4

Phase diagram

4.1 Introduction

In the last chapter we have dealt with the zero temperature ($T = 0$) properties of the two dimensional (2D) model solid introduced in chapter 2. We observed that the nature of the transitions can be classified as either first order or continuous depending on the values of the parameters of the model. Here we proceed a step further by performing finite temperature ($T \neq 0$) calculations to obtain the three dimensional phase diagram in the parameter space of α, v_3 and T. The complete phase diagram involves, as in the $T = 0$ case, both first order and continuous structural transitions. Using Monte Carlo simulations, free energies of the square and rhombic lattices are calculated which ultimately leads to the evaluation of the phase boundaries in the $v_3 - T$ plane for various α. To evaluate the first order lines in the $v_3 - T$ planes, we take help of an efficient method described by J. R. Morris and K. M. Ho [73]. If the anisotropy parameter $\alpha \neq 0$, this method becomes difficult to use and we evaluate the free energies and hence the phase boundaries using thermodynamic integration technique using the Einstein crystal as reference [63]. The $\alpha - v_3$ plane shows a first order line which terminates at what appears to be a tricritical point α_c at $\alpha = 1.511, v_3 = T = 0$. In the following part, we describe the continuous structural transition in the $\alpha - T$ plane . It shows typical strain texturing similar to those observed in tweeds [74, 75, 76]. At higher temperatures, the system melts into a liquid.

4.2 Methods for free energy calculations

To evaluate the complete phase diagram in the $\alpha - v_3 - T$ plane, knowledge of the relevant free energies of the parent square and product rhombic phases are required. Here we describe the two methods used by us to get the free energies of the perfect square and triangular lattices. While the first one is applicable in case of isotropic potential, the later is used for the potential with $\alpha \neq 0$.

4.2.1 The method of Morris & Ho

J. R. Morris and K. M. Ho [73] have presented a simple method for the calculation of the free energy for solids from a single simulation. Typical methods like thermodynamic integration technique employs a series of simulations to calculate the free energy, F of the solid. It transforms the solid reversibly into an Einstein crystal or other harmonic solid whose free energy, F_0 is known exactly [63]. If there is a reference potential V_0 with known F_0, the free enegy F at a different potential V may be calculated by using the equation,

$$F - F_0 = \int_0^1 \langle V - V_0 \rangle_\lambda d\lambda \tag{4.1}$$

This approach assumes that there are no irreversible processes occurring as the system is perturbed through the path from $\lambda = 0$ to $\lambda = 1$. Multiple simulations with various values of λ are necessary to evaluate the above integral. By employing the method of J. R. Morris and K. M. Ho, the free energies for perfect solids are found from a single simulation for different values of v_3 and T. The method works as follows.

Consider a particle in a one dimensional confining potential V with the partition function $Z = \frac{1}{\lambda_d} \int \exp[-\beta V]\, dx = \exp[-\beta F]$. The thermal de Broglie wavelength, $\lambda_d = h/(2\pi m T)^{1/2}$. From Gibbs-Bogoliubov inequality [77] we get,

$$F \leq F_0 + \langle V - V_0 \rangle_0 \tag{4.2}$$

The average in the above equation is with respect to a trial potential with known free energy F_0. If the roles of the trial and actual potential are reversed, then averaging with respect to V gives,

$$F_0 \leq F + \langle V_0 - V \rangle \tag{4.3}$$

and the corresponding entropy for $S \leq S_0$ is given as

$$S \equiv -\beta[F - \langle V \rangle - \langle E_k \rangle] \tag{4.4}$$

where $\langle E_k \rangle = T/2$ is the average kinetic energy. If we assume a harmonic trial potential with $V_0(x) = \frac{1}{2}m\omega^2 x^2$, then the trial entropy is,

$$S_0 = \frac{1}{2} + \frac{1}{2}\ln\left(\frac{2\pi T}{m\omega^2\lambda_d^2}\right) + \frac{m\omega^2\langle x^2\rangle}{2T} \tag{4.5}$$

which when minimized with respect to ω gives $\omega^2 = T/m\langle x^2\rangle$. Generalising this result to our 2D solid consisting of N particles the correlation matrix is defined as,

$$C = \begin{pmatrix} C_{11} & C_{12} & - & - & - & C_{1N} \\ C_{21} & C_{22} & - & - & - & C_{2N} \\ - & - & - & - & - & - \\ C_{N1} & - & - & - & - & C_{NN} \end{pmatrix} \tag{4.6}$$

with,

$$C_{ij} = \begin{pmatrix} \langle x_i x_j\rangle - \langle x_i\rangle\langle x_j\rangle & \langle x_i y_j\rangle - \langle x_i\rangle\langle y_j\rangle \\ \langle y_i x_j\rangle - \langle y_i\rangle\langle x_j\rangle & \langle y_i y_j\rangle - \langle y_i\rangle\langle y_j\rangle \end{pmatrix} \tag{4.7}$$

where i, j refer to a pair of particles. The C matrix is symmetric and real and it is diagonalized to get a set of decoupled modes for the system. The product of the eigen values is the determinant of the correlation matrix. Therefore S_0 becomes,

$$S_0 = \frac{N}{2}\ln(\frac{2\pi}{\lambda_d{}^2}) + \frac{1}{2}\ln(\det C) + N \tag{4.8}$$

Now using the expression for V_0 & S_0 in the Bogoliubov inequality, we get the expression for F as,

$$F \geq \langle V \rangle - \frac{NT}{2} - \frac{T}{2}\ln[\left(\frac{2\pi}{\lambda_d{}^2}\right)^N \det C] \tag{4.9}$$

At any given temperature T, the instantaneous correlation matrix can be determined from the simulation. The bound is determined by the accuracy of the equilibrium correlation function. Hence in the Monte Carlo simulations, the determinant of the correlation matrix is averaged over the ensemble of configurations pertaining to a particular crystal structure at equilibrium. We use the above procedure to evaluate the free energies of the square and the rhombic phases separately. It is essential that throughout this calculation, the eigen values of C remain positive definite. This implies that the cyrstal lattice in question is at least locally stable.

4.2.2 Thermodynamic integration method

In case of the anisotropic potential, we use the usual thermodynamic integration scheme to obtain the free energy. This is necessary because at finite temperatures, for non-zero values of α, ($\alpha \neq 0$), the quasiharmonic assumption becomes intenable rendering the correlation matrix method impractical. This difficulty is overcome by tethering the crystal to a set of ideal lattice positions with the help of harmonic springs. The reference ideal solid is the Einstein crystal which consists of a set of noninteracting particles. During the thermodynamic integration process, we "switch on" the spring constant κ and simultaneously "swithch off" the intermolecular interactions. Thus we consider the potential,

$$\tilde{V}(\mathbf{r}_{ij}) = V(\mathbf{r}_{ij})_0 + (1-\kappa)[V(\mathbf{r}_{ij}) - V(\mathbf{r}_{ij})_0] + \kappa \sum_{i=1}^{N} \gamma \{\mathbf{r}_{ij} - (\mathbf{r}_{ij})_0\}^2 \tag{4.10}$$

where $(\mathbf{r}_{ij})_0$ represent the position vectors of the initial square lattice, κ is the switching parameter such that for $\kappa = 0$ the original interactions are recovered and for $\kappa = 1$, the intramolecular interactions are completely switched off and the system behaves like an ideal noninteracting Einstein crystal. The parameter γ is determined from the fact that the interactions in the pure Einstein crystal differs as little as possible from the original system under consideration. This suggests that the mean-squared displacements for $\kappa = 1$ and $\kappa = 0$ should be equal.

$$\langle \sum_{i=1}^{N} \{\mathbf{r}_{ij} - (\mathbf{r}_{ij})_0\}^2 \rangle_{\kappa=0} = \langle \sum_{i=1}^{N} \{\mathbf{r}_{ij} - (\mathbf{r}_{ij})_0\}^2 \rangle_{\kappa=1} \tag{4.11}$$

For the noninteracting Einstein crystal, the mean-squared displacement is given by $\langle \mathbf{r}_{ij}^2 \rangle_\kappa = \mathcal{D}/2\beta\kappa$ where $\mathcal{D}$ refers to the dimension of the system. Therefore,

$$\frac{1}{\gamma} = \frac{2\beta}{\mathcal{D}N} \langle \sum_{i=1}^{N} \{\mathbf{r}_{ij} - (\mathbf{r}_{ij})_0\}^2 \rangle_{\kappa=0}$$

$$\text{for } \mathcal{D} = 2, \quad \gamma = \frac{N}{\beta \langle \sum_{i=1}^{N} \{\mathbf{r}_{ij} - (\mathbf{r}_{ij})_0\}^2 \rangle_{\kappa=0}} \tag{4.12}$$

The free energy for several κ values are obtained by performing simulations with the potential form $\tilde{V}(\mathbf{r}_{ij})$ with proper γ values for $\alpha = 1$. The stiffness of these springs is then gradually taken to zero and the free energy for the crystal is obtained by extrapolation for each value of α, v_3 and T.

4.3 Three dimensional phase diagram

The three dimensional phase diagram for our model two dimensional system is obtained in the parameter space comprising of v_3, T and α. It consists of a first order surface starting from the $v_3 - T$ plane which meets the continuous transition line in the $\alpha - T$ plane with a tricritical point at $\alpha = 1.511, v_3 = 0, T = 0$. We describe the phase diagram considering $v_3 - T$ and $\alpha - T$ planes seperately. The $T = 0$ phase diagram in the $v_3 - \alpha$ plane has already been evaluated for our model solid in section 3.3.3.

4.3.1 The $v_3 - T$ plane

To evaluate the phase boundary in the $v_3 - T$ plane, Monte Carlo simulations are done to get the free energy curves for the square and rhombic lattices. To calculate the equlibrium free energy, typical system sizes comprised of $N = 400$ particles which were equilibrated for 25×10^3 timesteps during the Monte Carlo simulation. We have repeated the calculations for a few data points with a larger system. The change in the free energy is small and does not affect the qualitative nature of the results.

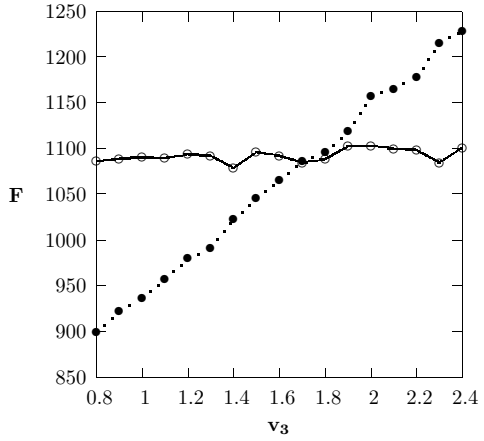

Figure 4.1: Intersection of the free energy curves for the perfect square (open circle) and triangular (filled circle) lattices. The point of transition is at $v_3 = 1.695$ for $\alpha = 0, T = 0.1, \rho = 1.1$. Monte Carlo simulations using the method described by J. R. Morris & K.M. Ho were performed to generate the data. For each value of v_3, the system was equilibrated for 25×10^3 steps and thereafter the correlation matrix was averaged over 18×10^3 configurations.

The intersection of these pure phase free energy curves at a definite value of v_3 correspond to the transition point for each temperature. These transition points when plotted against temperature gives a first order transition line. The plot in fig. 4.1 shows the free energy curves for the isotropic potential intersecting at $v_3 = 1.695$ for $T = 0.1, \rho = 1.1$. The anisotropic potential at finite temperatures also reveals a first order transition line in the $v_3 - T$ plane. For finite values of α, thermodynamic integration is used to get the free energy for the perfect square lattice while for the rhombic lattice both the methods described in the previous section were used to obtain the free energy with values which agreed with each other upto within a percent. Fig. 4.2 shows the intersection of the free energy curves for $\alpha = 1.0$. The curves intersect at $v_3 = 0.44$ for $\alpha = 1.0, T = 0.1, \rho = 1.1$. The first order transition lines thus obtained for both $\alpha = 0$ and $\alpha = 1$ in the $v_3 - T$

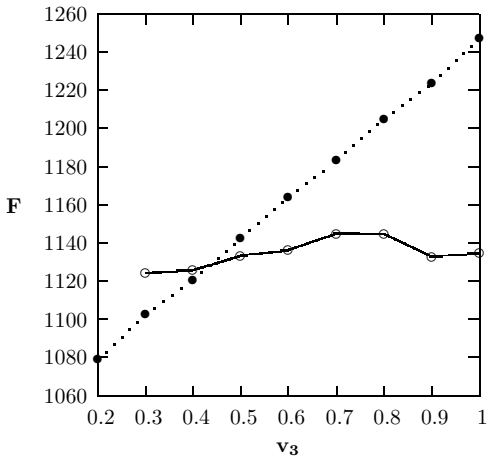

Figure 4.2: Intersection of square (open circle) and rhombic lattices (filled circle) for the anisotropic potential with $\alpha = 1.0$. Transition at $T = 0.1, \rho = 1.1$ takes place at $v_3 = 0.44$. Einstein crystal technique is used to get the free energy of the square while the rhombic free energy is calculated through Monte Carlo simulations using the Morris & Ho method.

plane are shown in fig. 4.3. The square phase is stable for higher values of v_3 while the rhombic phase is stable at lower values of v_3. As the anisotropy α is increased, the transition line shifts to lower values of v_3 stabilizing the square lattice for larger ranges of v_3. Increasing the amount of anisotropy however also weakens the first order transition further and ultimately leads to tricritical fluctuations. Thus for finite temperatures, the

square to rhombic lattice structural transition is first order in nature over a wide range of parameter space. In fig. 4.4 we show results for the transition at two different densities. We find that for higher densities, the transition point shifts to higher values of v_3. The square phase becomes unstable for lower values of v_3 as the density is increased. This is expected since a high density favours the triangular lattice.

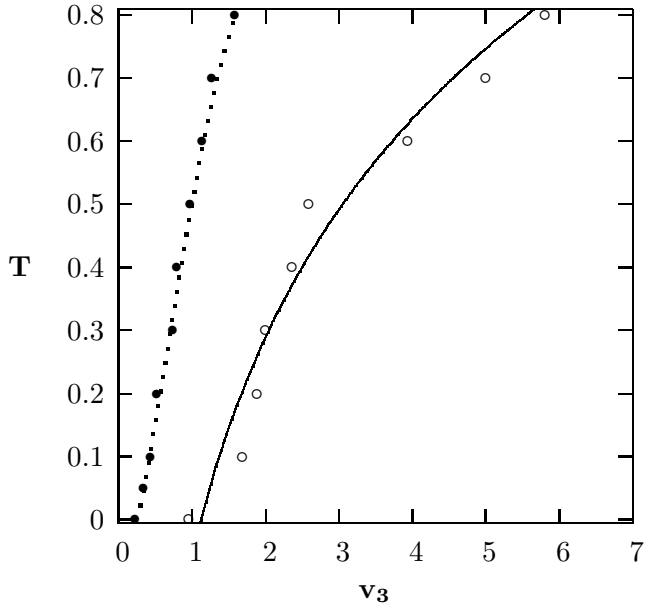

Figure 4.3: Phase diagram in the $v_3 - T$ plane showing first order lines for $\alpha = 0$ (open circle) and $\alpha = 1$ (filled circle). The line of transition shifts to lower values of v_3 for non-zero α stabilizing the untransformed square phase for larger ranges of v_3.The data obtained is for $\rho = 1.1$

4.3.2 The $v_3 - \alpha$ plane

The $T = 0$ phase diagram showing the structural transition in the $v_3 - \alpha$ plane has been discussed in section 3.3.3. At $T = 0$, eqns. 3.8 and 3.2 were considered to get the phase boundary separating the transformed rhombic phase from the untransformed square phase. Fig. 3.10 shows the phase diagram in the $v_3 - \alpha$ plane for $\rho = 1.1$. The transition remains first order at finite values of v_3 with $\alpha = 0$. With the increase in α, the jump in the order parameter decreases ultimately vanishing at $\alpha = \alpha_c = 1.511$. This

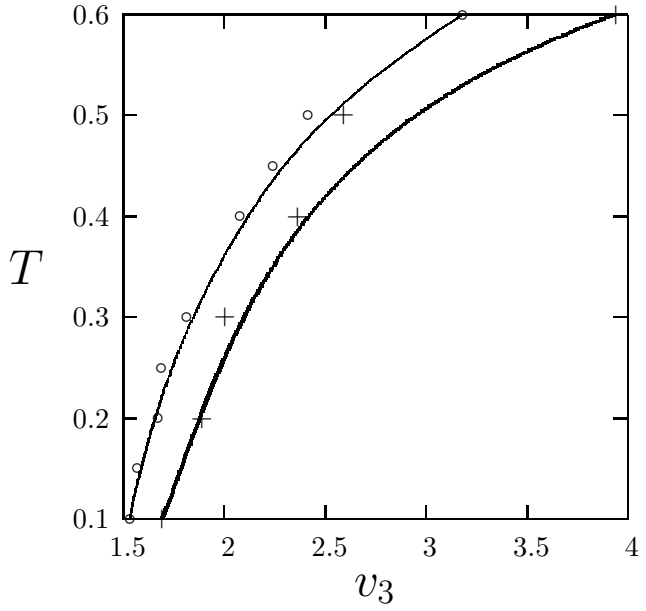

Figure 4.4: Phase diagram in the $v_3 - T$ plane showing first order lines for $\rho = 1.05$ (o) and $\rho = 1.1$ (+) for the isotropic potential. With the increase in density, the line of transition shifts to higher values of v_3 decreasing the region of stability for the square lattice.

also weakens the first order transition and hence at $v_3 = 0$ we get a tricritical point, α_c where the first order surface ends giving way to continuous transitions.

4.3.3 The $\alpha - T$ plane

We have seen that for finite $\alpha > \alpha_c$ and $v_3 = T = 0$, the structural transition becomes continuous in nature. At $T \neq 0$, the nature of the transition is obtained from our results for the specific heat calculations. Monte Carlo simulations give the specific heat C_v as the fluctuations in energy E,

$$C_v/k_B = \frac{\langle E^2 \rangle - (\langle E \rangle)^2}{N {k_B}^2 T^2} \tag{4.13}$$

The jump in the specific heat data confirms the presence of a square to rhombic transition (fig. 4.5). In general it is difficult to establish the order of the transition from a plot of the specific heat alone. A detailed finite size scaling analysis needs to be undertaken in order to establish the nature of the transition and the universality class. Since the transition

may be described within a spin-1 Ising theory, we however expect the divergence in C_v to be logarithmic in two dimensions [64].

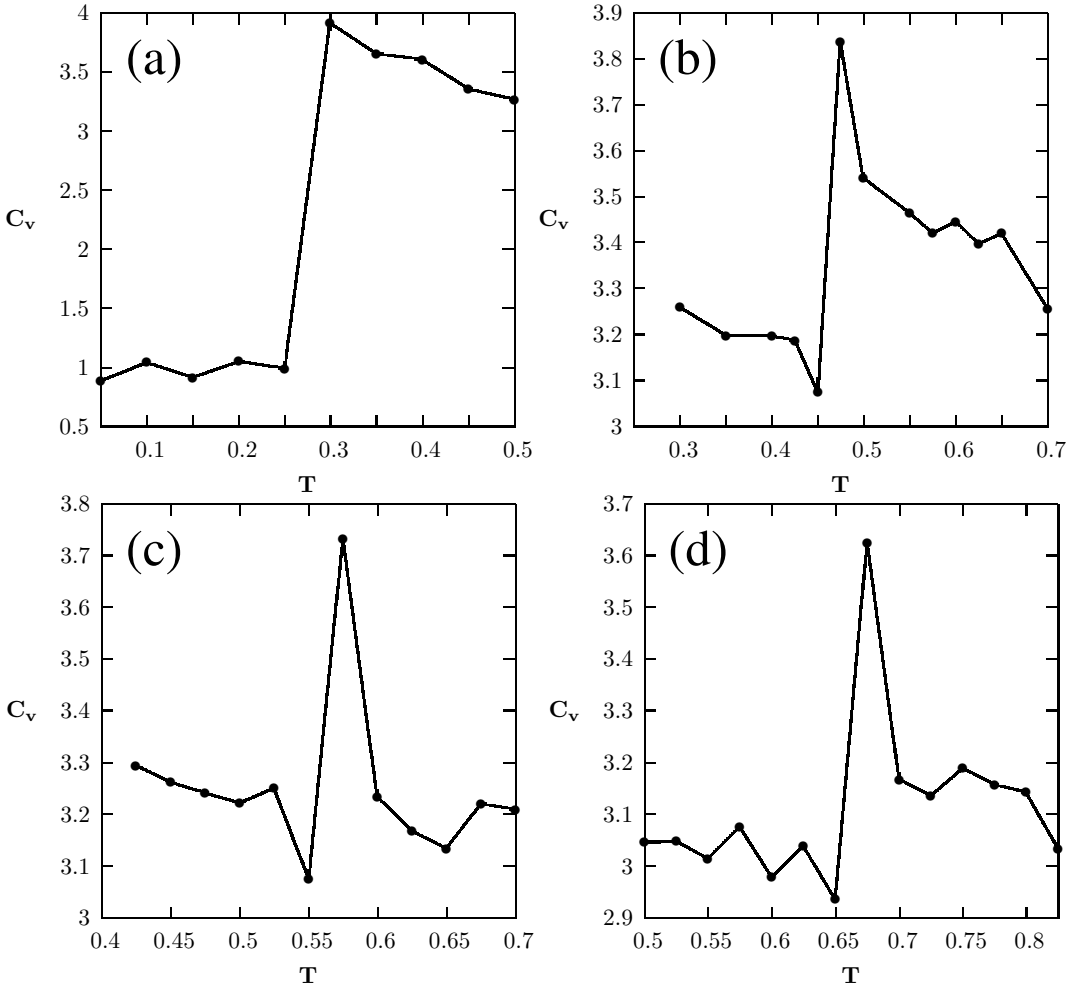

Figure 4.5: Figure shows the plot of specific heat with temperature at $v_3 = 0$ for (a)$\alpha = 1.7$, (b)$\alpha = 2.0$, (c)$\alpha = 2.25$ and (d)$\alpha = 2.5$. The jump in C_v proves the continuous nature of the transition in the $\alpha - T$ plane.

An examination of the snapshots of the system near the transition confirms that the transition is continuous. We show in fig. 4.6 a plot of the local shear strain e_3 - the order parameter for the square to rhombic transition. To obtain this plot, the system was first equilibrated at $\alpha = 1.75$ and $T = 0.1$. After equilibration, the system was quenched to $T = 0.75$ at the same value of α. Molecular dynamics simulation snapshots at different time steps are shown in figure 4.6. We characterize the resulting structures by calculating

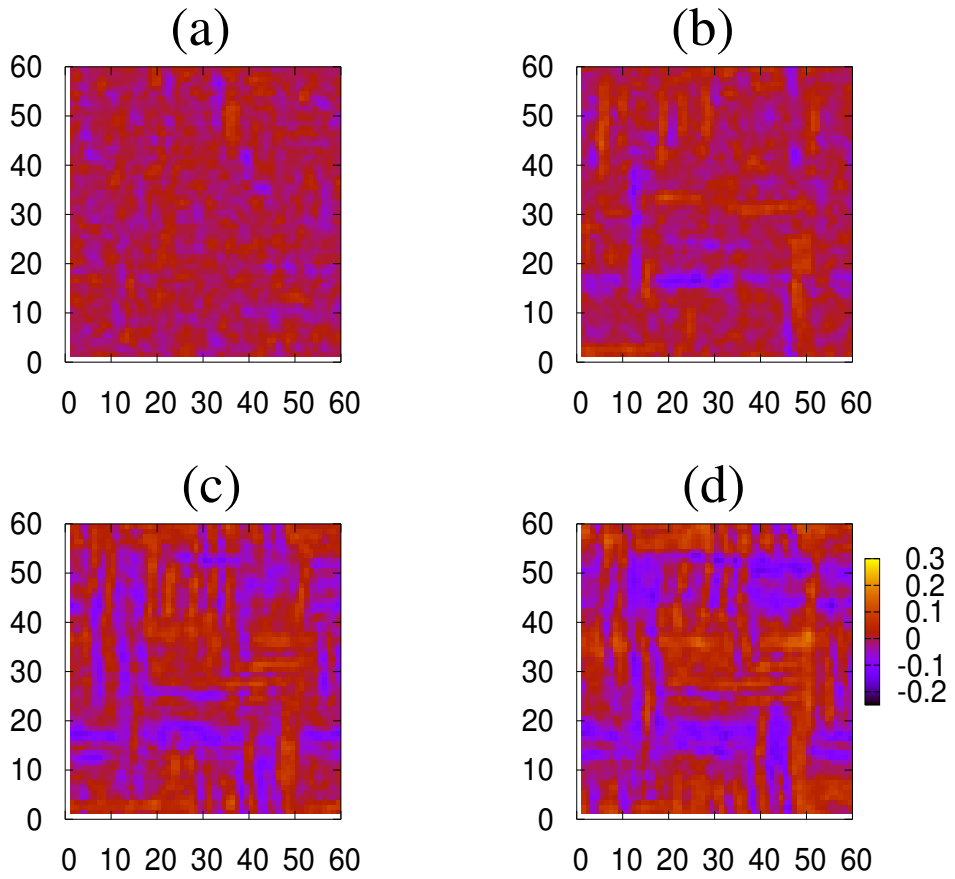

Figure 4.6: Configuration pictures obtained for quenches in temperature from $T = 0.1$ to $T = 0.75$ for $\alpha = 1.75$ with $v_3 = 0$ at (a) 2×10^3 MD-steps, (b) 8×10^3 MD-steps, (c) 13×10^3 MD-steps and (d) 15×10^3 MD-steps. The characterization in the pictures are done by calculating the shear strain e_3 for the lattice.

the local shear strain e_3 using the method discussed in section 5.3.2 of chapter 5. The reference state for the calculation was taken to be the undistorted square lattice. The typical strain textures shows a strong resemblance to spinodal structures in elastically coupled Ising-like systems [78]. It is known that long ranged forces arising from elastic interactions strongly influence the domain growth behaviour of these systems reducing the Lifshitz-Slyozov exponent away from its typical value = 1/3. However, our present data does not allow us to draw quantitative conclusions about domain growth behaviour in this model. Performing extensive computations to study such domain growth behaviour in this regime remains as one of our goals to be accomplished in future.

The phase diagram with the critical line in the $\alpha - T$ plane is shown in fig. 4.7 (a). As the temperature is increased the stability of the square phase shifts to higher values of α.

Lastly, we mention that for higher temperatures, the system melts into a liquid. At

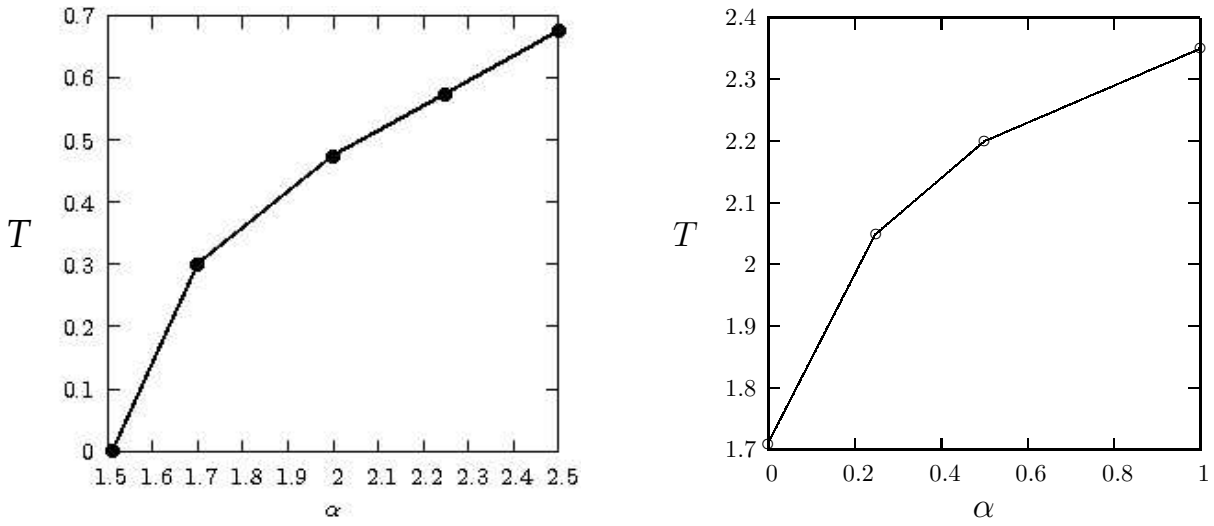

Figure 4.7: (a) Phase diagram in the $\alpha - T$ plane showing the continuous transition line starting at α_c. Here $v_3 = 0$. (b) Figure shows the melting transition line in the $\alpha - T$ plane. As α increases, the melting temperature goes to higher values. The data is obtained from the nature of the radial distribution function $g(r)$. The data in both the figures is for a system of density $\rho = 1.1$.

$\alpha = v_3 = 0$ and $\rho = 1.1$, the melting transition is given by the formula [79],

$$\rho_s \beta_s^{2/n} = \rho \beta^{2/n} \tag{4.14}$$

Here n represents the power of the interaction which is (1/12) in case of $v_3 = 0$. With $\rho_s = 1.006$ and $T_s = 1$, the melting temperature $T_m = 1.709$ in our units. For finite values of α we get the melting line as shown in fig. 4.7 (b). The nature of the melting transition line is obtained from the radial distribution function $g(r)$ (Fig. 4.8). It is seen that for finite values of α, T_m increases while it is only weakly dependent on v_3.

Connecting the three planes we get the full three dimensional phase diagram in the

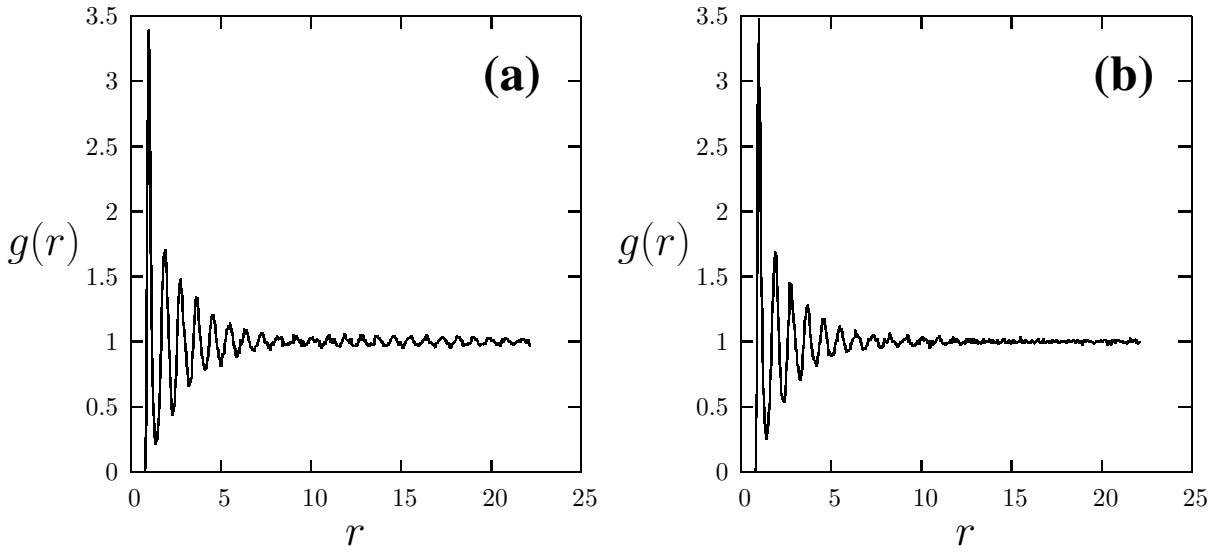

Figure 4.8: Figure shows the plots for the $g(r)$ at (a) $T = 2.0$ and (b) $T = 2.2$ for $\alpha = 0.5$ at $v_3 = 0$ and $\rho = 1.1$. The nature of the radial distribution function clearly shows that the system melts at $T = 2.2$ for $\alpha = 0.5$.

$\alpha - v_3 - T$ planes (Fig.4.9) for the square to rhombic structural phase transition in our two dimensional model system. The stage is now set to proceed with our aim to study the different evolving microstructures obtained at different regions of the phase space.
In the next chapter we illustrate the richness of this model solid by carrying on dynamical experiments *viz.* quenching from the square into the rhombic phase using various protocols. The resulting snapshots at various times show a rich variety of microstructures, each evolving with its distinct coarse-grained dynamics. In the rest of the thesis, we shall study, in detail, these dynamical processes of nucleation and growth which lead to the variety of microstructures.

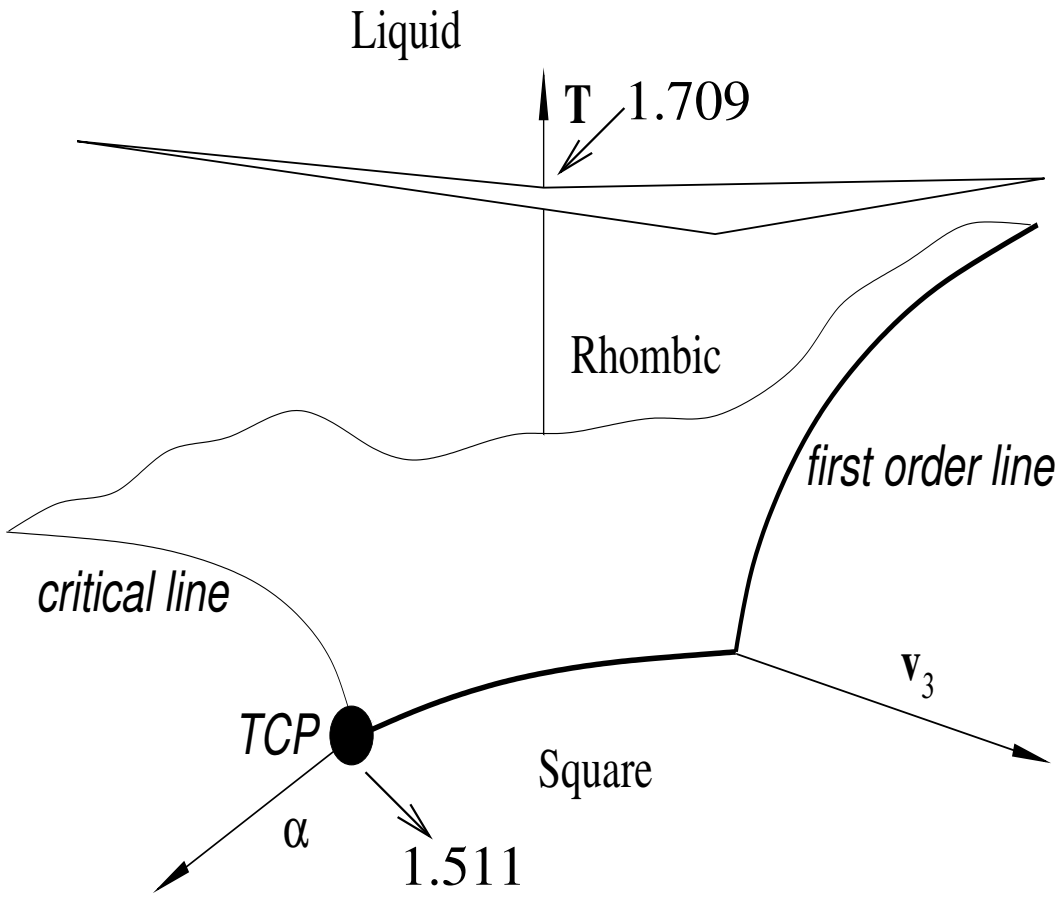

Figure 4.9: The phase diagram of the model system in the space of α, v_3 and T. The funnel shaped first order surface is bounded by first order boundaries (bold lines) and a critical line (thin line) which terminates at a tricritical point $\alpha_c = 1.511$ (black dot). The phase within the funnel is rhombic which continuously transforms to a triangular phase for $\alpha = 0$. The phase outside the funnel has square symmetry. For large temperatures the solid melts via a first order transformation to a liquid.

Chapter 5

Characteristics of microstructure selection from molecular dynamics simulations

5.1 Introduction

In the last chapter we have obtained the three dimensional dynamical phase diagram for our model solid in the $\alpha - v_3 - T$ plane. We have shown that the solid exists either as a square or a rhombic crystal separated by a first order surface which ends at a critical line and a tricritical point. In this chapter we begin our study of microstructure selection by performing several quenching schedules using the dynamical phase diagram. These quenches are done from the square into the rhombic region. By changing v_3 or α at constant temperature in the $v_3 - T$ plane we get an atlas of microstructures or snapshots of particles during the formation of the product phase. The related particle snapshots obtained by performing molecular dynamics simulations show interesting microstructures for various values of the temperatures. The product phase inside the parent crystal experiences varying dynamical constraints which determines the mode of nucleation and its subsequent growth. Hence microstructure selection is a dynamic process leading to various product phases with different distinct physical features. These microstructures are reproducible and show that at high temperatures the triangular solid forms within isotropic patches with a high degree of local disorder while at low temperatures anisotropic but structurally ordered nuclei are produced. These two limits are not mutually exclusive. Indeed, at intermediate temperatures, the resulting microstructures can be quite complex often containing a mixture of the two extreme situations at different temporal and spatial locations, a feature observed in real materials [80]. Spinodal structures were seen when

quenches in the $\alpha - T$ plane was performed by changing the temperature at a constant value of α. Thus the different microstructures (twinned and un-twinned) were obtained simply by tuning appropriate kinetic parameters, as observed in the heterogenous nucleation of colloidal crystals [81, 82]. Clearly a unified understanding of solid state nucleation along with the view towards developing a comprehensive theory is essential.

In the next part of the chapter, we look at these snapshots in greater detail with the objective of extracting general principles. We discuss these principles or "laws" of microstructure selection in the following sections. We find that the transformations occurring at high temperatures are typically accompanied by large-scale rearrangements of atoms and in this case the elasticity of the solid plays only a minor role in determining the microstructure [83]. On the other hand, at low temperatures, minimal diffusion allowing only local rearrangements of atoms are possible and the resulting microstructures are largely determined by elasticity [4]. These are just two of the myriad possibilities explored by the transforming solid. Which of these is actually selected during the nucleation and growth procedure is related to the dynamics of structural transitions. We also show that most of our results are robust with respect to variation of the potential parameters, initial and boundary conditions. Finally, we show that how the information obtained from the molecular dynamics simulations may be used to construct a simple phenomenological theory for microstructure selection.

5.2 Quenches and microstructures

There are two distinct modes of nucleation and growth of the product rhombic phase in the parent square matrix. We mainly concentrate on two quenching protocols, where the three body interaction strength v_3 is suddenly reduced from a value at which the square phase is stable to one where the rhombic phase gains stability. This is done at a constant temperature and we contrast two cases – one at low temperature (Q_1) and the other at high temperature (Q_2) (fig. 5.1).

The explanation for performing such a quench protocol is as follows. The atomistic interactions in our model are themselves coarse-grained over much faster degrees of freedom e.g. electrons and atomic magnetic (or electric) moments. In a real system, these fast

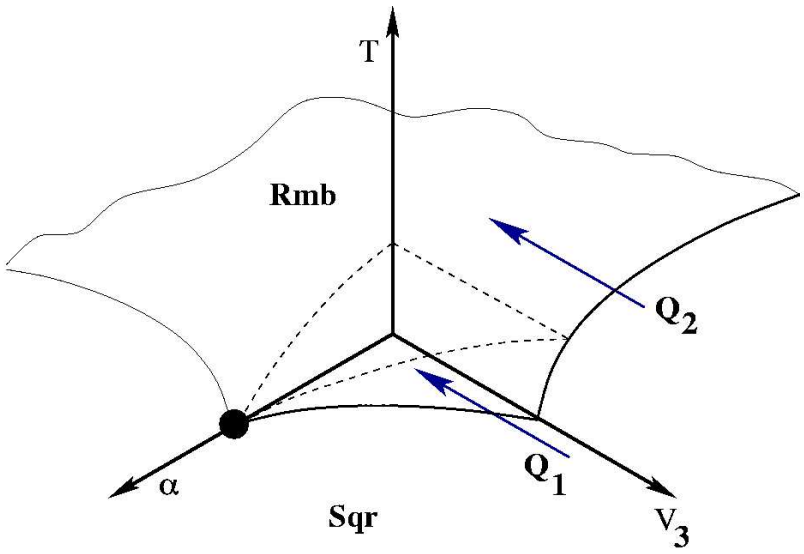

Figure 5.1: Three dimensional dynamical phase diagram in the $\alpha - v_3 - T$ plane showing the two different quenching protocols performed by varying v_3 at constant T. Q_1 represents the low temperature quenching which forms the "martensite" microstructure while Q_2 refers to the high temperature quenching forming the "ferrite" microstructure. "Sqr" and "Rmb" refer to the square and rhombic phases respectively.

degrees of freedom produces (in general) many-body interactions which finally determine the structure. For example, in Fe the face centered to body centered cubic structural transition is driven by the ferromagnetic transition of Fe [2, 84]. The time scale of variation of these degrees of freedom (the atomic magnetic moment in the case of Fe) is several orders of magnitude faster than the typical timescales of atomic motion. Isothermal transformation of steel [80] achieves exactly the conditions we have in our molecular dynamics simulations where the temperature quickly fixes the magnitude of the magnetic interactions in the Fe atoms which subsequently transforms at a fixed temperature. The three body term may also couple to external fields (eg. an electric field) in which case isothermal transformations may also be induced by changing the field. Such a mechanism has been reported for colloidal crystals [58, 59].

Square crystals, containing a single vacancy are equilibrated at large v_3. The equilibrated structure are subsequently "quenched" across the phase coexistence line to just within

the rhombic phase by varying the coefficient of the three body term v_3. Care is taken to quench the crystal into a regime where the square lattice is locally metastable for both high and low temperatures, ensuring nucleation and growth at a constant temperature and v_3. In our quench protocol, the depth of quench is adjusted so that only a single nucleus is formed. This makes our analysis substantially simpler.
Following either transformation protocols, the nucleation and growth process can be observed through the dynamics during the molecular dynamics simulations by defining a local order parameter Ω_i as follows

$$\Omega_i = \Omega_0 \sum_{jk} \sin^2(4\theta_{ijk}) \tag{5.1}$$

where the particles j and k are near neighbours to particle i and Ω_0 is chosen so that Ω_i varies from 1 (red) in the transformed phase to 0 (blue) in the untransformed phase. The simulations are performed on a system consisting of $N = 12100$ particles along with a seed located at the centre of the lattice. Details regarding the simulation has already been discussed in chapter 2 of the thesis.

5.2.1 The low temperature quench

The low temperature quenching protocol Q_1 (fig. 5.1) at $T = 0.1$ gives a "twinned" critical nucleus which grows anisotropically to form the "Martensite" microstructure, the terminology being borrowed from the microstructure of steel [2, 84]. Figure 5.2 depicts the snapshot of the anisotropically grown martensite in the parent square lattice for an isotropic potential at 4000 MD-timestep during the molecular dynamics simulation. To obtain the growing microstructure from the quenching schedule, the system was first equilibrated at $v_3 = 5$ for the isotropic potential ($\alpha = 0$). Here the system consisting of $N = 12100$ particles is seeded with a seed of strength $\delta = 1.0$ to initiate the nucleation process. Seeding the lattice refers to the introduction of a single/partial vacancy at the centre of the square configuration. δ is related to the strength of the seed *i.e.* $\delta = 1.0$ confirms a full vacancy while $\delta < 1.0$ reflects a partial vacancy. We have used various values of δ and have observed no qualitative change in the results. We discuss these in details in a separate section of the chapter. The inclusion of the seed is essential for

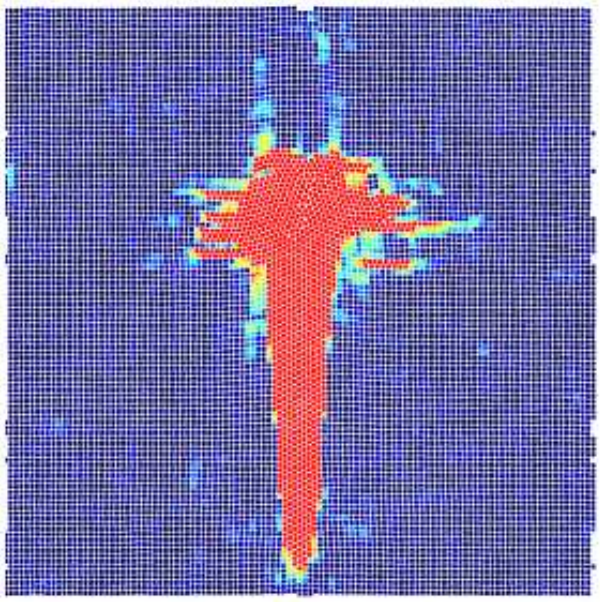

Figure 5.2: Anisotropic twinned martensite microstructure obtained from quenching an equilibrated square parent crystal composed of $N = 12099$ particles ($\delta = 1$) by changing $v_3 = 5 \rightarrow 1.65$ using an isotropic potential at $T = 0.1, \rho = 1.1, \alpha = 0$. The colours in the figure are according to the local order parameter described in eqn. 5.1.

the low temperature quench and hence in the next section we treat this inclusion as one of the basic laws to formulate the theory of microstructure selection. After complete equilibration, we quench the system to a lower value of v_3. For the isotropic case, the system at $T = 0.1, \rho = 1.1$ is quenched at $v_3 = 1.65$. A closer look into the austenite-martensite interface suggests that the martensite nucleus follows from a transformation where the local connectivity of the lattice is, to a large extent, preserved (fig. 5.3). Also the martensite nucleus is roughly elliptical consisting of a pair of twin-related crystallites.

5.2.2 High temperature quenching

The high temperature quenching protocol Q_2 (fig. 5.1) forms an isotropic critical nucleus as shown in figure. 5.4. Borrowing terminology from the microstructure in steel [2, 84], it is termed as the "Ferrite" microstructure. For the isotropic potential quench-

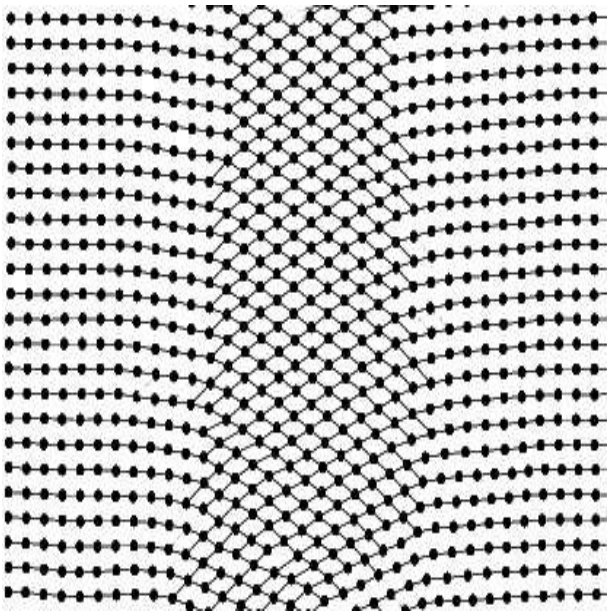

Figure 5.3: Close-up of the interface between the transformed lattice of the martensite and the untransformed lattice. It also shows the anisotropic nature of the growing microstructure.

ing schedule the system consisting of $N = 12099$ particles was previously equilibrated at $v_3 = 10, T = 0.8$ before commencing of the quench. The system is then quenched down to $v_3 = 5.5$ which gives rise to the polycrystalline ferrite. The ferrite nucleus formed is thus obtained following extensive rearrangements of atomic coordinates. At high temperatures, seeding is a matter of convenience since thermal fluctuations occuring at high temperatures are enough to initiate the nucleation and growth process.

5.3 General principles of microstructure selection

Preliminary attempts at a unifying picture [33] for microstructure selection were based on the recognition (from the MD simulations) of the role played by *non-elastic* variables, which were identified with local density fluctuations. The coupled dynamics of density fluctuations and elastic strain determines the microstructure of the growing nucleus. We extract the principles of microstructure selection using extensive molecular dynamics sim-

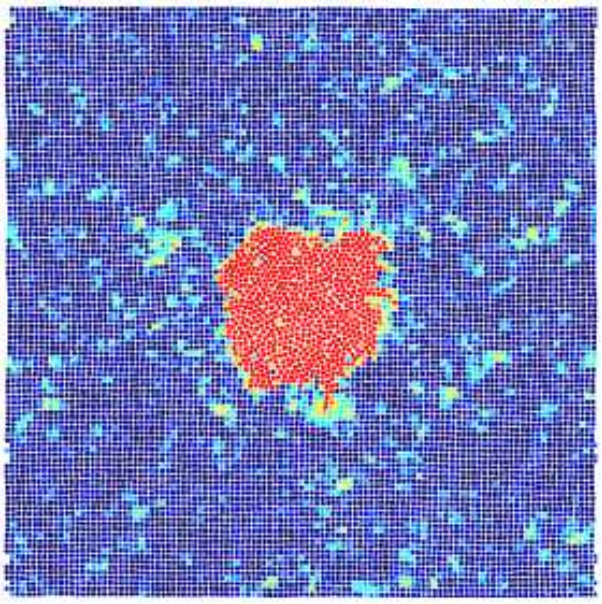

Figure 5.4: Typical product ferrite nucleus obtained from quenching an equilibrated square parent crystal composed of $N = 12099$ particles ($\delta = 1$) by changing $v_3 = 10 \rightarrow 5.5$ using an isotropic potential at $T = 0.8, \rho = 1.1, \alpha = 0$. The colours depicted in the figure show the transformed and the untransformed phases according to Ω_i described in eqn. 5.1.

ulations to study the nucleation dynamics in 'microscopic' detail. Based on the results obtained from our molecular dynamics simulations we get four generic principles for the nucleation dynamics of a solid in solid due to quenching across the structural transition phase curve [85] which we discuss one by one. It provides a more refined understanding of solid-state nucleation and microstructure selection. These principles are then further used to construct an elastoplastic theory for the dynamics of solid state transformations.

5.3.1 Principle I : Heterogenous nucleation

In the preceeding section, we have seen that microstructures are formed from the austenite phase represented by the initial square lattice as an outcome of the nucleation and growth of the critical nucleus. A typical quench process through molecular dynamics simulations initiates multiple nucleation events at higher temperatures. However, at low

temperatures the scenario is completely different in the sense that without a seed (a single vacancy), there is no nucleation and hence no structural transformation inside the lattice. Hence it is essential to introduce a nucleation seed at the centre of the lattice configuration. After equilibrating the seeded initial square configuration at a large value of v_3, quenches were performed at two different temperatures across the phase coexistence line. The results of the quenches at $T = 0.1$ and $T = 0.8$ for $N = 12099$ particles at a density, $\rho = 1.1$ are shown in fig. 5.2 & fig. 5.4 respectively. At $T = 0.1$, we get the anisotropic, twinned martensite crystal while at $T = 0.8$, isotropic, untwinned ferrite is obtained. Therefore transformations in the solid due to quenching at low temperature proceeds via heterogenous nucleation with the seed being very much essential for the initiation of the nucleation event. At higher temperatures the nucleation is homogenous in nature. Hence multiple nucleation events hinder the dynamical study of the critical nucleus and hence are not desirable. To prevent this, a seed is added to enable the formation of a single nucleus whose dynamics may be studied in detail. Hence we arrive at the first law for microstructure selection :

1. Solid state transformations predominantly proceed via nucleation. At low temperatures, the nucleation of the product solid is heterogeneous and is initiated by 'seeding' the parent.

5.3.2 Principle II : Non-order parameter and order parameter strains

To follow the dynamics in quantitative detail, we compute the coarse-grained local strain field using the procedure introduced in [37, 38, 39]. Briefly, we compare the immediate neighborhood Ω, centered around $\mathbf{r}$, of any tagged particle 0 (defined using a cutoff distance equal to the range of the potential) in the initial reference lattice (at time $t = 0$) with that of the same particle in the transformed lattice. We obtain the "best fit" local affine strain $\mathbf{e}_{ij} = \mathbf{T}_{ij} - \delta_{ij}$ ($\delta_{ij} \equiv$ Kronecker delta) which maps as nearly as possible all the particles n in Ω from the reference to the transformed lattice using an affine connection.

This is done by minimizing the (positive) scalar quantity,

$$D^2_\Omega(\mathbf{r},t) = \sum_{n\in\Omega}\sum_i \{r^i_n(t) - r^i_0(t) - \sum_j(\delta_{ij}+\mathbf{e}_{ij}) \times (r^j_n(0) - r^j_0(0))\}^2 \tag{5.2}$$

with respect to choices of affine $\mathbf{e}_{ij}$. Here, again, the indices i and $j = x, y$ and $r^i_n(t)$ and $r^i_n(0)$ are the i^{th} component of the position vector of the n^{th} particle in the reference and transformed lattice, respectively. Any *residual* value of $D^2_\Omega(\mathbf{r},t)$ is a measure of *non-affineness*. The affine shear strain e_3 measures the distortion of the initial square to the rhombus and as discussed previously is the sole OP for the transition.

Figure 5.5(a) shows the nucleation and growth of the twinned martensite nucleus, following the lower temperature quench – we have plotted the best-fit e_3 for snapshot configurations of $N = 110 \times 110$ particles at time steps of 2000, 3000, 4000 and 5000 Δt. The twinned structure of the nucleus composed of the two degenerate rhombi (characterized by positive and negative values of e_3, separated by a sharp boundary) is evident even at the earliest time, and becomes more pronounced as time progresses. The constraint of fixed density forces a dynamical coupling between the affine OP strain and the affine non-order parameter (NOP) volume strain $e_1 = \mathbf{e}_{xx} + \mathbf{e}_{yy}$, so that the transformation is also accompanied by a volume change, (fig.5.5(b)). As a result, as the transformation proceeds, more and more particles are pushed up against the surrounding untransformed square lattice which creates a *jammed* region at one end and an *unjammed* region at the other end of the anisotropic martensitic nucleus, (fig.5.5 (b)).

Therefore the second law is :

2. The dynamics of transformation is described by an affine OP strain (here, shear strain) characterizing the microstructure of the growing nucleus, and an affine NOP strain (here, volumetric strain), which is slaved to the former.

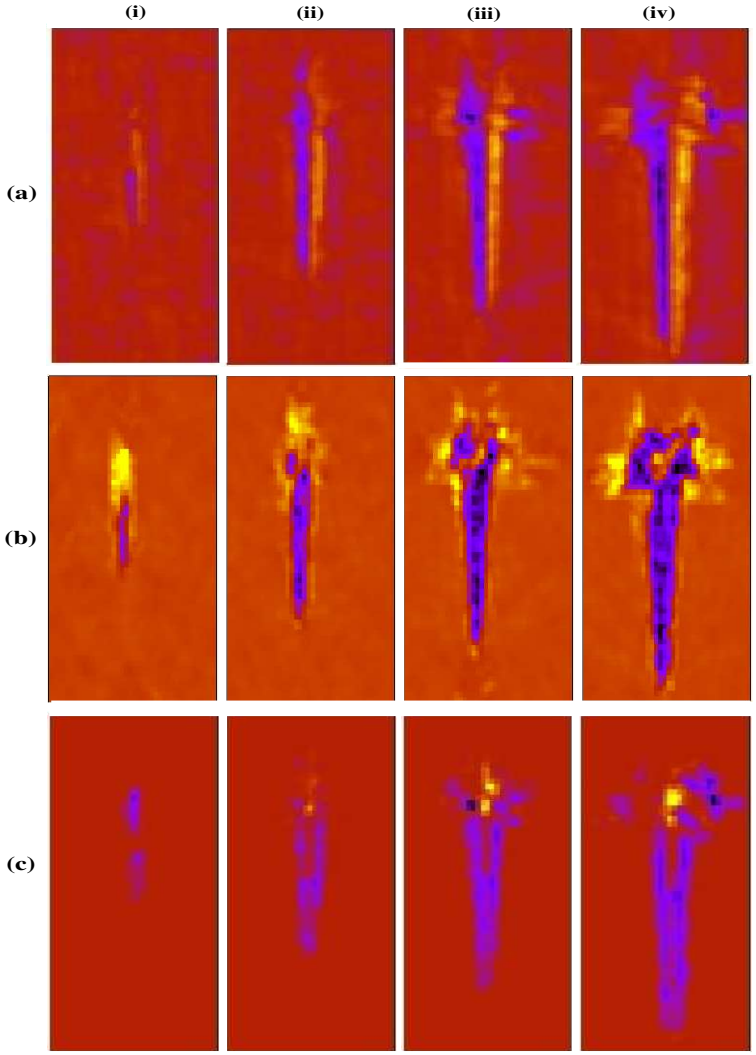

Figure 5.5: Best-fit affine strains and residual non-affine deformations, obtained from molecular dynamics simulations of particles undergoing a square to rhombic transition at $T = 0.1$, for time slices (i) 2000, (ii) 3000, (iii) 4000 and (iv) $5000\,\Delta t$. Plots obtained by coarse-graining the $N = 110 \times 110$ lattice to a 64×64 lattice. (a) Order parameter (shear) strain e_3, colors show e_3 from -0.3 (black) to 0 (brown) to 0.3 (yellow). The twinned microstructure is clearly visible, even at earlier times. (b) Non-order parameter (volumetric) strain e_1, colors show e_1 from -0.5 (black) to 0.3 (yellow). The equilibrium value of e_1 is nonzero within the rhombic phase, in addition, e_1 appears at the two ends of the twinned microstructure due to elastic coupling to the order parameter e_3. (c) Non-affine deformation χ. Colors show χ ranging from -1 to 1. Note that $\chi \to 0$ at the centre of the growing nucleus at large times. The NAZs surround the growing nucleus and are created at and advected by the front. Jammed and unjammed NAZs occur at the 'top' and 'bottom' of the nucleus, respectively, sharing the same spatial symmetries as e_1.

5.3.3 Principle III : Existence of non-affine zones associated with the growing nucleus

We can now use the residual D^2_Ω of eqn. 5.2 as introduced in the last section to extract the spatio-temporal variation of any non-affine deformation that is produced during the transformation. To be able to distinguish between non-affineness arising from different components of the strain (shear or volumetric) distortion, we need to incorporate the notion of jamming in the definition of non-affineness (eqn. 5.2). In the context of granular compaction [86] and glassy materials [87], jamming has been quantified in terms of changes in the local free-volume relative to the reference state. In our context, this translates into computing the relative change in the distance between particles within Ω in the direction of motion of the particles in the nucleus, denoted by Δl; we may thus define a quantity $\chi(\mathbf{r}, t) = -D^2 \,\mathrm{sign}(\Delta l)$, which takes both positive (jammed) and negative (unjammed) values. For the martensite nucleus, the jammed and unjammed non-affine zones (NAZs) are shown in fig. 5.5 (c); as the transformed region grows, χ is localized and advected by the transformation front. Note that the spatial symmetries of χ are the same as that of e_1 at all times (compare figs. 5.5 (b) and (c)), and so we associate the non-affineness predominantly with the NOP or volumetric strain. This restriction of non-affineness to the NOP strain alone, could be specific to the square-to-rhombus transition; in transitions between other structures, there could be a fair degree of plasticity associated with the OP strain too. We deal with this point in chapter 7 (see also Ref. [88, 89]). Consistent with geometrical theories, the NAZs are absent at the twin interface; this interface is coherent and the twins are simply related to each other by an affine transformation.

In contrast, fig.5.6 (a) shows the nucleation and growth of the ferrite nucleus, following the higher temperature quench – as above, we have plotted the best-fit e_3 for snapshot configurations of $N = 110 \times 110$ particles at time steps of 8000, 10000, 13000 and 15000 Δt. The nucleus is composed of polycrystalline grains of the rhombic phase separated by large angle grain boundaries. As time progresses, the grains rotate with respect to each other, giving rise to large non-affine distortions *even in the bulk of the nucleus*. This is reflected in the large values of χ in the bulk of the growing nucleus, fig. 5.6 (b). However, a spatial average of the instantaneous values χ and e_3 over a scale larger than the grain size, gives zero for both. Similarly, a time average of the local χ and e_3 over a window

corresponding to typical grain reorganization times, gives zero for both. The plastic zone spreads throughout the product region causing extensive atomic rearrangements.

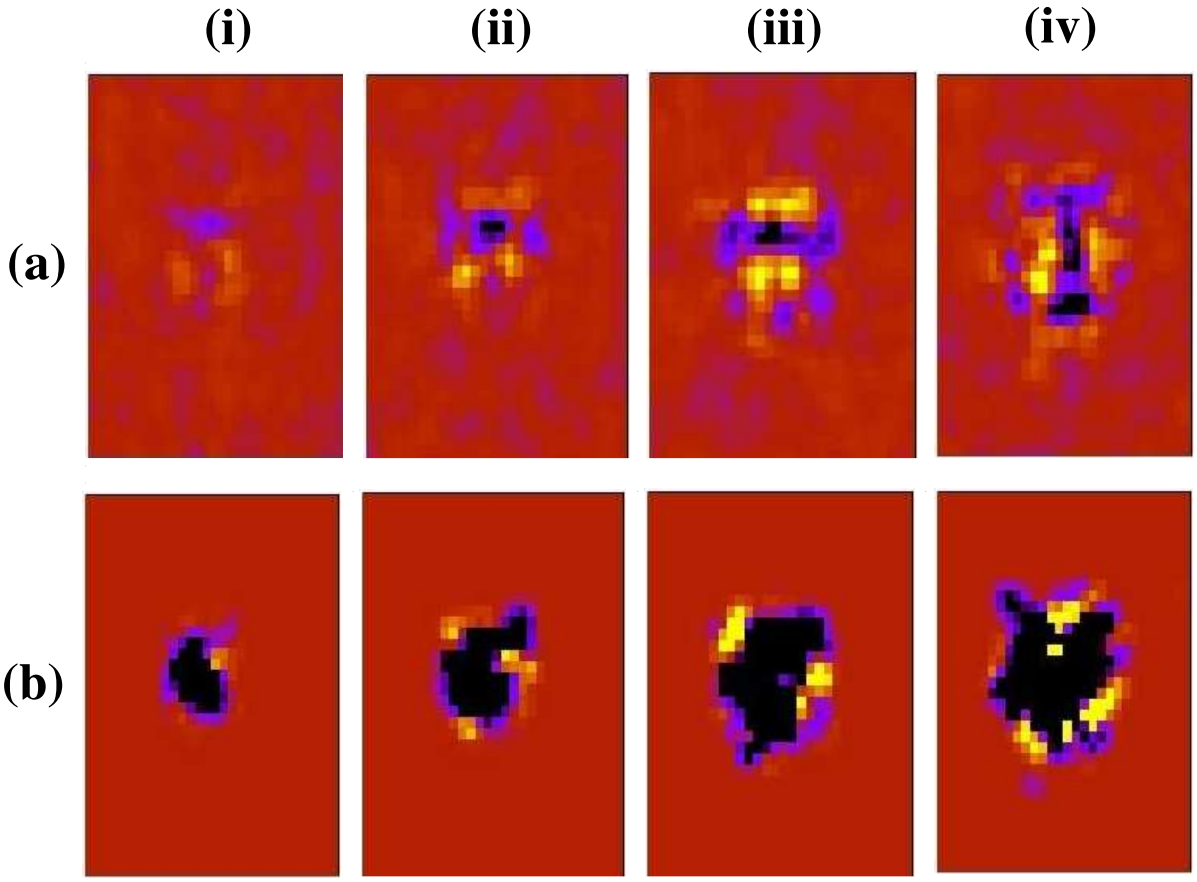

Figure 5.6: Best-fit affine strains and residual non-affine deformations, obtained from molecular dynamics simulations for a quench at $T = 0.8$, for time slices (i) 8000, (ii) 10000, (iii) 13000 and (iv) $15000\,\Delta t$. Same coarse-graining as in fig.5.5. (a) Order parameter (shear) strain e_3, colors show e_3 from -0.3 (black) to 0.3 (yellow). Note that unlike the martensite, no clear spatial pattern in e_3 can be discerned. The local structure of the product nucleus is polycrystalline, with individual grains which coarsen with time. (b) Non-affine deformation χ, colors show χ ranging from -1 to 1. Note that non-affine regions are present throughout the interior of the nucleus, signifying extensive plastic deformation during growth.

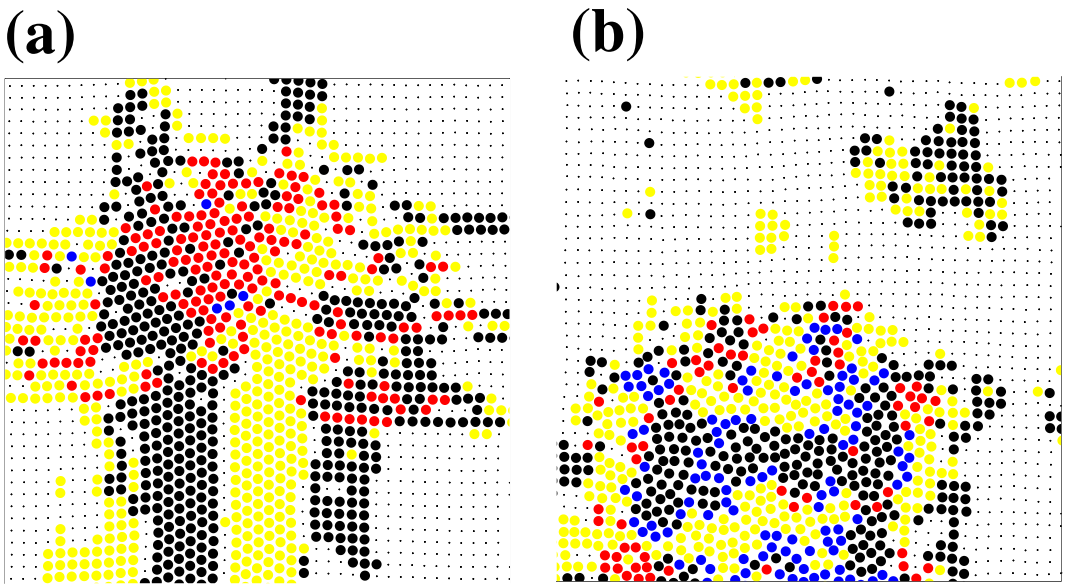

Figure 5.7: Close up of a region from the nucleus (a) in martensite : corresponding to fig.5.5(iii) and (b) ferrite : corresponding to fig.5.6(iv). The color code is as follows: black dots – untransformed regions; yellow and black circles – affine regions with +ve and −ve e_3; red and blue circles – jammed and un-jammed non-affine regions. In (a) a similar non-affine region arises at the other (bottom) end of the twinned region (not shown).

We now take a closeup look at the NAZs – fig.5.7(a),(b) shows snapshots of the atomic positions in the NAZs of the martensite and ferrite nucleus, respectively. It is clear that the atomic configurations in the NAZs are highly amorphous, with no clear relation to the reference parent lattice. It seems meaningless to describe NAZs in terms of a density of dislocations, since the reference state has no unique physical significance for characterizing the current state in the NAZs. Even if we were to describe the state of NAZs in terms of dislocations, the density of dislocations would be so high as to have overlapping cores, thus rendering this language inadequate. It is more reasonable to describe the NAZs in terms of fluctuations in the local density $\Phi(\mathbf{r},t) = (\rho(\mathbf{r},t) - \rho_0)/\rho_0$, where $\rho(\mathbf{r},t) = \sum_{n\in\Omega} \delta(\mathbf{r} - \mathbf{r}_n(t))$, and ρ_0 is the average uniform density. This quantity includes density fluctuations due to both affine as well as non-affine contributions coming from defects (vacancies/interstitials and dislocations). Indeed in [33], the authors had studied the dynamics of $\Phi(\mathbf{r},t)$ in great detail and demonstrated its involvement with dynamics of

transformation and microstructure selection. Φ was shown to be concentrated at the two ends (top and bottom) of the growing martensite nucleus, being advected by the transformation front. The authors argued that the mode of relaxation of Φ determined whether a Martensite or ferrite nucleus is formed. Specifically, a rapidly relaxing Φ produces an isotropic ferrite nucleus at high temperatures while at low temperatures, when Φ is advected without relaxation by the transformation front, a twinned, anisotropic Martensite nucleus is formed. Here we find by explicit computation that Φ and χ are related – localized regions with large Φ correspond to large χ and so on.

3. Right from its initiation, the transformation is accompanied by non-affine deformations primarily associated with NOP (here volumetric) strain. The dynamics of non-affine deformations determines the microstructure.

The distinguishing features of these NAZs, in summary, may therefore be set down as follows :

- The non-affine regions located at the two ends of the growing martensite microstructure comprises of large variations of local density in space and time. This finally results in jammed and unjammed regions (fig. 5.8) at the two extremities of the microstructure.
- Computation of the radial distribution function, $g(r)$ of the NAZ reflects an effectively liquid-like structure in both martensite (fig. 5.9 (a)) and ferrite (fig. 5.9 (b)) microstructure.
- Voronoi construction of the non-affine regions present in both martensite and ferrite microstructures are shown in fig. 5.10 (a) and (b) respectively. It shows high density of dislocations/disclinations comprising of $5-7$ neighbour particles.
- Such a highly defective structure implies that defect cores overlap and hence description in terms of individual defects fails.
- High effective temperature is evidenced from the disordered structure implying higher rate of diffusion.

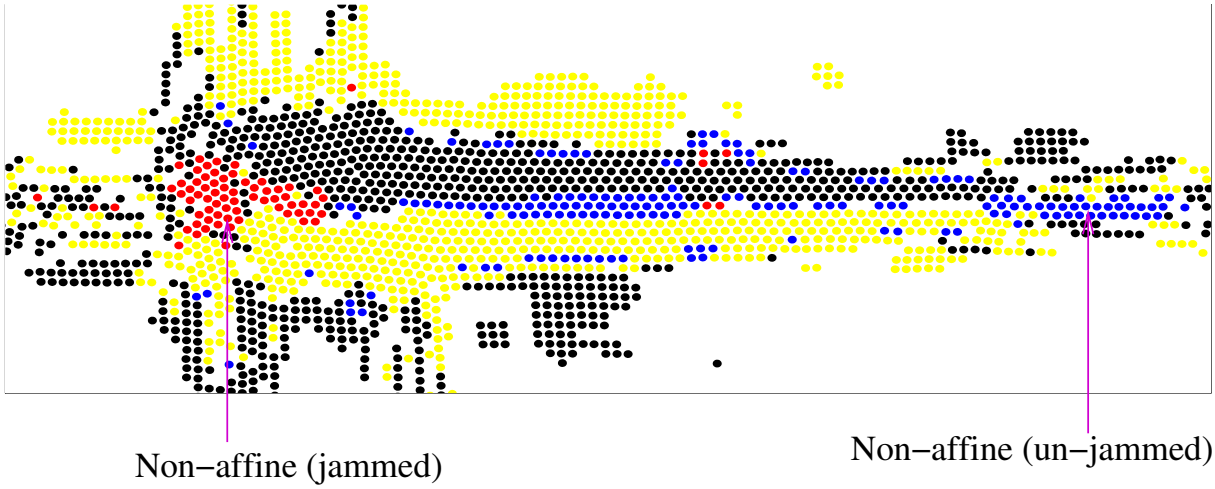

Figure 5.8: The Martensite twin structure depicted by positive and negative values of e_3 symbolised by yellow and black dots respectively. The red and blue dots at the two ends of the structure show the jammed and unjammed regions formed during the growth of the anisotropic nucleus.

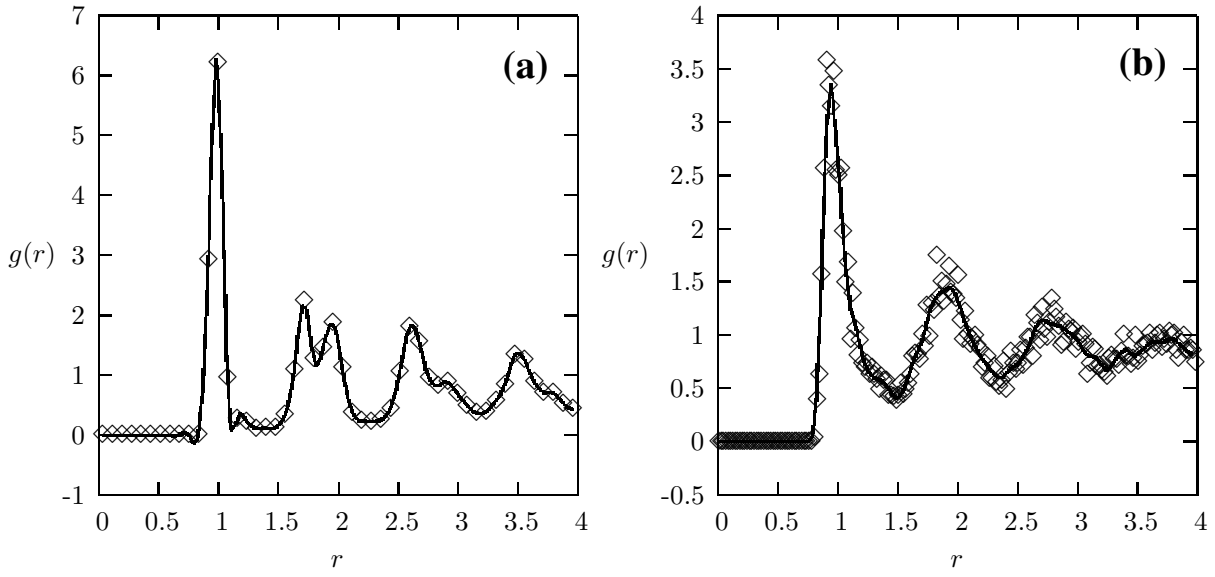

Figure 5.9: Radial distribution function, $g(r)$ for the martensite (a) and ferrite (b) microstructure.

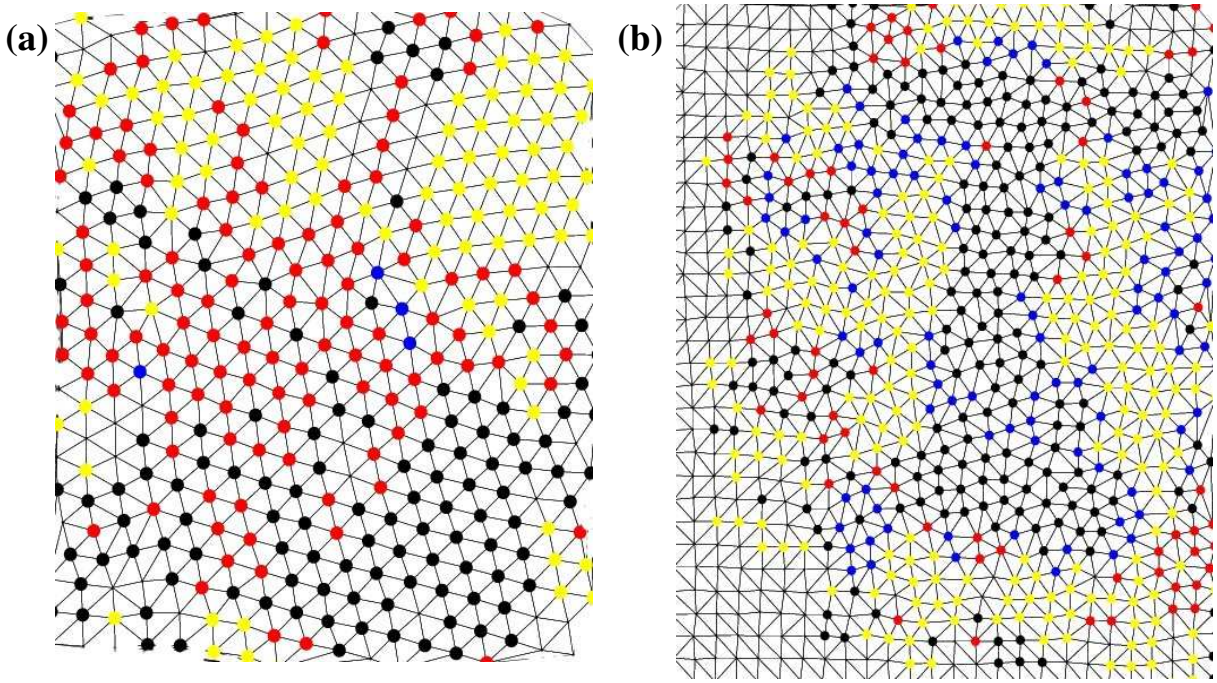

Figure 5.10: Voronoi construction of the non-affine regions present in the martensite (a) and ferrite (b). It shows the presence of $5-7$ neighbour particles in both types of microstructure.

- The above features are observed in NAZ for both types of microstructures. The distinguishing factor between the two is that in case of the ferrite, NAZ is more extensive, more disordered and hence has higher effective temperature.

5.3.4 Principle IV : Dynamics of formation of non-affine zones

We will now show that NAZs are produced when the local volumetric stress exceeds a threshold value. We compute the instantaneous local stress from our simulations by spatially averaging the generalized virial,

$$\sigma_{ij} = \langle \sum_{n \in \Omega} \mathbf{F}_i \mathbf{r}_n^j \rangle$$

over cells Ω_M containing M particles where $1 \ll M < N$. The choice of M is dictated by the mutually competing considerations of proper averaging and obtaining information over a fine enough length scale. We have chosen $M = 100$ as a compromise between these

considerations. Further, in order to obtain good statistics for any time t, we average over many independent quenches. The spatio-temporal resolution of the computed σ is however not as high as the one for the coarse-grained strain $\mathbf{e}$. In the NAT ensemble, the spatial average of the volumetric stress σ_1 is related to the thermodynamic pressure as $\sigma_1 = -P(\rho, T) \neq 0$.

We now compute the local volumetric stress σ_1, affine volumetric strain e_1 and non-affine χ, averaged over the coarse-grained cell Ω_M, at different times following the quench. This is plotted in fig. 5.11 (a), (b), where we have expressed the local stress as a fractional difference about the value of σ_1 for $e_1 = 0$, viz., the undistorted region. The σ_1-e_1 plot shows a linear elastic regime for those coarse-grained cells where the strain e_1 is small; concomitantly the non-affine χ is zero (fig. 5.11 (c), (d)). Coarse-grained cells where e_1 is larger than a threshold, show yielding (nonlinear and erratic σ_1-e_1) and appreciable plastic flow, $\chi \neq 0$. We have verified that these coarse-grained cells showing plastic deformation are indeed the NAZs reported above.

There are two distinct regions in each of these plots, an elastic regime for small strains and for larger strains a regime of plastic flow followed by failure. Going back to the particle configurations, we verify that the elastic region corresponds to the distortion of the parent matrix in the untransformed region. The region of plastic flow corresponds to the transformation front, specifically the NAZs. While, in the martensite case, the elastic response is sharply linear and virtually independent of time, the ferrite yields at slightly smaller strains at later times. The maximum and minimum stresses in the plastic regime is the same and appears to be only weakly dependent on temperature with the values for the ferrite case somewhat larger than the martensite. This is a simple consequence of the fact that the total pressure itself increases with temperature for the same density.

We now focus on one coarse-grained cell, and study the time development of σ_1, e_1 and χ as the transformation proceeds (fig. 5.12). We find that at earlier times, the strains are small and the stress-strain response is elastic. Beyond a yield stress σ_{1c}, the stress-strain relation is nonlinear, giving rise to non-affine deformations $\chi \neq 0$. Following yielding, the local stress eventually decreases, often exhibiting oscillatory behavior. We find that the threshold stresses σ_{1c}, when expressed as a fraction of the ambient stress is only weakly dependent on temperature.

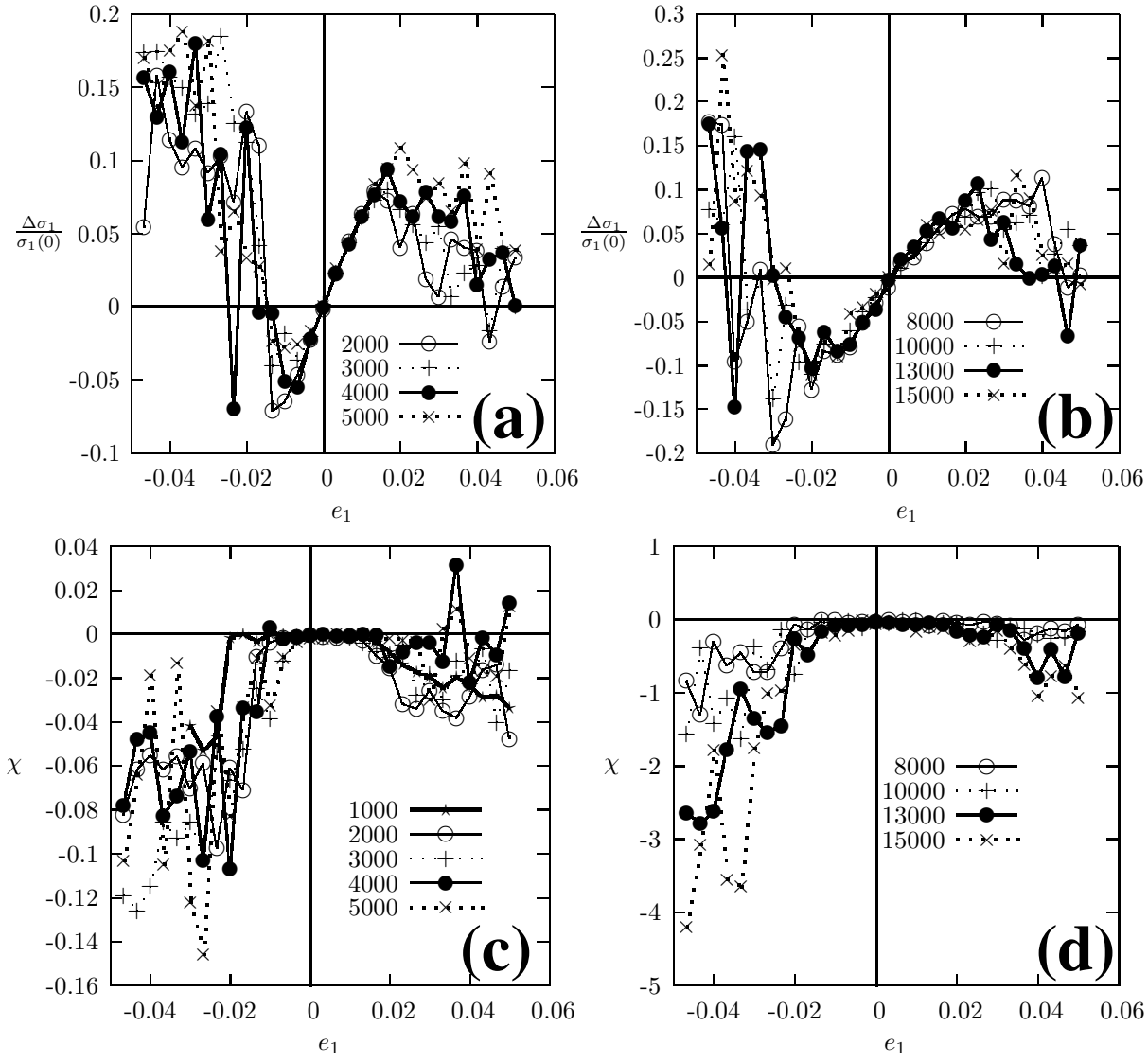

Figure 5.11: Local stress expressed as a fractional difference from the volumetric stress at $e_1 = 0$ ($\Delta\sigma_1/\sigma_1(0)$), plotted against the local strain at different times (symbols) obtained for the (a) quench at $T = 0.1$, averaged over 40 independent quenches, and (b) quench at $T = 0.8$, averaged over 35 independent quenches. (c) and (d) are corresponding plots of χ vs e_1. The linear Hookean regime represents the local elastic response at small local stress. Beyond a threshold, the system *yields* locally, giving rise to a nonlinear stress-strain behavior *and* simultaneously non-affine deformations $\chi > 0$. The regions in real space associated with this local plastic regime are identical to the NAZs. The contribution to (c) and (d) comes predominantly from unjammed regions due to the (negative) volume change which accompany the transformation.

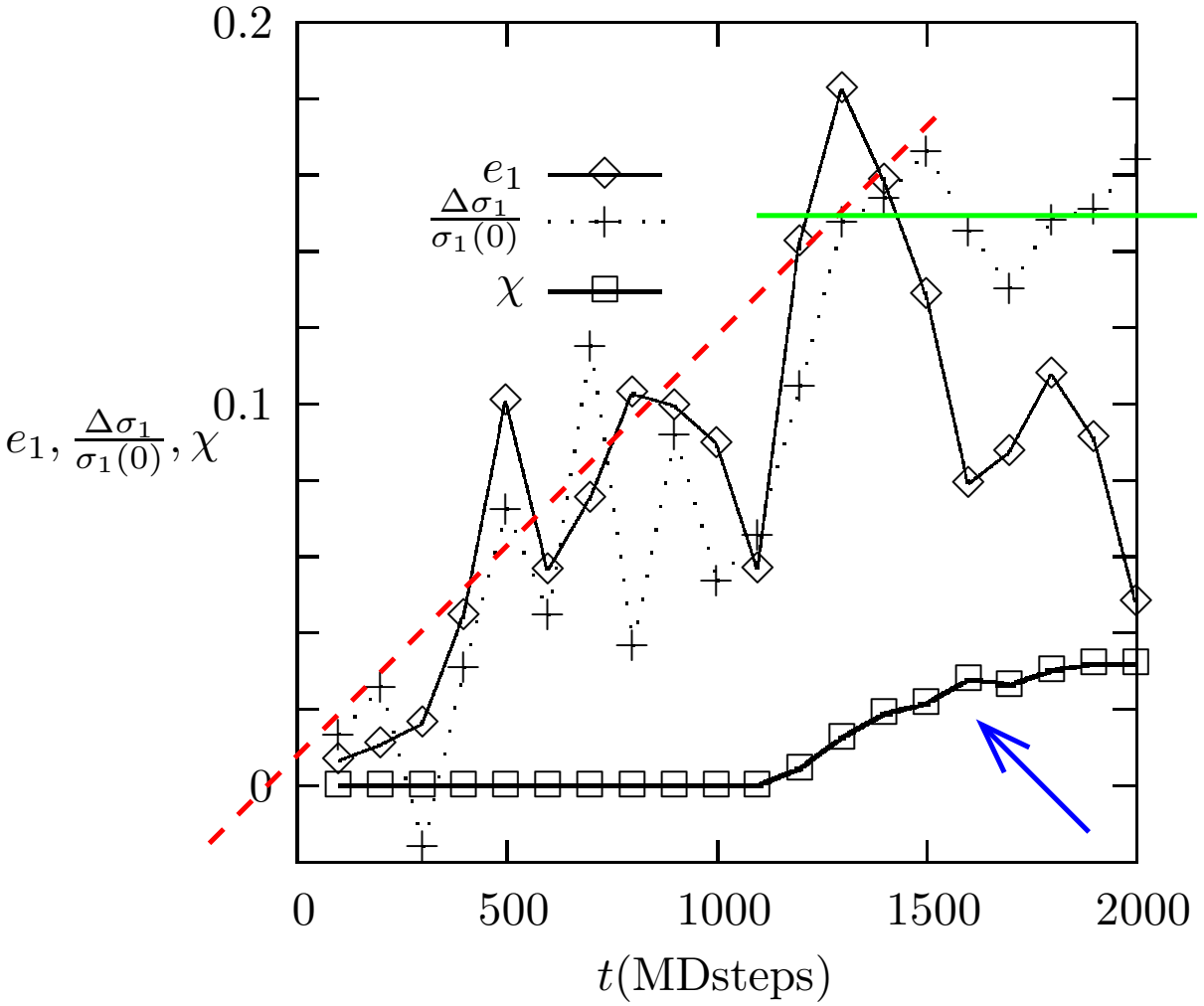

Figure 5.12: Time dependence of local stress $\Delta\sigma_1/\sigma_1(0)$, strain e_1 and χ near the growing nucleus within a jammed region after a quench at $T = 0.1$. Note that initially $\chi = 0$ and the stress (apart from large statistical fluctuations) is proportional to strain. The thick red dotted line in the figure represents the Hooke's Law regime. When the local stress exceeds a threshold denoted by the thick green line, χ begins to increase, and the stress versus strain is highly nonlinear. The blue arrow shows the region of plastic flow.

4. Non-affine deformations are produced when the local stress crosses a threshold. The threshold stress is only weakly dependent on temperature.

While the general nature of the stress-strain curves are similar to material deformation or loading experiments showing plastic flow and failure in materials under *external* stresses or when deformed with a constant externally imposed strain rate [40], there are some very important differences. First of all, unlike the loading experiments, the stress calculated in our case is *not* a quantity which is in thermodynamic equilibrium. However, local *mechanical equilibrium*, which translates to just the force balance condition for every internal point within the sample, is satisfied. Secondly, the strain e_1 in this case is internally generated by the transformation strain e_3 due to elastic coupling between the components of the strain tensor. Lastly, for deformation under external stress or strain rate, plasticity is associated with irreversibility. This is not true in the present case since the NAZs are dynamical objects similar to STZs in Refs. [37, 38, 39, 40]. As the transformation front sweeps through a region, the sequence of transformations is; undistorted region $\rightarrow$ elastic distortion $\rightarrow$ NAZ $\rightarrow$ transformed region. At late times, the entire system is transformed to the product phase and plastically deformed regions cease to exist. Note that, the NAZs are primarily associated with the non-order parameter sector of the strains. Plasticity in the order parameter sector on the other hand can and does lead to irreversibility. We investigate this issue in detail in chapter 7. In the martensite, the plastic zone which is associated with the NAZs, are advected with the front, and in our finite simulation box with periodic boundary conditions anihilate each other. In the ferrite case the plastic zone spreads throughout the product region causing extensive atomic rearrangements.

In the next section we shall show that the development of the microstructure is crucially influenced by the dynamics of the NOP plastic strain associated with the NAZs within a dynamical coarse grained field theory involving both elastic and plastic strains. These principles $1-4$ highlighted above, will form the basis of our construction of an elastoplastic theory for the dynamics of solid state transformations. We believe that they are generic, independent of the choice of potential or the nature of the transformation.

5.4 Principles of microstructure selection: Robustness with respect to variation of potential parameters, initial conditions and ensembles.

In this section, we repeat the quench protocols presented in the earlier section for a variety of potential parameters, initial conditions and boundary conditions/ensembles. Our objective is to find out the domain of validity of the general principles of microstructure selection as extracted by us from our earlier simulations. We shall first consider making the two body potential anisotropic (*i.e.* $\alpha \neq 0$), then change the initial conditions which induces heterogenous nucleation and finally we shall consider replacing periodic with open boundary conditions. The last modification leads to new phenomena and will be discussed in further detail in chapter 7.

5.4.1 Quenching with anisotropic potential

As discussed in chapter 2, the two body term V_2 in the two dimensional model potential (eqn. 2.2) contains the anisotropy parameter α which plays an important role in varying the jump in the order parameter in case of first order transitions to continuous transitions. The nucleation and growth procedure which forms the different microstructures were previously studied considering the isotropic potential with $\alpha = 0$. We perform similar low and high temperature quench protocols now using a non-zero value of α. The low temperature quench at $T = 0.05$ is performed by first equilibrating a square lattice at $v_3 = 10$ with $\alpha = 1$. The system contains $N = 12100$ particles with a seed of strength $\delta = 1$ at $\rho = 1.1$. After complete equilibration, it is quenched to $v_3 = 0.34$.

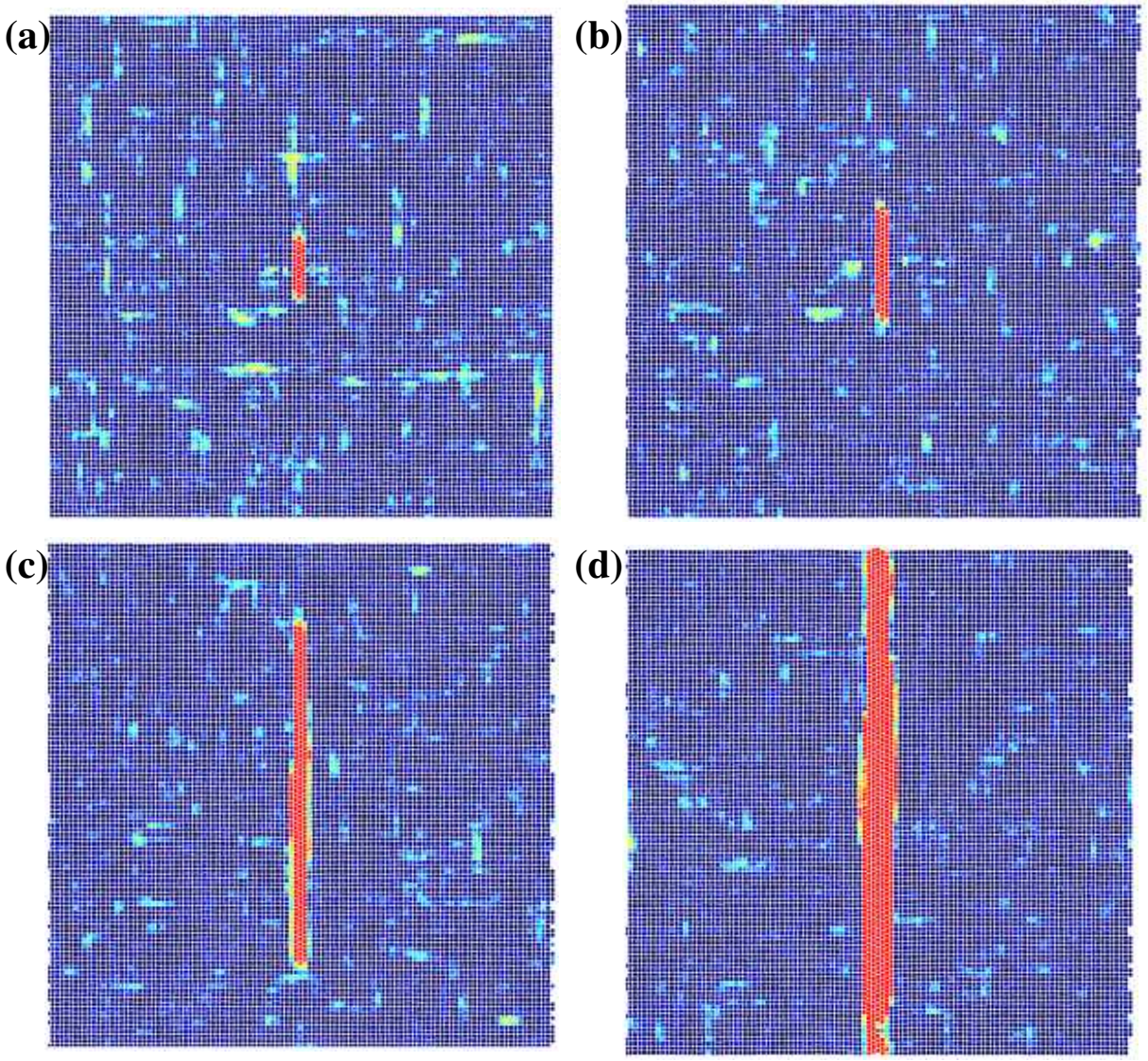

Figure 5.13: Typical molecular dynamics simulation snapshots at (a) 1200 (b) 2000 (c) 5000 and (d) 10000 MD-timesteps showing the growth of a twinned martensite critical nucleus at a low temperature, $T = 0.05$ quenched at $v_3 = 0.3383$. The equilibrated square parent lattice at $\rho = 1.1$ has particles interacting via the anisotropic potential with $\alpha = 1$. The colourscale goes from $\Omega_i = 0$ (blue) representing the untransformed austenite to $\Omega_i = 1$ (red) pertaining to the transformed martensitic microstructure.

As seen from the molecular dynamics snap-shots in fig. 5.13, an anisotropic twinned critical nucleus develops and gradually grows to form the martensite microstructure. The high temperature quench protocol is performed at $T = 0.6$ for the same system of $N = 12100$ particles with $\delta = 1, \alpha = 1, \rho = 1.1$. The system is equilibrated at $v_3 = 5$ and quenched to $v_3 = 1.1$. Fig. 5.14 shows the nucleation and growth of an isotropic ferrite nucleus. Thus we conclude that as long as the value of α considered gives $\Delta e_3 > 0$ at

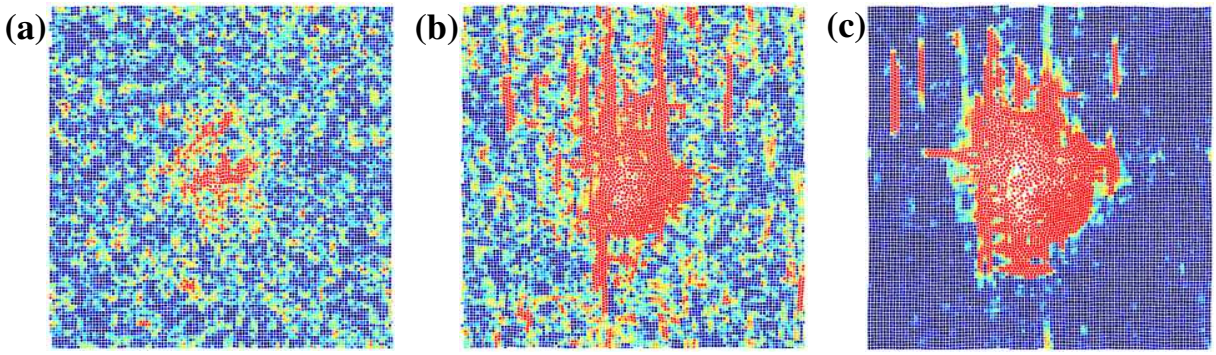

Figure 5.14: Molecular dynamics snapshots at (a) 100 (b) 1200 (c) 2500 time-steps showing the growth of an isotropic critical nucleus at a high temperature, $T = 0.6$ quenched at $v_3 = 1.1$. The equilibrated square parent lattice is subjected to an anisotropic potential with the value of $\alpha = 1$ and $\rho = 1.1$. The colourscale for Ω_i is the same as described in fig. 5.13.

the transition, the outcome of the quenching schedules are same for both isotropic and anisotropic potentials. Notably, however, the anisotropy of the twinned nucleus which results from the low temperature quench seems to increase with α.

5.4.2 Quenching with a soft seed

The necessity of a seed in the nucleation event at low temperatures and also at high temperatures forms one of the basic laws of microstructure selection. However, the strength of the seed may be varied as follows. It consists of replacing the central particle with a particle whose size σ is smaller than that of the rest of the particles of size σ_0. The strength of the seed can be varied by a factor δ where $\delta = (\sigma_0 - \sigma)/\sigma_0$. To obtain nucleation within reasonable computation times we take $0.25 \leq \delta \leq 1$. Thus δ equal to

0.25 and 1 produces a soft and a hard seed respectively. Here we present our results for quenches at both low and high temperatures using a soft seed of strength $\delta = 0.26$ in a system consisting of $N = 12100$ particles at $\rho = 1.05$.

Considering the isotropic potential with $\alpha = 0$, we equilibrate the initial square lattice at $v_3 = 5, T = 0.1$. To perform the quench, v_3 is reduced to 1.47 keeping the other parameters fixed. Fig. 5.15 shows the anisotropically growing twinned martensite nucleus at various timesteps during the MD simulation. To perform the high temperature quench,

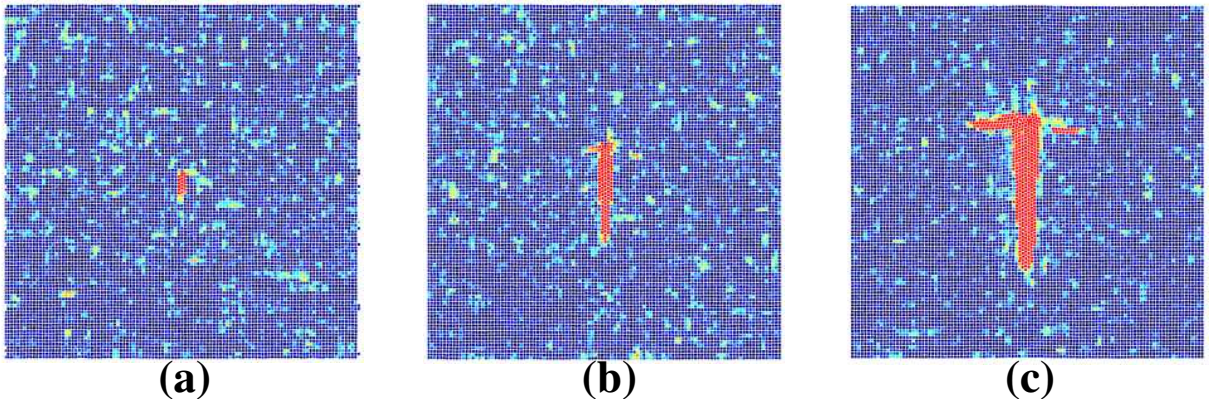

Figure 5.15: Typical molecular dynamics snapshots showing the development of the anisotropic twinned martensite nucleus obtained as a result of quenching across the phase curve in the $v_3 - T$ plane. The quenching was done for isotropic potential with $\alpha = 0$ at $\rho = 1.05, v_3 = 1.47, T = 0.1$ for $N = 12100$ particles along with a seed of strength $\delta = 0.26$. The colour scale in the picture goes from $\Omega_i = 0$ (blue) representing the untransformed austenite square lattice to $\Omega_i = 1$ (red) pertaining to the transformed martensite microstructure. (a), (b) and (c) are the snapshots at $3700, 6200$ and 8400 MD-timesteps respectively.

the system with the soft seed was equilibrated at $v_3 = 10$ and then quenched to $v_3 = 3.5$ at $T = 0.8$. As expected, we obtain the isotropically growing ferrite nucleus (fig. 5.16).

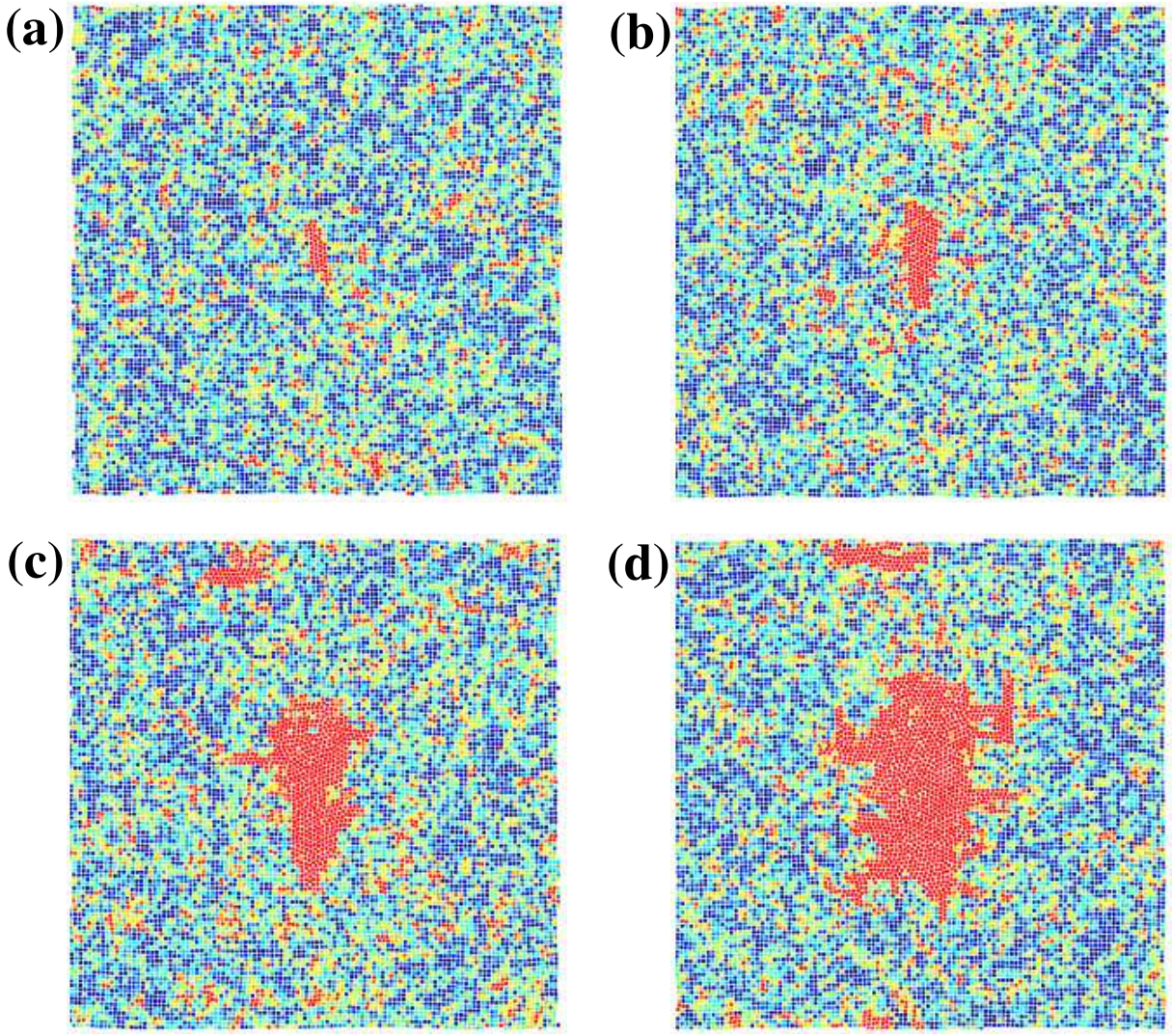

Figure 5.16: Typical molecular dynamics snapshots showing the nucleation and growth of the isotropic ferrite nucleus obtained as a result of quenching across the phase curve in the $v_3 - T$ plane. The parameters for the quench are as follows: $\alpha = 0, \rho = 1.05, v_3 = 3.5, T = 0.8$. The system consisting of $N = 12100$ particles along with a seed of strength $\delta = 0.26$ was equilibrated at $v_3 = 10$. The colour scale in the picture goes from $\Omega_i = 0$ (blue) representing the untransformed austenite square lattice to $\Omega_i = 1$ (red) pertaining to the transformed ferrite microstructure. (a), (b), (c) and (d) are the snapshots taken at $2500, 4000, 7500$ and 10000 MD-timesteps respectively.

Thus the features of the microstructures obtained as a result of the quenches remain undisturbed due to the inclusion of the seed and its strength variation in the lattice system.

5.4.3 Open boundary conditions

The glue potential as would be introduced in chapter 7 removes the restriction of the periodic boundary conditions and allows overall shape changes in the system with open boundary conditions in both directions. Accounting for the glue potential helps to analyse the system in the constant stress ensemble ($N\Sigma T$). To study the system in such an environment requires large system sizes and larger computational resources. As the overall shape of the system changes, the nucleation and growth process becomes completely different from that described earlier. Even with a seeded lattice we get surface nucleation and hence the development of the microstructure becomes cumbersome. Although NAZs are produced during the quench process but their evolution differs from those obtained previously. However a detailed study of the system with the glue potential leading to shape changes and non-affine deformations is described in chapter 7.

5.5 Elasto-plastic theory of nucleation dynamics of solids

In this last section of the chapter, we briefly show how the four principles derived from our molecular dynamics simulations may be used to construct a phenomenological "elasto-plastic" theory for microstructure selection [88] which shows many qualitative features similar to those seen in the simulations.

5.5.1 Elastoplastic theory : square to rhombus transformation

The specific square to rhombus transformation, is described by two OP strains characterizing the four degenerate product phases. Construction of Landau theory for this transition (refer chapter 3) uses terms up to sixth order on OP strains $e_T^A = \{e_2, e_3\}$ and quadratic in NOP strain $\mathbf{e}_V \equiv e_1$. We decompose the NOP strain into a slaved, affine NOP strain $\mathbf{e}_V^A \equiv e_1^A$, and a dynamical non-affine NOP strain $\mathbf{e}_V^P \equiv e_1^P$, enabling the total

NOP strain to be written as, $e_1 = \mathbf{e}_1^A - \mathbf{e}_1^P$. In order to compare with the results and phenomenology of the molecular dynamics simulation of the model solid, we look at a restriction of this problem. Recalling that our microscopic potential supports *two* rather than the possible four product minima [85] the choice of potential has therefore only *one* minimum in the e_2 direction. It thus suffices to retain upto quadratic terms in e_2 in the strain free-energy functional. The minimal free-energy functional, sufficient to describe this square to rhombus transition is given by,

$$\begin{aligned}\mathcal{F} &= \frac{1}{2}\int \mathrm{dxdy}\,\Big[a_1(e_1+e_1^P)^2 + a_2e_2^2 + a_3e_3^2 \\ &\quad + c_1(\nabla(e_1+e_1^P))^2 + c_2(\nabla e_2)^2 + (\nabla e_3)^2 - e_3^4 + e_3^6\Big] \end{aligned} \tag{5.3}$$

in terms of the OP strains e_3 and e_2 and the NOP strain e_1. The only other term to quadratic order in e_2, viz., $e_2^2e_3^4$ has been dropped as it does not influence the phase transition. The three elastic constants $a_1 = K_{11} + K_{12}/2, a_2 = K_{11} - K_{12}/2, a_3 = 2K_{44}$ define the linear elasticity of the square phase with K_{11}, K_{12} and K_{44} being the conventional elastic constants of a solid with square symmetry [69]. The coefficients of the quartic and sixth order terms as well as that of ∇e_3 can be scaled to unity by rescaling e_1, $\mathcal{F}$ and the spatial coordinates (x, y). They may also be obtained for our specific model from appropriate $T = 0$ calculations as shown in chapter 3. The coefficient a_3 represents the degree of under-cooling. We work in a parameter range where the square crystal is metastable and the rhombic crystal is stable at equilibrium. Note that all the parameters in eqn. 5.3 may be obtained for any particular material by fitting experimental neutron scattering data [22, 23, 24] or data obtained from computer simulations or derived from a microscopic non-affine field theory [90]. The affine NOP strain is slaved to the OP strains; we make use of the conditions of mechanical equilibrium ($\nabla \cdot \sigma = 0$), and the St. Venant compatibility condition [1, 91] to express e_1^A in terms of e_2 and e_3,

$$\nabla \times (\nabla \times \mathbf{e})^\dagger = \nabla^2 e_1 - (\nabla_x^2 - \nabla_y^2)e_2 - 4\nabla_x\nabla_y e_3 = 0\,. \tag{5.4}$$

The relation between the total NOP strain e_1 and the OP strains $e_j, j = 2, 3$ is most conveniently expressed in $\mathbf{k}-$space,

$$\tilde{e}_i(\mathbf{k}) = \tilde{\mathcal{Q}}_{ij}(\mathbf{k})\,\tilde{e}_j(\mathbf{k}) \tag{5.5}$$

with the kernels,

$$\begin{aligned}\tilde{\mathcal{Q}}_{13}(\mathbf{k}) &= \frac{4a_2 - 2a_3}{a_1 + a_2}\,\frac{k_x k_y}{k^2} \\ &= q_{13}\frac{k_x k_y}{k^2}\,, \end{aligned} \tag{5.6}$$

and

$$\begin{aligned}\tilde{\mathcal{Q}}_{12}(\mathbf{k}) &= -\frac{a_3 - 2a_2}{2a_1 + a_3}\,\frac{k_x^2 - k_y^2}{k^2} \\ &= -q_{12}\frac{k_x^2 - k_y^2}{k^2}. \end{aligned} \tag{5.7}$$

In effect, the above equations connect the instantaneous e_1^A to the dynamical e_1^P, e_2 and e_3. We now specify the dynamics for the OP strains and the plastic NOP strain. At this stage we make the approximation of replacing the value of the OP e_2 by its value at equilibrium, i.e., $e_2 = 0$ for all times. This greatly simplifies the calculation without changing the physics. The dynamical equation for the affine OP strain e_3 may be derived from Newton's laws [22, 23, 24] incorporating dissipation via a Rayleigh dissipation functional [69],

$$\frac{\partial^2 e_3}{\partial t^2} = \nabla^2\left[\frac{\delta\mathcal{F}}{\delta e_3} + \gamma'\frac{\partial e_3}{\partial t}\right], \tag{5.8}$$

where γ' is a solid shear viscosity.

The dynamics of the plastic NOP strain are determined by the phenomenological equation,

$$\begin{aligned}\dot{e}_1^P &= \frac{1}{h_1}\;\sigma_1 \qquad\qquad \text{if } |\sigma_1| > \sigma_{1c} \\ &= 0 \quad \text{otherwise} \end{aligned} \tag{5.9}$$

where the local stress $\sigma_1 = \delta\mathcal{F}/\delta e_1$ and we have, for simplicity, chosen the 'Newtonian' ansatz with a simple threshold criterion, with yield stress σ_{1c}. σ_{1c} is a material dependent stress threshold.

We solve the dynamical equations (5.8) and (5.9) numerically; details of the computation and the results obtained are provided below.

The algorithm used is based on a simple real space scheme to obtain the numerical solution of the partial differential equations (5.8) and (5.9). This involves discretizing over a lattice of square cells of size $\delta x = 1$. We have used 128×128 cells to obtain the phase diagram (fig.5.17) and 512×512 cells for figs. 5.18, 5.19 and 5.20. The initial value problem in time is solved using an Euler scheme with a time step of $\delta t = 0.002$ which is sufficient to avoid numerical instabilities. The sequence of steps involved in the iteration of the discretized equations is given in Appendix C.

In order to mimic the molecular dynamics simulations as closely as possible, the dynamics is initiated by seeding the square phase with a tiny elliptical, twinned nucleus without any imposed randomness or noise. As in the simulation, we first obtain a dynamical phase diagram demarcating the regions where a martensite or ferrite is obtained upon quenching. This is done by studying the shape of the nucleus, in terms of the shape asphericity A and twinning of the microstructure, in terms of the affine OP strain e_3. We focus on a special cut in parameter space; we fix the coefficients appearing in (5.3) and γ', and explore the dynamical phase diagram in the plasticity variables, σ_{1c}–h_1 plane (fig. 5.17 (b)). The threshold stress σ_{1c} is expressed in units of $a_1 \Delta \mathbf{e}_1^A$ (the affine stress at the structural transition), and h_1 in units of ℓ^2/γ' (where ℓ, thickness of the twin interface, has been taken to be 1). In fig.5.17 (a), we plot A as a function of time for an anisotropic (twinned) nucleus and an isotropic (untwinned) nucleus; the value of A at late times (fig. 5.17 (a)), and the profile of the order parameter strain is used to map out a dynamical phase diagram containing the martensite and ferrite, fig.5.17 (b).

There are several novel features in the dynamical phase diagram. For instance, even when the threshold stress σ_{1c} is zero, a martensite can form if the plasticity relaxation rate is small (large h_1) compared to the rate of growth of the nucleus. This feature was already present in our earlier calculation [33], where the dynamics of the local density fluctuations determined the selection of microstructure, and is an inescapable feature of real martensites. The phase diagram, fig.5.17 (b), is constructed for a fixed value of under-cooling. As the degree of under-cooling changes, the phase boundary changes slightly, but not a whole lot- the ferrite is favoured for low under-cooling. More significantly, the plasticity relaxation time h_1 increases with the lowering of temperature. Thus by starting out in the ferrite phase, one can cross the phase boundary into the martensite by simply

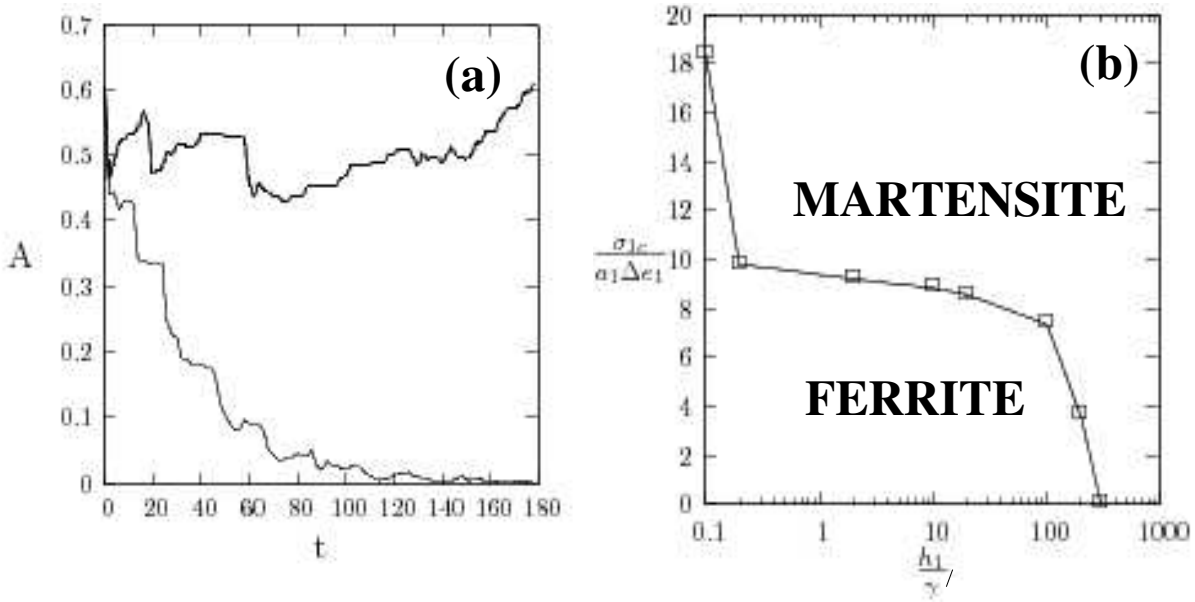

Figure 5.17: Results from the numerical solution of the dynamical equations in a 128×128 grid with a time step $\delta t = 0.002$. The parameters for this calculation are $a_1 = 100, a_2 = 1, a_3 = 0.01, \gamma' = 5$. (a) Shape asphericity A of the growing nucleus as a function of time t from the elastoplastic model – bold line martensite and thin line ferrite. (b) Dynamical phase diagram in the $\sigma_{1c} - h_1$ plane (expressed in units of $a_1 \Delta \mathbf{e}_1^A$ and γ', respectively), starting from the same (elliptical) initial seed. The shape asphericity A at later times and the order parameter strain e_3 have been used to determine the phases.

lowering the temperature, identified as the martensite-start or T_{MS} temperature. In addition, there is a well defined plateau yield stress over three decades in h_1, suggesting that the yield stress is independent of temperature over this range. This is consistent with our simulations results. Finally, it must be noted that the dynamical phase diagram, fig. 5.17 (b) is constructed from the nature of the first critical nucleus that forms. In a macroscopic sample, a ferrite nucleus may eventually nucleate and grow *even in the martensite phase*, once the plastic strain e_1^P gets enough time to relax. This is consistent with our simulations and agrees with results of isothermal quenching experiments in real materials [80].

Having displayed the dynamical phase diagram we perform quenches to the martensite and ferrite phase, and study the time development of the profiles of e_3, σ_1 and e_1^P (figs. 5.18, 5.20).

Using plasticity parameters corresponding to the martensite phase, (fig. 5.18) shows the temporal evolution of a twinned nucleus, in perfect analogy with our simulations. The nucleus initially grows parallel to the twin boundary (fig. 5.18 (i)), while the stress σ_1 approaches the threshold at the growing tips. As a result the plastic strain e_1^P gets to be large at these tips. As the nucleus grows, these highly stressed and plastic regions are advected by the growing tips. In the interior transformed region, the stress relaxes to a sub-threshold value, and the plastic deformation goes to zero. The sequence of events exactly mimic the dynamics of the $\mathbf{e}_V^A$, χ and NAZs of fig. 5.5 [85].

To study the time evolution of the NAZs in more detail, we focus on a single cell, Ω, midway within our computation box, along (but not on) the twin boundary of the initial seed within the untransformed square lattice. With time, the growing tip of the nucleus approaches, and then sweeps by Ω, in the process transforming it into the triangular phase. This situation is analogous to that shown in fig. 5.12 from our simulations results. We plot the local e_1,σ_1 and e_1^P at Ω as a function of time t in fig. 5.19. As in fig. 5.12, initially Ω, which lies ahead of the approaching transformation front, begins to deform elastically due to stress generated at the growing tip. The resulting affine volumetric strain e_1^A is proportional to the local σ_1 and $e_1^P = 0$. As the tip of the growing nucleus approaches Ω, σ_1 rises and tends to cross the threshold, σ_{1c}. At this instant, e_1^P begins to form reducing σ_1 to a value below σ_{1c}. As the nucleus grows further, σ_1 within Ω in-

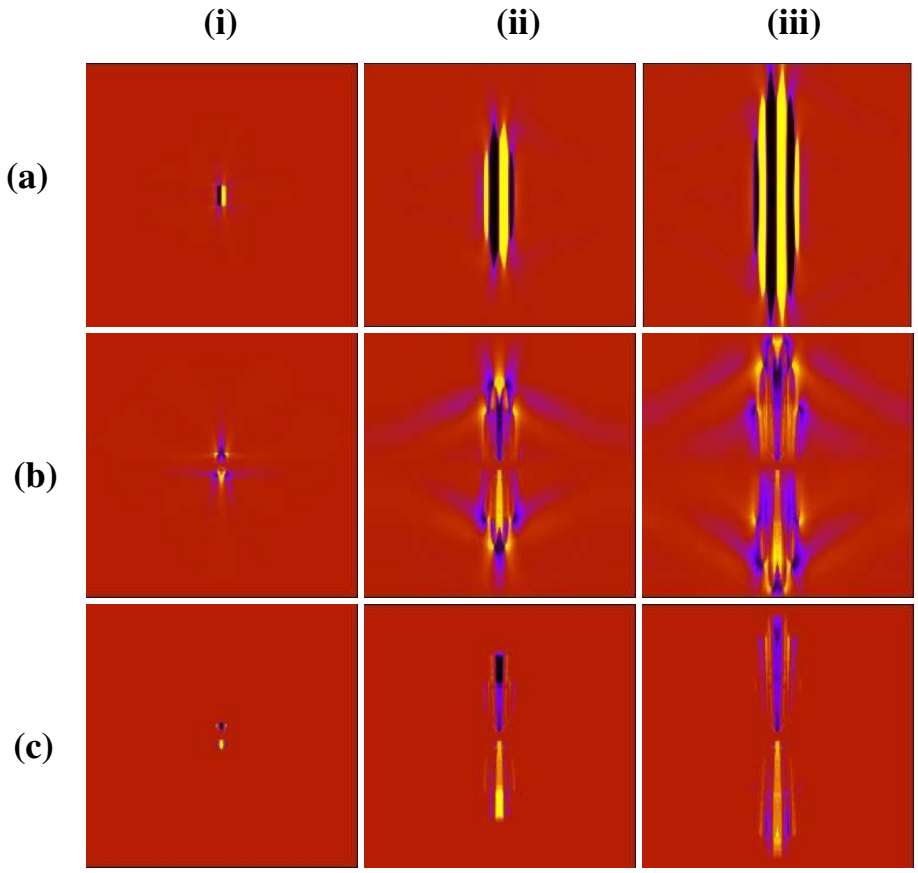

Figure 5.18: Time development of the affine strain, stress and non-affine strain following a quench into the martensite phase for 512×512 cells, at (i) $t = 30$, (ii) $t = 600$ and (iii) $t = 800$, starting from an initial elliptical nucleus with a single twin boundary. The plasticity parameters $|\sigma_{1c}| = 1$ and $h_1 = 1$ while the rest of the parameters are as before. (a) Profile of affine OP strain e_3, showing the initial growth parallel to the twin interface, followed by the dynamical addition of twins. Colors: yellow to black maps the range $-1.0 < e_3 < 1.0$. Brown region denotes retained austenite, $e_3 = 0$. (b) Corresponding profile of the local stress σ_1. The local stress is concentrated at the tips of the growing front where it approaches the threshold value σ_{1c} (i) and (ii). In the interior of the growing nucleus σ_1 relaxes to zero. Subsequently in (iii), the local stress gets large in regions where the new twins are being accommodated. Note the variation in the signs of the stress in the direction along which new twins are added. Colors: yellow to black maps the range $-1.0 < \sigma_1 < 1.0$. (c) Corresponding non-affine strain e_1^P, showing the initial advection by the transformation front, and its dynamical emergence as subsequent twins are added. e_1^P appears in regions where $\sigma_1 \sim \sigma_{1c}$ and $\sigma_1 \sim -\sigma_{1c}$. Colors: yellow to black maps the range $-0.01 < e_1^P < 0.01$.

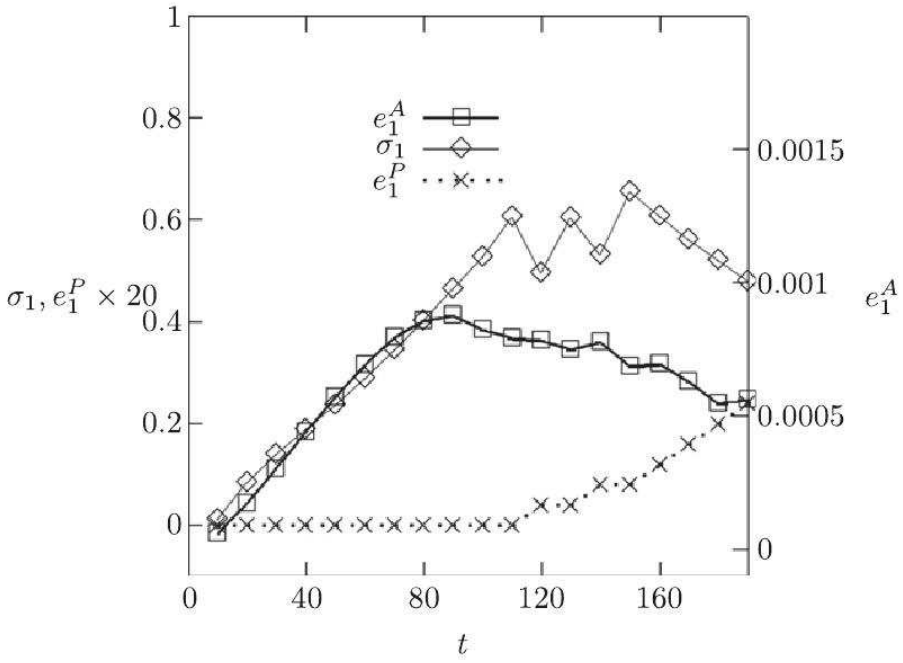

Figure 5.19: Evolution of the local affine strain e_1^A (scale on right), the local stress σ_1 and the non-affine part of the strain e_1^P for a cell $\Omega = (128, 100)$ on the twin axis following the quench into the martensite phase shown in fig.5.18. Note the initial linear regime, when $\sigma_1 \propto e_1^A$ and $e_1^P = 0$, followed by oscillations in σ_1 and the creation of e_1^P as the stress σ_1 rises to the threshold value $\sigma_{1c} = 1$. The resemblance with fig. 5.12 from our molecular dynamics simulations (Ref. [85]) is quite apparent. We have multiplied e_1^P by 20 in order to make it visible.

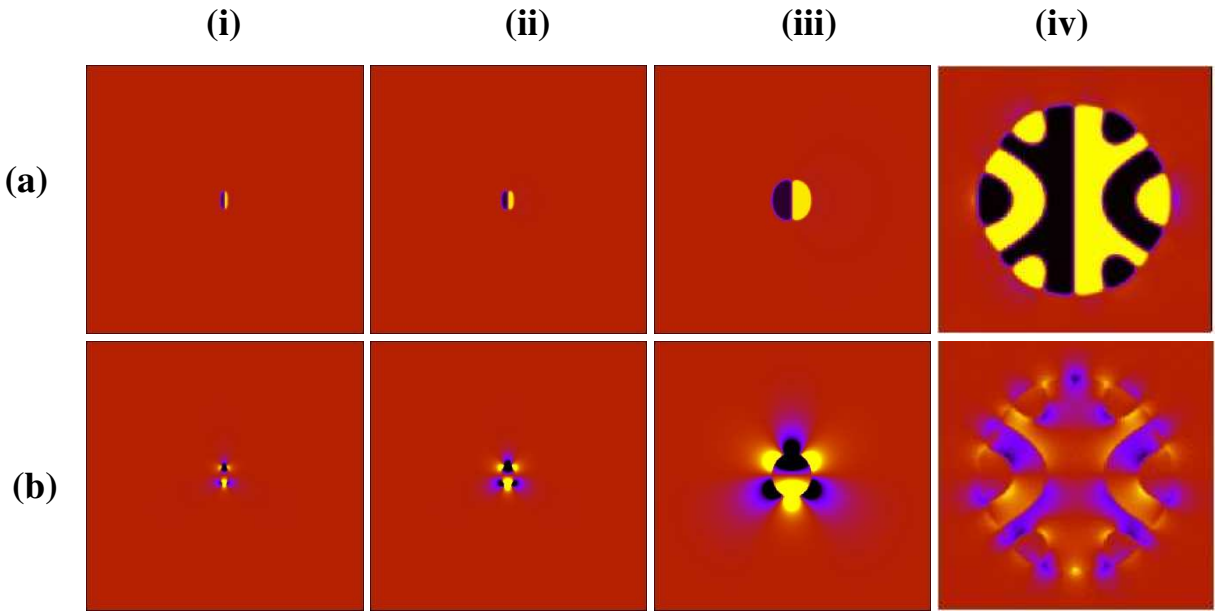

Figure 5.20: Time development of the affine strain and non-affine strain following a quench into the ferrite phase, at (i) $t = 40$, (ii) $t = 200$ and (iii) $t = 1000$, starting from an initial elliptical nucleus with a single twin boundary. The plasticity parameters $\sigma_{1c} = 10^{-4}$ and $h_1 = 1.0$ while $a_3 = 0.1$; the rest of the parameters are as before. (a) Profile of affine OP strain e_3, which shows the initial elliptical nucleus growing approximately isotropically. Colors: yellow to black maps the range $-1.0 < e_3 < 1.0$. (b) Corresponding non-affine strain e_1^P, showing its invasion into the 'bulk' of the growing polycrystalline nucleus. Colors: yellow to black maps the range $-0.01 < e_1^P < 0.01$. (iv) (a) and (b) show e_3 and e_1^P respectively for a very late time ($t = 1600$) ferrite nucleus in a 256×256 system with parameters $a_3 = 0.01$, $h_1 = 0.1$ and $\sigma_{1c} = 0$. The stress σ_1 is negligibly small for all (i)-(iv).

creases again – and the process repeats producing a local stress which oscillates rapidly in time. These oscillations result from cooperative jamming and unjamming events caused by alternating build-up of σ_1 due to interface motion and its relaxation by creation of NAZs [87]. The region of high (and oscillating) local stress and the NAZ travels with the growing tip, being advected by the moving transformation front. The strong resemblance between fig. 5.12 and fig. 5.19 is striking. Eventually, the interface crosses Ω and σ_1, as well as e_1^P relaxes to zero within the bulk of the product phase.

The subsequent dynamics, fig. 5.18(iii), goes beyond the time scales accessed in the molecular dynamics simulation. The dynamics now proceeds perpendicular to the twin interface, adding new twins (symmetrically disposed) as time proceeds. The production of new twins with a fixed width, is a consequence of the anisotropic, non-local interactions connecting spatially separated regions with nonzero e_3.

Note that the affine NOP strain mediates the anisotropic, long-ranged interactions [22, 23, 24]; the presence of the plastic NOP strain *screens* this interaction, making it short-range. The emergence of the OP strain in the form of twins, leads to an increase in the local stress σ_1, which in turn generates plastic flow on crossing the threshold (fig. 5.18 (c)). The plastic strain, once produced, reduces the value of the total NOP strain and, therefore, that of the non-local interaction. In the case of the martensite, this reduction is not complete. The stress σ_1 decreases to zero in the interior of the martensitic nucleus, so that any given region undergoes the same sequence of transformations : untransformed $\rightarrow$ elastic distortion $\rightarrow$ non-affine $\rightarrow$ transformed. This temporal sequence is also seen in our simulations.

We now use plasticity parameters corresponding to the ferrite phase. Fig. 5.20 depicts the time evolution of an isotropic, polycrystalline ferrite nucleus, starting from the same initial conditions. For small values of σ_{1c}, the plastic strain e_1^P is produced readily, and on average largely cancels out the effect of the affine NOP strain. This significantly reduces the magnitude and range of the non-local interactions, which were responsible for producing the twins. The local stress σ_1 tends to cross the threshold (positive and negative) in the *interior* of the growing nucleus, which leads to an *invasion* of the non-affine strain e_1^P into the 'bulk' of the isotropically growing, polycrystalline nucleus. This results in incoherent grain boundaries in the interior of the growing nucleus. Note that the symmetry

of the pattern in fig. 5.20 which arises because the evolution equations are deterministic; any noise would destroy this symmetry and make the grain boundaries rough and orient randomly. The sequence of events then exactly mimic the dynamics of the $\mathbf{e}_V^A$, χ and NAZs of fig. 5.7.

Thus we have successfully constructed the elastoplastic theory which gives a general description for the dynamics of microstructure selection and formation in solid state transformations. The results of the theory closely resembles to that obtained from the molecular dynamics simulations.

5.6 Appendix C

The numerical steps used for the iteration of the dynamical equations of the elastoplastic theory are as follows:

- *Step 1-* We start with initial values for e_3, its time derivative $\dot{e}_3$ and e_1^P defined over all the cells in our lattice and for time t. First, we need to compute the (slaved) affine strain $\mathbf{e}_1^A$ from the OP strain e_3 by solving (eqn. 5.6). The affine strain e_1^A together with the known e_1^P determines the total strain e_1 at t. In real space, (eqn. 5.6) becomes,

$$\nabla^2 e_1(x,y) = q_{13}\frac{\partial^2}{\partial x \partial y} e_3(x,y) \tag{5.10}$$

  Equation 5.10 is the Poisson equation for the charge density,

$$\rho_3(x,y,\{e_3\}) = q_{13}\frac{\partial^2}{\partial x \partial y} e_3(x,y) \tag{5.11}$$

  and we need to solve it for the (Dirichlet) boundary condition $e_1 \to 0$ for $x, y \to \infty$. This is done by discretization in real space and by using an iterative scheme with a small over-relaxation and a convergence criterion of 1 in 10^6 [92, 68]. For convenience in what follows, we refer to this solution using the notation, $e_1 = \mathcal{P}(\{\rho_3\})$.

  Our numerics can be checked for accuracy by comparing the results with that of simple choices for e_3 for which e_1^A (same as e_1) may be obtained analytically.

- *Step 2-* Knowing the strain e_1 at time t, we next update the plastic strain e_1^P to the next time step $t + \delta t$ by iterating eqn. 5.9. For this, the local stress $\sigma_1 = a_1 e_1$ (plus any external stress if present) is obtained for all the cells and is then used as input to eqn. 5.9.

- *Step 3-* Lastly, we have to update e_3 and $\dot{e}_3$ for which one needs to compute the functional derivative,

$$\frac{\delta \mathcal{F}}{\delta e_3} = \frac{\delta \mathcal{F}_3}{\delta e_3} + \frac{\delta \mathcal{F}_1}{\delta e_3} \tag{5.12}$$

where the two terms on the right hand side represent functional derivatives of the parts of the free energy (eqn. 5.3) involving only e_3 and e_1 respectively. The first term is straightforward and is given by,

$$\frac{\delta \mathcal{F}_3}{\delta e_3} = -\nabla^2 e_3 + e_3 - 4(e_3)^3 + 6(e_3)^5 \,, \tag{5.13}$$

while the second term, after some algebra, can be shown to be,

$$\frac{\delta \mathcal{F}_1}{\delta e_3} = a_1 \mathcal{P}(\{\rho_1\}) - c_1 \rho_1 \tag{5.14}$$

where,

$$\rho_1(x, y, \{e_3\}) = q_{13} \frac{\partial^2}{\partial x \partial y} e_1(x, y) \,. \tag{5.15}$$

Note that eqn. 5.15 involves the total e_1 which includes both affine as well as the non-affine strain. Even if $e_3 = 0$ to begin with, at subsequent times e_3 may be created due to the presence of nonzero e_1^P. One encounters such a situation during the heterogeneous nucleation of martensite near defect sites [2, 84, 1] with pre-existing e_1^P. Secondly, the resulting form for the functional derivatives are highly non-local since they involve repeated solutions of the Poisson equation. However, if e_1^P is large the total NOP strain e_1 vanishes and the non-local coupling between spatially separated regions of the OP e_3 disappears.

Chapter 6

Microstructure selection as a space-time trajectory transition

6.1 Introduction

We have shown in the previous chapter that (1) a solid when quenched across a structural transition is able to show various kinds of microstructure depending on the temperature of quench and (2) microstructure selection in solids undergoing a structural transition is driven by the dynamics of localized and transient regions within the solid called non-affine zones or NAZs. This information is summarized in a dynamical phase diagram shown in fig. 6.1 (a). Quenches within the shaded region in $v_3 - \alpha - T$ space, bounded by a well defined surface $T_{MS}(v_3, \alpha)$, produce martensitic microstructures while those above $T_{MS}(v_3, \alpha)$ are ferritic. T_{MS} refers to the *martensite start* temperature. The typical NAZs which accompany these quenches are also shown in fig. 6.1 (b) and (c) for completeness. Recall that when the evolution of the NAZs is arrested, twinned martensitic microstructures form with the NAZs being advected by the growing front. When the NAZs disperse throughout the growing nucleus, a ferrite results. In this chapter we explore the multi-scale properties of the NAZs by showing that the two different scenarios result from a *dynamical transition* in the character of the particle trajectories.

Often the parent and product solids are incompatible, with considerable mismatch or frustration at the interface. This mismatch is accomodated in various ways giving rise to different microstructures. Here we show that this accomodation is facilitated by the appearence of dynamical heterogeneities in solids undergoing such structural transition. These heterogeneities are analysed in terms of a thermodynamics of space-time trajecto-

ries of active particles [41, 42]. An order parameter is defined characterizing the nature of trajectories of active particles which show an abrupt transition precisely coinciding with the sharp transition in the microstructure of the product solid, thus defining the thermodynamics of phase transitions in trajectory space. The active particles experience intermittant jamming and flow. Hence the underlying physics of solid-solid transformations share common features with the physics of plasticity [37, 93], glass [41, 94] and granular systems [87, 95, 96].

Starting from the lowest scale, the problem of microstructure selection is how do the particles of the parent solid know how to position themselves with respect to each other, so as to form a product with a specific microstructure and precise relations at the parent-product interface ? We address this using our molecular dynamics (MD) simulations of a model solid-solid transformation. Thus, NAZs accompanying the martensitic nucleus contain particles which move ballistically and in a coordinated manner, while those associated with the ferrite nucleus contain particles that move diffusively, characterized by a local effective temperature. The jamming and unjamming of the local stress at the meso-scale is reflected in the tagged-particle dynamics at the microscale. This qualititative change in tagged-particle dynamics is sharp and coincides with the dynamical transition from an isotropic, untwinned to an anisotropic, twinned critical nucleus thus showing an intriguing connection between microscopic particle trajectories, mesoscopic NAZs and macroscopic structural transformation.

We demonstrate this scenario by calculating several structural and dynamical quantities from our MD simulations, namely the shape of the critical and supercritical nuclei, the first-passage times, equal time strain correlations within the NAZ, the diffusion matrix and the velocity auto-correlation function. All of these diverse quantities exhibit prominent signatures of a dynamical transition — all approximately at the same temperature. In what follows, we first define each of the above quantitites one by one and show how these may be obtained from our MD configurations. This is followed by the presentation and discussion of the results. Finally, we conclude the chapter by exploring the implication of our findings on the observed dynamical transition.

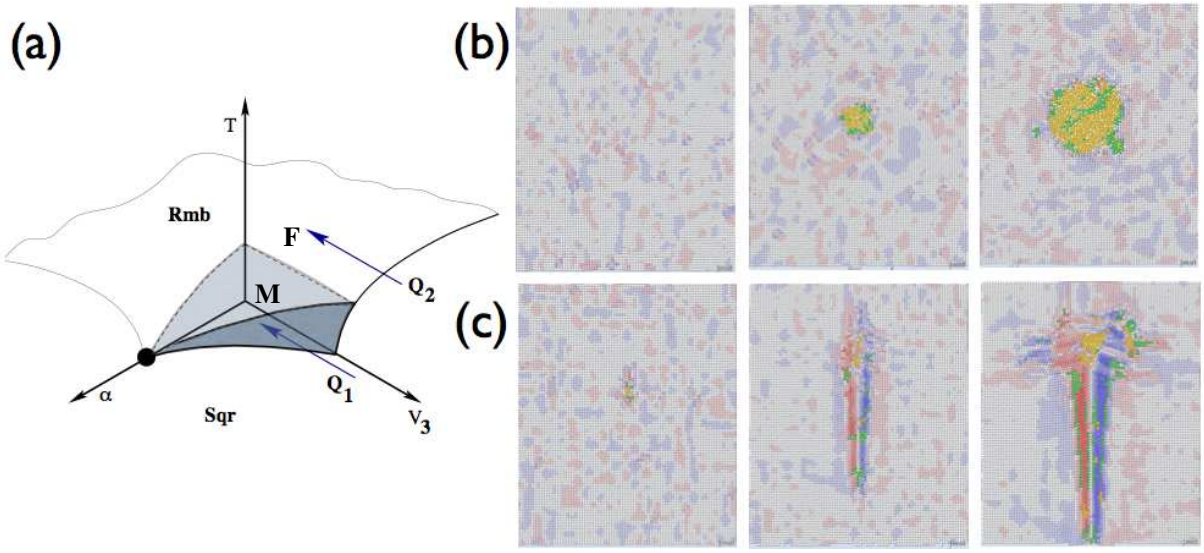

Figure 6.1: (a) Phase diagram in $T - v_3 - \alpha$ at $\langle\rho\rangle = 1.1$, same as figs. 4.9 and 5.1 but now indicating the dynamical transition between ferrite (F - Q_2) and martensite (M - Q_1) across the shaded surface. Time development snapshots showing NAZs for (b) ferrite and (c) martensite. The order parameter shear strain is shown in red ($+ve$) and blue ($-ve$); the high density NAZ is shown in yellow and low density NAZ in green. Untransformed regions are shown in gray. In the ferrite, presence of large non-affine contribution masks the order parameter strain.

6.2 First passage times and shape of the critical nucleus

The mean first passage time (FPT), in the context of the decay of a metastable state, is defined as the average time one has to wait before nuclei of the stable phase begin to appear. At every temperature, there are droplet fluctuations of the product phase within the body of the parent. The energy E_d of these droplets, considered to be d dimensional spheres of radius R within classical nucleation theory, is given by $E_d(R) = -A'R^d + B'R^{d-1}; A', B' > 0$ where the terms represent volume and surface contributions respectively. Fluctuations with size $R < R_c$, where the critical radius $R_c = B'(1-1/d)/A'$, tend to decay while those with $R > R_c$ grow. The FPT is therefore the average time one has to wait before one obtains a random fluctuation of size R_c. At the equilibrium transition temperature T_c, $A' \to 0$ and $R_c \to \infty$ so that the FPT also

diverges. As the temperature is reduced, the FPT is expected to decrease. The brief description given above has been successful in describing simple situations like nucleation of droplets of liquid in a condensing gas or a field driven magnetization reversal in Ising like magnets [97, 98].

In a solid state transformation, the situation is considerably more complex and a corresponding nucleation theory for solid in a solid does not exist. Firstly, the droplet energy may not be expressible as a neat sum of volume and surface terms since contribution from elastic fields partially screened by fluctuations of non-affine fields of the sort discussed in chapter 5 are important. Secondly, the surface energy is now strongly anisotropic and will have the symmetry of the parent lattice. Thirdly, behavior of the FPT is more complex because atomic diffusion, which may be involved in the formation of the new phase, is strongly temperature dependent. Metallurgical engineers, who require to know the formation kinetics of the stable phase in quantitative detail, have empirically obtained this information for a variety of alloys. Recalling the discussion in chapter 1 in section 1.4, this is depicted in the form of a diagram — the so called time - temperature - transformation or TTT curve shown in fig. 1.2. Finally, the shape of the critical nucleus has no reason to be isotropic at all temperatures. All of these effects suggests that a simple classical nucleation theory is grossly inadequate for describing solid state transformations in full detail.

In our MD simulations, we have found the FPT in the following simple way. We have characterized the formation of the rhombic phase using the average order parameter $\Omega = 1/N \sum \Omega_i$, with Ω_i being defined as in chapter 5. A plot of $\Omega(t)$ shows an initial incubation period when $\partial\Omega(t)/\partial t$ is small followed by accelerated growth. We find out the typical duration of this incubation period by fitting a straight line to the data for $\Omega(t)$ at intermediate times (larger than FPT but smaller than the saturation time due to finite size effects) and extrapolating it to $\Omega(t_{in}) = 0$. We identify this incubation time t_{in} with the FPT. In fig. 6.2 we present a typical $\Omega(t)$ vs. t curve which shows the growth of the rhombic phase when the system consisting of $N = 12099$ particles is quenched from $v_3 = 5.0$ to $v_3 = 1.65$ for $\alpha = 0.0$ and at $T = 0.1$. A linear fit to the intermediate time behavior, is extrapolated to obtain an approximate value of the FPT. In fig. 6.3, we have plotted the FPT obtained in this way as a function of the temperature

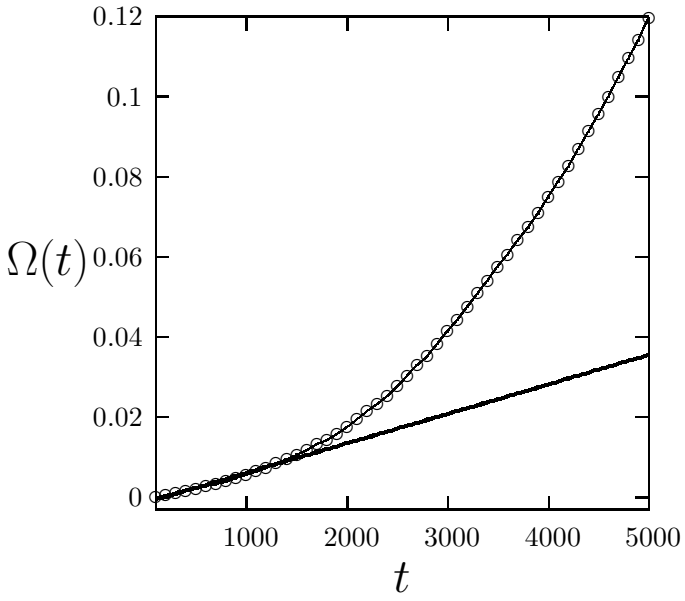

Figure 6.2: Typical Ω vs t curve for a quench from $v_3 = 5 \rightarrow 1.65$ for a system of $N = 12099$ particles at $\rho = 1.1, T = 0.1$ with $\alpha = 0.0$. The curve is obtained after averaging over 23 quenched configurations.

of the quench. The FPT first decreases as a function of temperature. However as the temperature is decreased further, amazingly, the FPT goes through a minimum at around $T \approx 0.2$. At still lower temperature, the FPT increases signifying the lack of diffusion making the transformation to ferrite sluggish. At a temperature below 0.2 martensite begins to form. One therefore finds that the FPT initially decreases for high temperature transformation to a ferrite but then tends to increase as the temperature is reduced. In materials which undergo martensitic transformations, martensites begin to form when the temprature decreases below T_{MS} where diffusion is completely suppressed. The FPT for martensite formation is usually smaller than that of ferrite which needs atomic diffusion. The sequence of events in our model solid, seems to mirror quite faithfully the situation in a real material.

At the same time, we also keep track of clusters of particles with $\Omega_i > 0$ formed at each time step and identify the largest such cluster at t_{in} with the critical nucleus. Once the cluster has been identified, we calculate the eigenvalues $\lambda_>$ and $\lambda_<$ of the moment of inertia tensor $I_{mn} =< n^{-1} \sum_i (\mathbf{r_i} - \mathbf{r_{cm}})^{\mathbf{m}} (\mathbf{r_i} - \mathbf{r_{cm}})^{\mathbf{n}} >$, where $\mathbf{r_{cm}}$ is the centre of mass

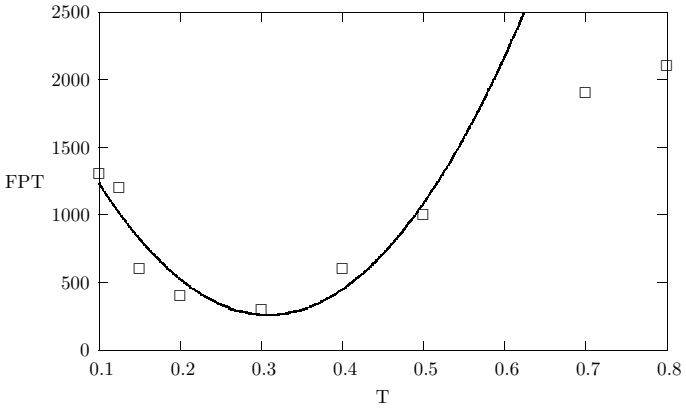

Figure 6.3: FPT in MD steps as obtained from the procedure shown in fig. 6.2 from our MD simulations of $N = 12099$ particles with $\alpha = 0.0, v_3 = 1.65, \rho = 1.1$ and $T = 0.1$.

of the cluster and $\mathbf{r_i}$ is the position vector of the i^{th} particle in the cluster of n particles. The anisotropy of the nucleus is then defined as

$$\mathcal{A} = \frac{\lambda_> - \lambda_<}{\lambda_> + \lambda_<} \tag{6.1}$$

At every temperature we average our results over many independent quenches from different realisations of the initial equilibrium configurations at $v_3 = 5.0$. The formation of a martensitic critical nucleus is signified by a sharp upturn in the $\mathcal{A}$ vs T curve shown in fig. 6.4. The upturn occurs just after the dip in the FPT in a behavior again reminiscent of TTT curves in real systems. Our data for the critical nuclei are, however, plagued by large error bars which tend to mask the transition somewhat. We have therefore plotted the same parameter, in the same plot, for a growing nucleus at later times referring to it as the supercritical nucleus. The transition is now much sharper.

6.3 Equal time strain correlations and "Twinniness"

We have shown in the last section that the critical and super critical nuclei change in shape as the temperature at which the transformation takes place is reduced. There is a signature of a well defined transition characterized by a sharp increase of the anisotropy parameter $\mathcal{A}$ at a temperature below the point of minimum FPT (the so-called "nose") – a behavior reminiscent of the martensitic transition as depicted in the TTT curves

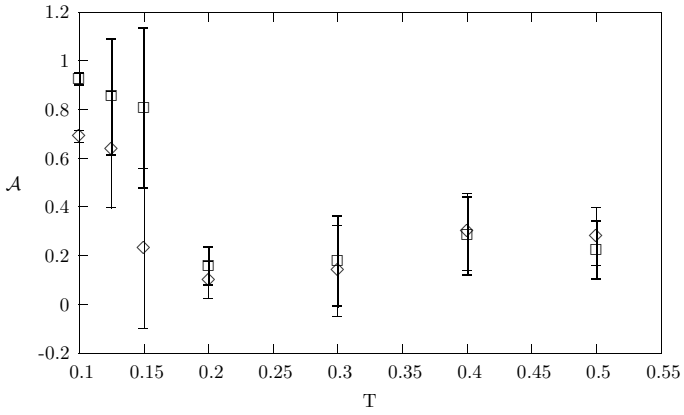

Figure 6.4: Shape anisotropy of the critical nucleus (diamond) and supercritical (box) nucleus - note the higher anisotropy for lower temperatures signifying sharper transition for the supercritical nucleus at $t = 5000$ MD timesteps.

(*ref.* section 1.4). As we have learnt in chapter 5, the highly anisotropic martensite nucleus is also twinned i.e. consist of a pair of grains of the product phase with equal and opposite values of strain lying on either side of an approximately flat grain boundary. We need to show that twins appear at the same temperature at which the nuclei become anisotropic to lend more credence to our contention that microstructure selection in solid state transformation is, in fact, a true dynamical transition.

In order to quantify the formation of twins, we calculate the equal-time strain - strain correlation function defined as,

$$T_{33}(\mathbf{r}, t) = \langle \sum_{i \in \Gamma} e_3(\mathbf{r}_i, t) e_3(\mathbf{r}_i + \mathbf{r}, t) \rangle \tag{6.2}$$

where the angular brackets denote an average over realizations and Γ is the set of all particles belonging to the nucleus determined by a suitable threshold criterion *viz.* $\Omega_i > 0.1$. Even in an ideal crystal far from any transition, this quantity is anisotropic and has a four fold symmetry, x and y axes being equivalent. Formation of a twin breaks this symmetry while randomly oriented product crystals preserve it. This quantity therefore is ideally suited for distinguishing twinned and un-twinned product nuclei. The correlation functions are plotted for temperatures $T = 0.125, 0.19$ and 0.2 in figs. 6.5 (a), (b) and (c) respectively. Note that at higher temperatures T_{33} has a fourfold symmetry while at low temperatures it becomes distinctively bilateral. The transition is very sharp, occurring

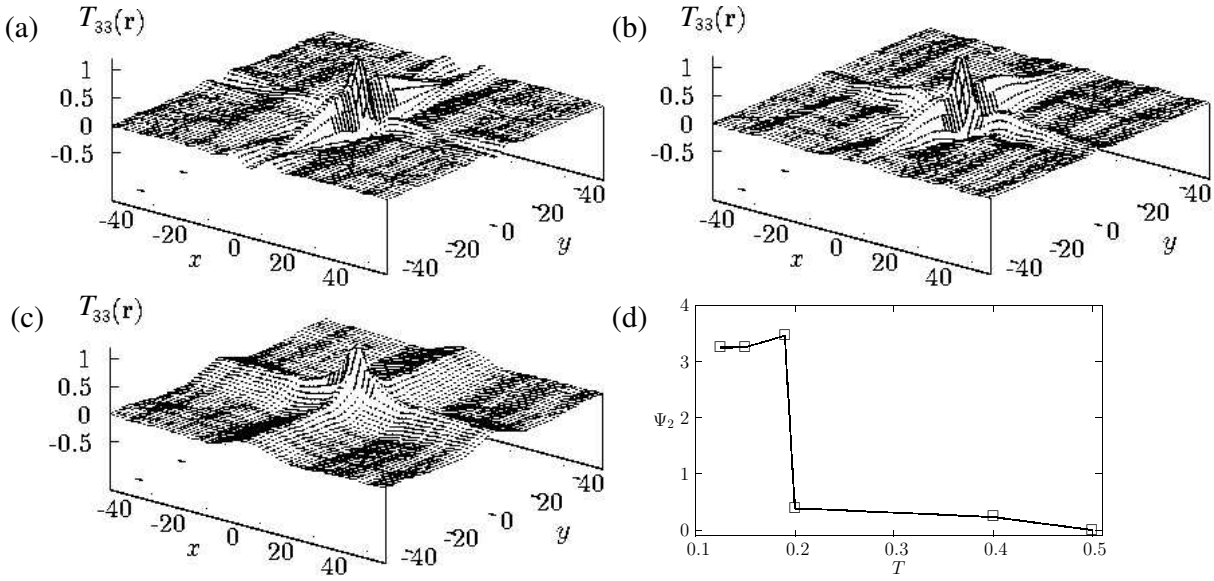

Figure 6.5: Correlation function T_{33} plotted for (a) $T = 0.125$, (b) $T = 0.19$ and (c) $T = 0.2$. (d) The order parameter Ψ_2 is plotted at various temperatures. The dynamical transition occurs at $T = 0.2$. The system consisted of $N = 12099$ particles with $\alpha = 0.0$.

around $T = 0.2$. Using the properties of this correlation function, one can devise an alternative order parameter for the dynamical transition defined as,

$$\Psi_2(t) = \int_0^R dr \int_0^{2\pi} T_{33}(r, \theta; t) \cos(2\theta) \tag{6.3}$$

In fig. 6.5 (d) Ψ_2 is plotted for various values of T. The anisotropy order parameter Ψ_2 changes by two orders of magnitude from 0.007 to 0.7 as T changes from 0.8 to 0.1. In fig. 6.5, the time $t = 5000$ MD timesteps was chosen such that all the nuclei were of comparable size. The correlation functions were averaged over up to 40 realizations after quenching from the square to the rhombic phase using a single vacancy as seed.

In order to investigate whether the nature of the initial state affects the qualitative nature of the correlation functions, the calculation was repeated with a "softer" seed. This is accomplished by using a single special particle in the centre of the box replacing the central particle with a particle whose size σ is smaller than $\sigma_0 = 1$, the size of the rest of the particles, by a factor $\delta = (\sigma_0 - \sigma)/\sigma_0$ (*ref.* section 5.4.2). We have taken $\delta = 0.75$, so as to obtain nucleation events within reasonable computation time. The correlation

function obtained for this system with a soft seed is shown in fig. 6.6. It is clear that there are no qualitative differences.

Therefore from the behaviour of the twin order parameter Ψ_2 and the shape anisotropy

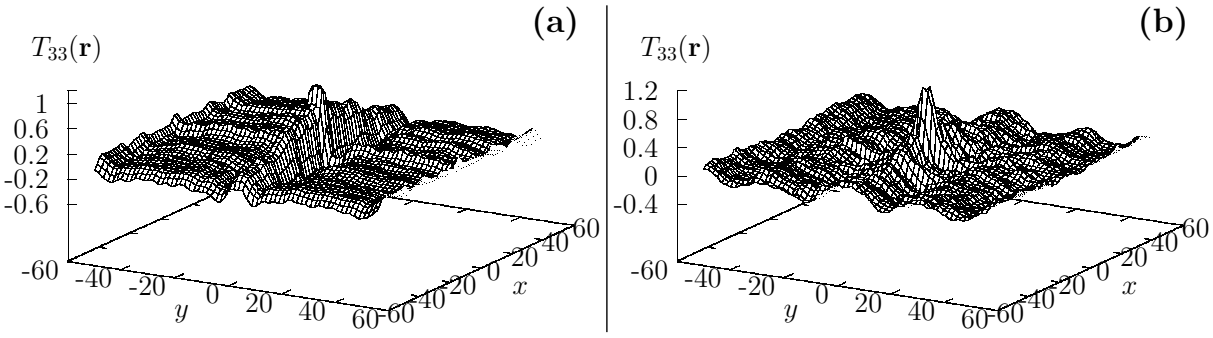

Figure 6.6: Plot of the correlation function T_{33} at (a) $T = 0.1$ and (b) $T = 0.8$ for a system with a soft seed at the centre of a lattice consisting of $N = 12100$ particles with $\alpha = 0.0$

$\mathcal{A}$ of the critical nucleus, we find that the regions F and M are seperated by a sharp dynamical phase boundary (fig. 6.1 (a)). Both Ψ_2 and $\mathcal{A}$ exihibit discontinuous jumps at the dynamical phase boundary. We emphasize that this boundary is sharp only when the quench rate is infinitely fast.

6.4 The velocity autocorrelation function

In this section we show that the dynamical transition signified by the appearance of anisotropic twinned nucleus is driven by an underlying dynamical transition in the nature of the particle trajectories. We shall show this by computing quatities which are related to particle trajectories.

The nucleation and growth of the product is initiated by the movement of a fraction of particles in the neighbourhood of the product nucleus. These are termed as the "active" particles. The clusters formed by such particles define the dynamical heterogeneities in the transforming solid. These dynamical heterogeneities overlap completely with the NAZs characterized by the non-affine parameter χ in chapter 5 [85]. We compute the velocity

autocorrelation function (VACF) for the active particles defined as,

$$\Sigma_{vv}(t,\tau) = \langle \mathbf{v}(t) \cdot \mathbf{v}(t+\tau) \rangle \tag{6.4}$$

The angular brackets denotes an average over all particles and over independent runs. There are two differences with the VACF for ordinary liquids. Firstly, it includes only those particles which belong to the growing nucleus. Secondly, there is no average over t, the origin of time, since the VACF is expected to show aging i.e. variation with respect to a shift of the time origin. This is because unlike the equilibrium VACF, this non-equilibrium VACF is not time translational invariant. We show in fig. 6.7 (a) and (b), the normalized VACF as computed for two temperatures $T = 0.1$ and $T = 0.8$ respectively.

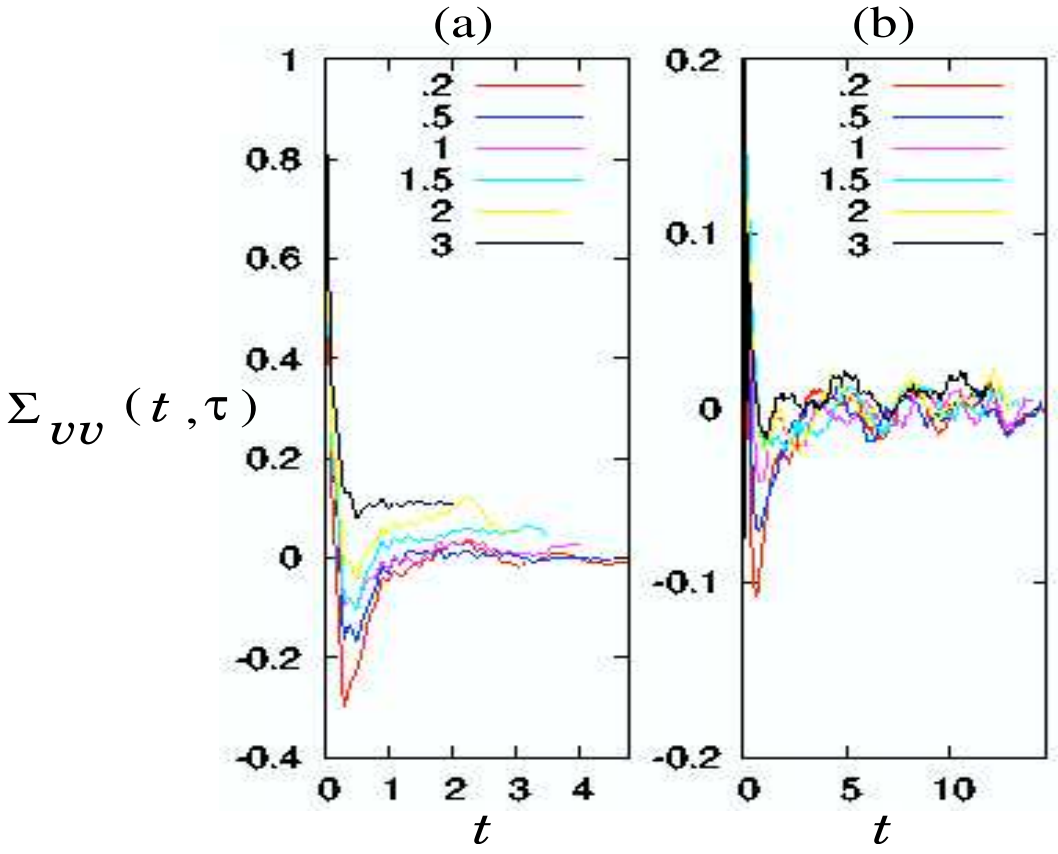

Figure 6.7: Normalized velocity autocorrelation function $\Sigma_{vv}(t,\tau)$ computed for two temperatures, (a) $T = 0.1$ and (b) $T = 0.8$. Here $\tau = 0.2 - 3.0$. The VACF for the martensite at $T = 0.1$ shows strong aging behaviour.

The VACF at $T = 0.1$ for the martensite shows strong correlations and saturates to a non-zerovalue at late times. This indicates that on an average the active particles move ballistically and velocity vectors of individual particles align. Also the VACf shows strong aging behaviour for the martensite.

The velocity correlation time measured from the VACF is defined as follows,

$$\tau_v = \frac{\int_0^{t_{obs}} \sum_i \langle \mathbf{v}_i(t) \cdot \mathbf{v}_i(0) \rangle}{\int_0^{t_{obs}} \sum_i \langle |\mathbf{v}_i(t)|^2 \rangle} \tag{6.5}$$

τ_v is large in case of martensite and much smaller in the ferrite. At times longer than τ_v, the active particles in the ferrite are diffusive, the tagged-particle diffusion coefficient D_0 is large and athermal. It is driven by local variations in free-volume as a result of accomodation with $D_0 \sim \exp(-1/\chi)$, where χ is the non-affine parameter. The tagged particle "diffusion" obtained for $T = 0.2 \rightarrow 0.6$ is shown in fig. 6.8. We plot $\langle \delta r^2 \rangle = \int_0^t \sum_i (\mathbf{r}_i(t') - \mathbf{r}_i(t' - \Delta t'))^2 dt'$ vs. t with $\Delta = 0.1$. The sum is over all active particles. The effective diffusion coefficient D_0 is the slope of the curve. Note that the temperature dependence of D_0 is very weak.

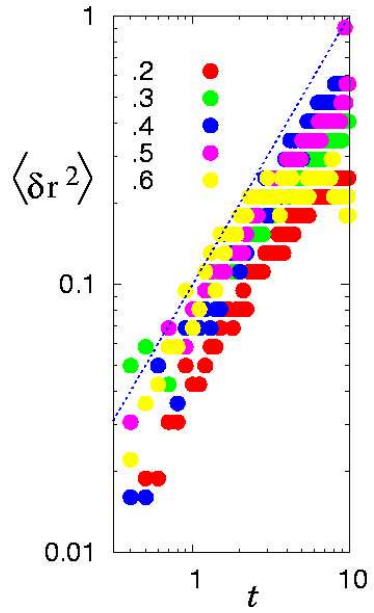

Figure 6.8: The tagged particle diffusion D_0 obtained for $T = 0.2 \rightarrow 0.6$ as the slope of the curve from a plot of $\langle \delta r^2 \rangle$ versus t. D_0 shows a weak temperature dependence.

6.5 Activity and active, inactive transition

A closer look at the space-time trajectories within and in the vicinity of the dynamical heterogeneities, in the form of *kymographs* (figs. 6.9 and 6.10) reveals fine differences between the martensite and ferrite microstructures respectively. In fig. 6.9, we see that

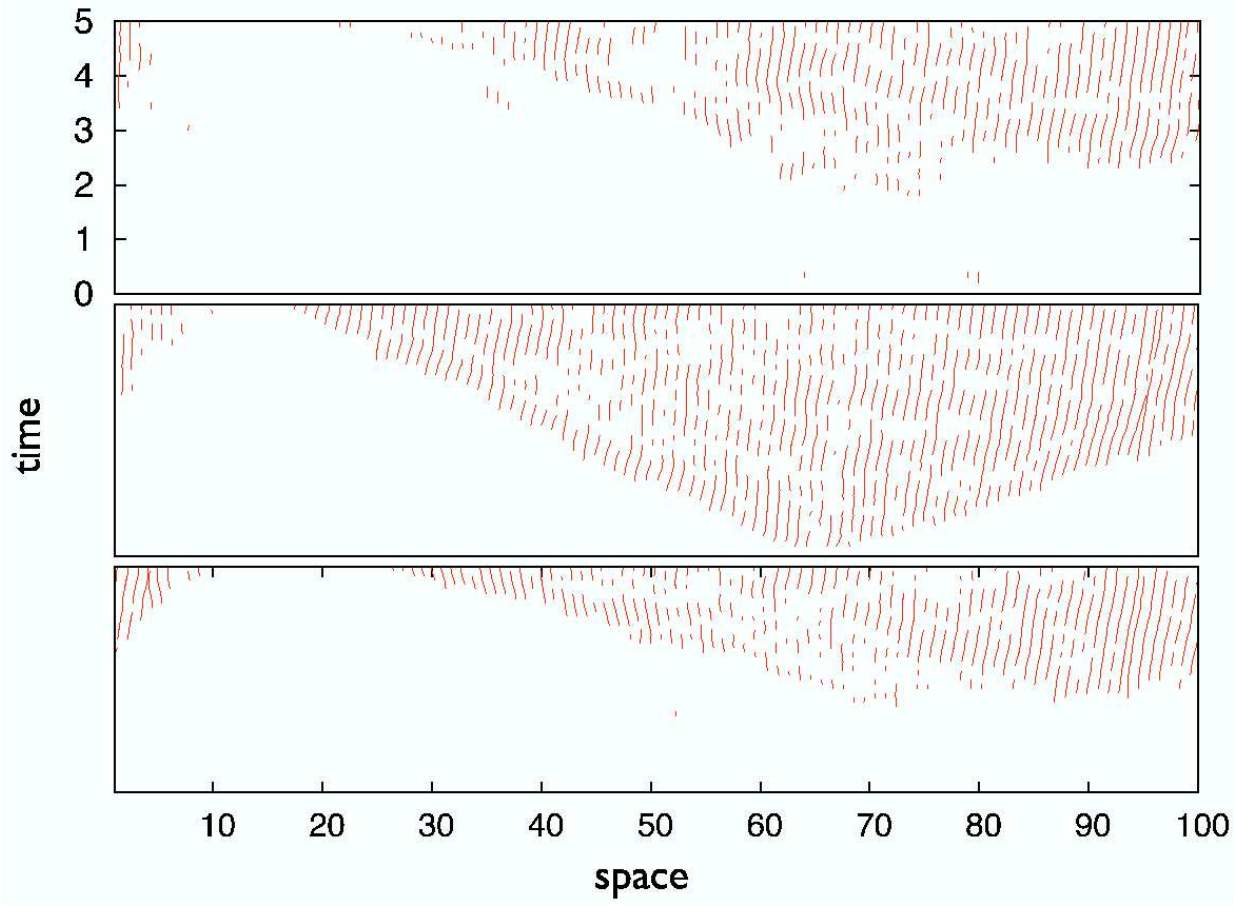

Figure 6.9: Space-time *kymographs* or plots of $y(t)$ for active particles with chosen values of x for the martensite microstructure at $T = 0.1$. The three different plots from top to bottom are for three different values of x used: 10, 15 and 20.

nucleation is accompanied by the birth of a small fraction of active particles which are surrounded by regions of inactive particles [42]. At these early times they move ballistically and in a coordinated manner. The velocity correlation is significant both along a single trajectory and across neighbouring trajectories at equal time. The number of active par-

ticles grows with time, with the older active particles seeding newer ones. Thus the active and inactive particles transform into one another. Significantly, the active particles do not move for too long and their motion is intermittent. The highly coordinated military movement is apparent in the kymograph in fig. 6.9. In ferrite, (fig. 6.10), the fraction

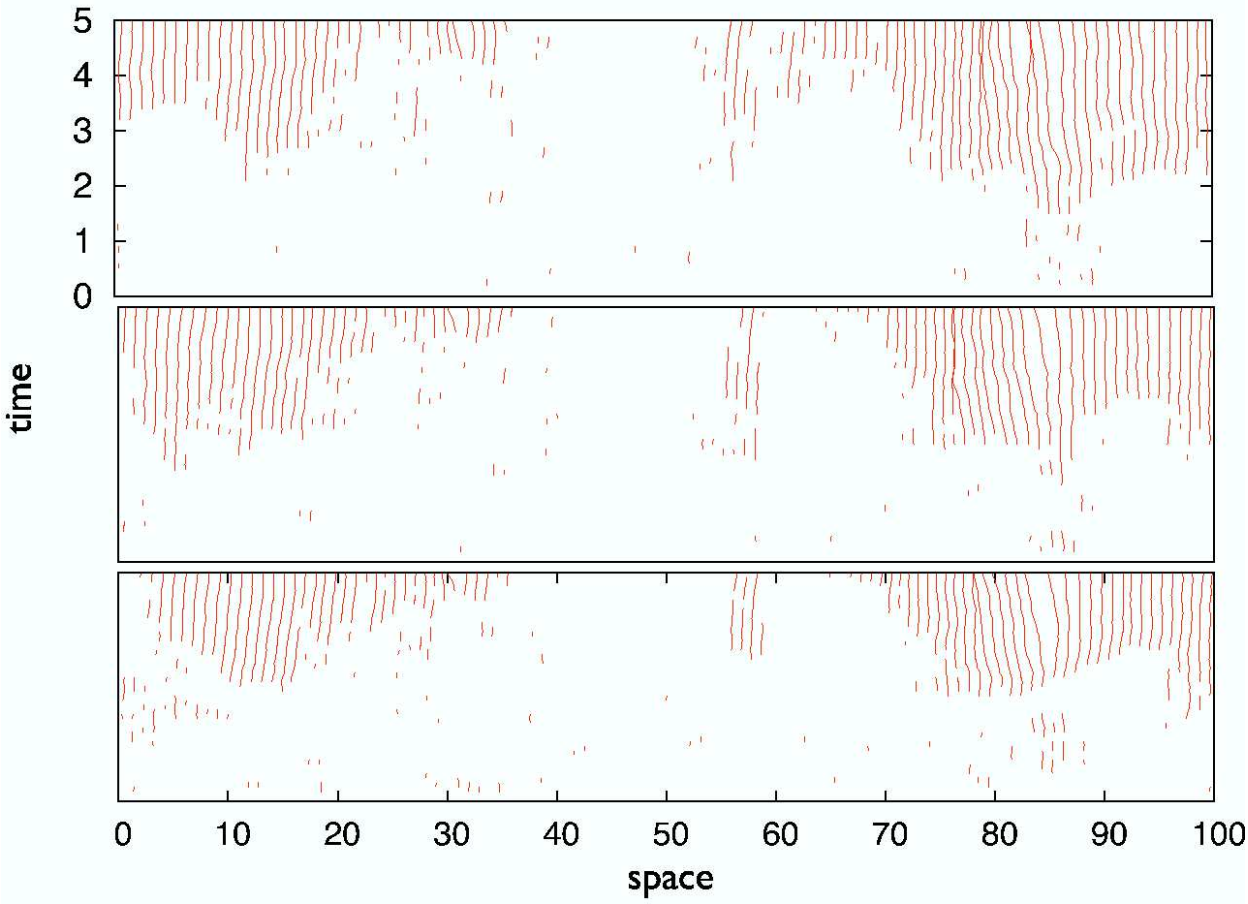

Figure 6.10: Space-time *kymographs* for active particles with chosen values of x for the ferrite microstructure at $T = 0.6$. The three different plots from top to bottom are for three different values of x used: 15, 26 and 57.

of active particles is much larger and their trajectories intersect many times (fig. 6.11 (a)). The single particle trajectories are diffusive over time scales larger than τ_v. For the martensite, active particles are concentrated near the edge of the single growing nucleus, while for the ferrite they are distributed throughout the sample. Note the alternate cycles

of activity showing jamming (inactive) → unjamming (active) transitions. While the particles are active, the trajectories are ballistic in case of the martensite and random for the ferrite. Fig. 6.11 (a) shows that the trajectories of the particles in the ferrite are disordered and entangled with each other. However, for the martensite (fig. 6.11 (b)), they are ballistic and move along specific channels. The active particle trajectories show alternate

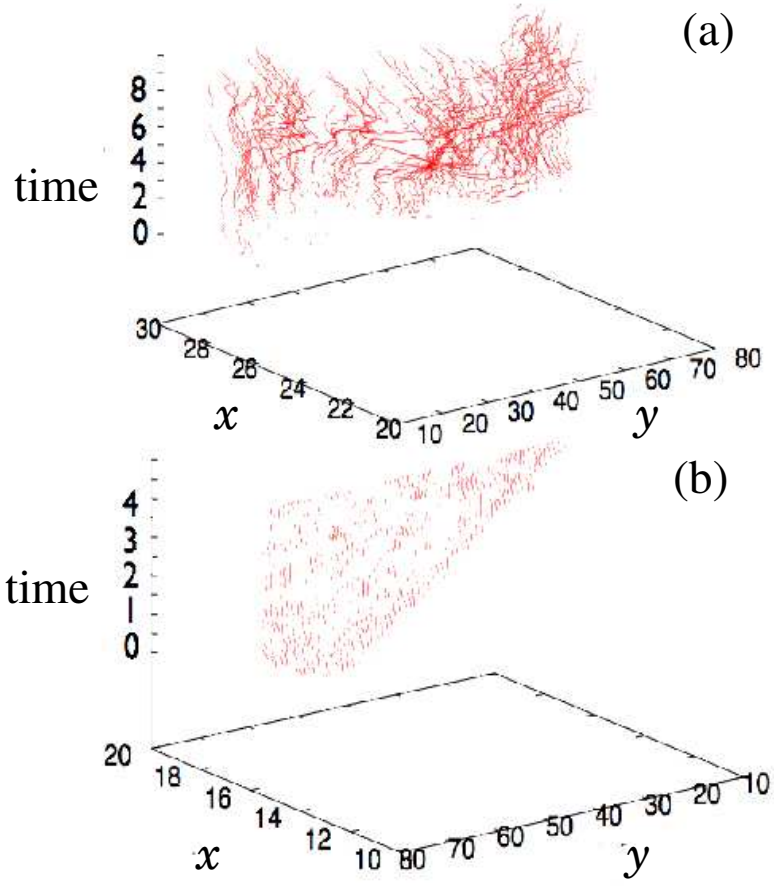

Figure 6.11: Space-time trajectory plots of active particles belonging to a specific crystalline row at $t = 0$ for (a) ferrite and (b) martensite.

arrest and movement in both types of microstructure. They continuously transform from an active to inactive state. We study the statistics of the coordinated active - inactive or unjamming and jamming transitions in the two microstructures using the probability distribution for activity reversal $P(n_R)$. It denotes the number of times particles change

state from active to inactive and vice-versa. Fig. 6.12 shows that the distribution of state reversals is exponential with a possible stretching in case of the ferrite. The arrest of all active particles within a dynamical heterogeneity happens roughly simultaneously (figs. 6.9 and 6.10). This is the space-time realization of the observed jamming and flow [93] in the stress-flow curves within the NAZs.

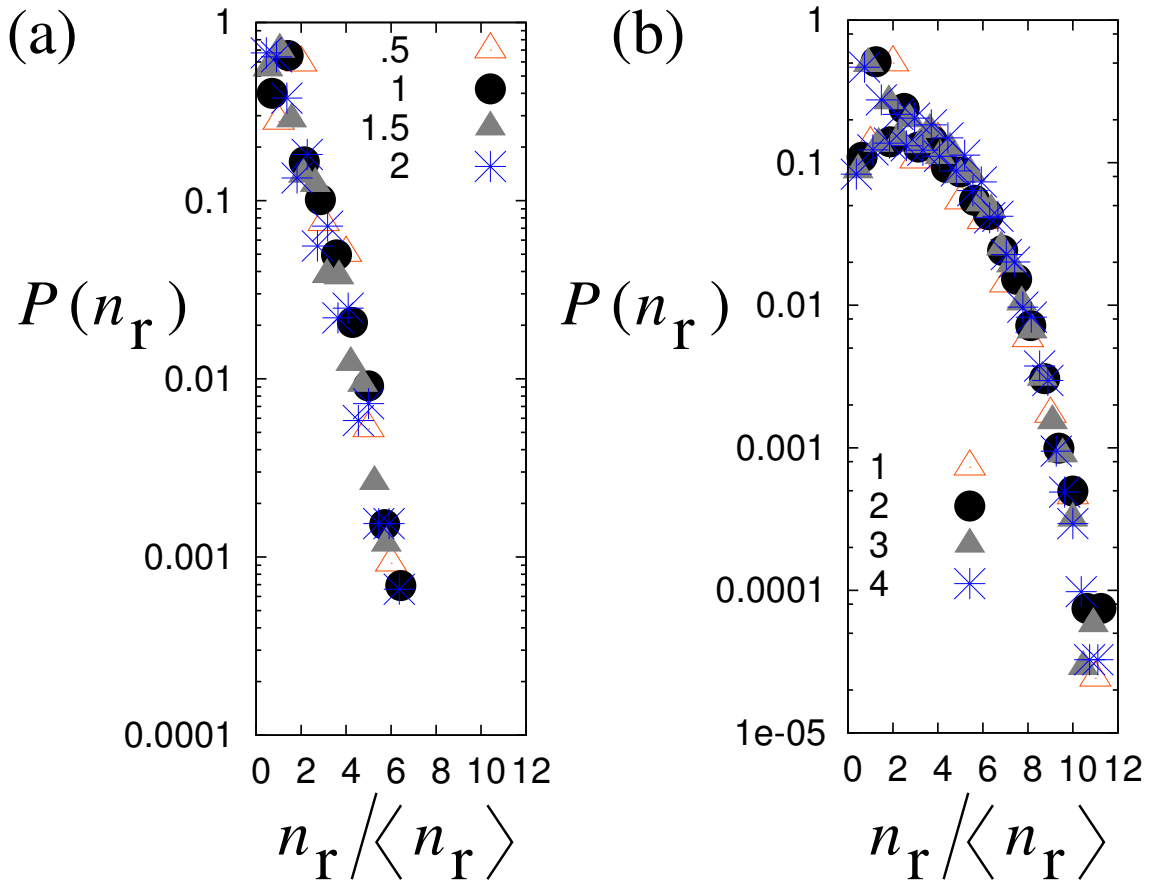

Figure 6.12: Jamming-unjamming transitions shown with the help of the probability distribution for activity reversal $P(n_R)$ for the (a) martensite at $T = 0.1$ and (b) ferrite at $T = 0.6$. (a) is plotted for observation times $t_{obs} = 0.5 - 2.0$ while (b) is plotted for $t_{obs} = 1.0 - 4.0$. In both cases $P(n_R)$ decays exponentially as expected.

6.6 The trajectory transition and dynamical order parameter

We now investigate why the nature of trajectories of the active particles in the dynamical heterogeneities is different in martensite and ferrite. The active particles associated with the martensite are dynamically hindered and do not explore the local configuration space. This is dramatically apparent in the topography of the local energy landscape set by the inactive particles (fig. 6.13 (a)). The energy landscape is obtained by using the fitted local order parameter strain $e_3(x, y)$ in a free energy functional of the form $c_1 e_3^2 - c_2 e_3^4 + c_3 e_3^6$ such that the coefficients c_1, c_2 and c_3 are the nonlinear elastic moduli (upto an arbitrary proportionality constant) obtained from total energy calculations [34]. Fig. 6.13 (a) shows deep ridges in the local free-energy landscape which herd active particles along a narrow channel, creating string-like excitations [94]. The width of the string is of the order of the lateral scale of the dynamical heterogeneities, $\Xi_\perp$. In ferrite, fig. 6.13 (b), the landscape exhibits many criss-crossing shallow ridges which directs particles here and there, ending up in a large scale topography akin to a delta. The shallow delta spans out isotropically, leading to diffusive collective excitations. Thus the difference in the space time trajectories arises from the kinetic constraints on active particles created by the potential landscape due to inactive particles.

To quantify the abrupt changes in the nature of trajectories of (a few) active particles moving in the confining potential created by the (majority) inactive particles, we take a space-time approach [41, 42] and define a thermodynamics of phase transitions in trajectory space. The two types of microstructures are characterized by the space-time intensive off-diagonal order parameter, constructed from the bilinear $\Delta^i_{mn}(t) = u_{im}(t)u_{in}(t)$ with $m \neq n$,

$$\mathcal{O}/N \equiv \frac{1}{t_{obs}N} \int_0^{t_{obs}} dt \sum_i |\Delta^i_{mn}(t)|^2 \tag{6.6}$$

Here we define the Lagrangian displacements $u_{im}(t) = r_{im}(t) - r_{im}(t - \delta t)$, where $m = 1, 2$ (along x and y directions for the square-to-rhombus transition) and δt is a small time offset. The active particles move freely in the confining potential set by the inactive particles. The typical value of $\mathcal{O}/N$ is zero for the martensite and undergoes a sharp jump of $O(1)$ in the ferrite (fig. 6.14 (a) and (b)).

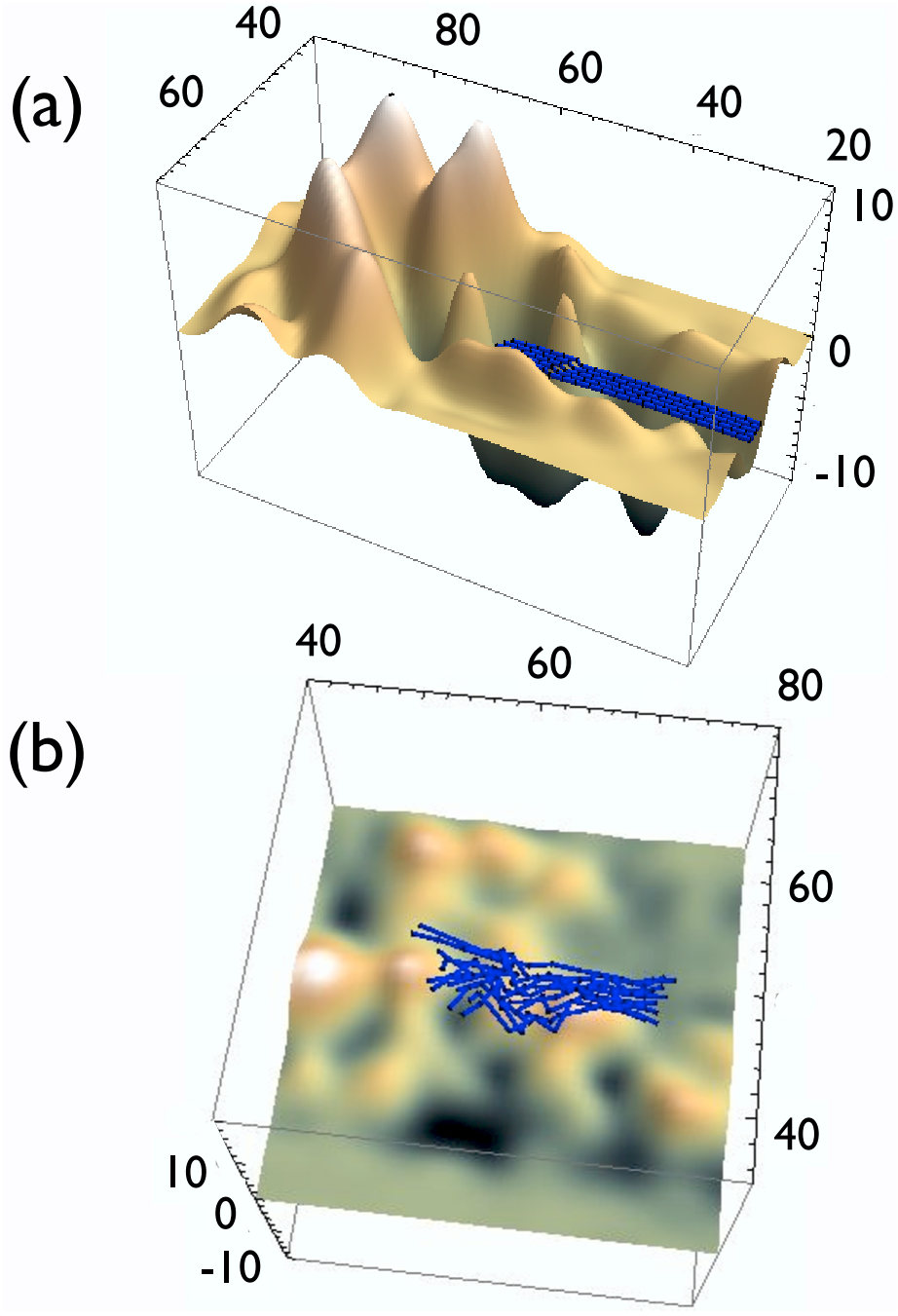

Figure 6.13: Topography of energy landscape obtained during the dynamical transitions for (a) martensite and (b) ferrite microstructures. It shows the regions visited by the tagged particle trajectories during the transition. The nature of the particle trajectoties are distinctly different for the two cases. In (a) the deep ridge directs rows of particles (blue lines) along a specific channel. In (b), the particle excitations span out isotropically and are seen to meander. Thus the collective excitations are string-like in (a) and diffusive in (b).

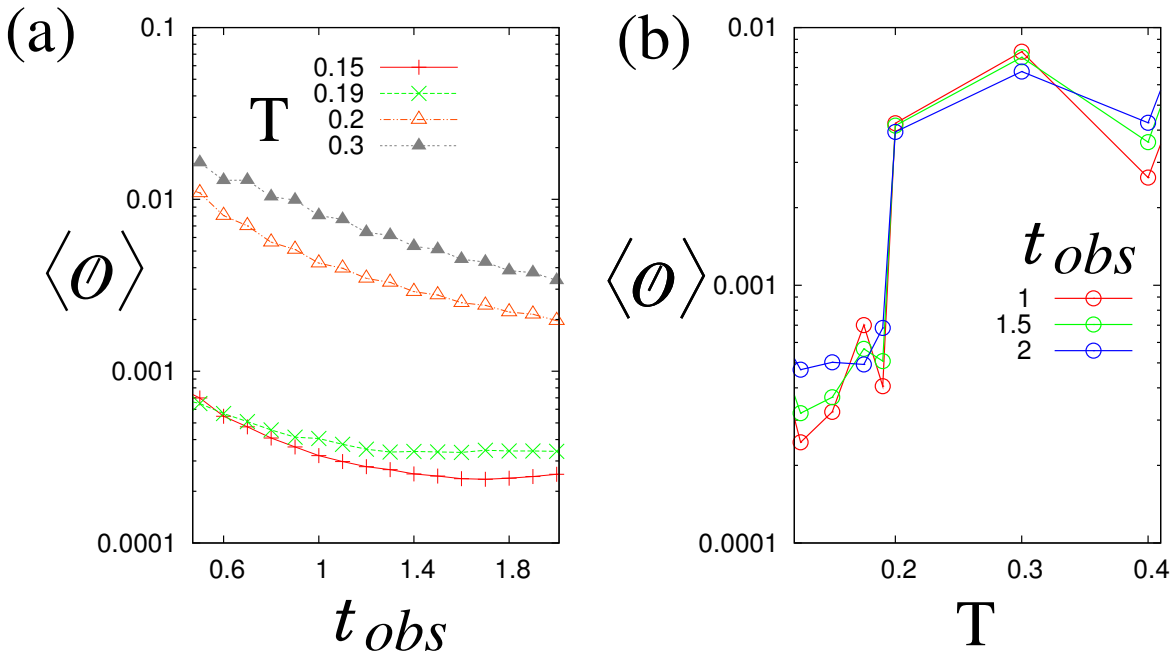

Figure 6.14: Plot of the mean entanglement order parameter $\langle \mathcal{O} \rangle$ plotted as a function of t_{obs} for various $T = 0.15, 0.19, 0.2, 0.3$ in (a) and as a function of T for various $t_{obs} = 1, 1.5$ and 2 in (b).

6.7 Conclusion

We have shown that the dynamics of solid state transformation and microstructure selection is closely associated with the generation and dynamics in and of dynamical heterogeneities. The clear separation of time scales between microscopic trajectories and mesoscopic microstructure, immediately suggests a causal connection between microscopic trajectories of active particles kinetically confined by inactive particles in dynamical heterogeneities, the stress-flow characteristics of NAZs [85] and the microstructure. We have thus demonstrated that it is the nature of active particle movement that decides the fate of the transforming solid. In doing so our work addresses the fundamental problem of microstructure selection, namely, how do the particles of the parent solid "know" how to position themselves with respect to each other, so as to form a product with a specific microstructure and precise relations at the parent-product interface ? When the topog-

raphy of potential energy landscape is such that single particle diffusive excitations are suppressed, then the solid state transformation proceeds via rare string-like correlated excitations involving a small number of particles, giving rise to a twinned microstructure with compatible parent-product interfaces. A shallower topography permits single particle diffusive excitations; the solid then transforms into a ferrite with highly distorted parent-product interfaces. The dynamical heterogeneities so generated can form a percolating network giving rise to the possibility of a new kind of glass obtained during a solid-solid transformation.

Chapter 7

Structural transitions with open boundary conditions: Shape reversibility

7.1 Introduction

In the previous chapters of the thesis we have described static and dynamic aspects of structural transitions in solids under situations where the overall shape of the solid remains fixed. Martensitic transformations in real materials, on the other hand are always accompanied by changes of overall shape of the solid. This may be in the form of localized surface relief effects producing ridges and furrows on the surface as the transformation proceeds. Here, in this chapter, we intend to study such structural transitions and microstructure formation by treating the two dimensional model system with *open* (as opposed to *periodic*) boundary conditions. This feature is exclusively introduced to study shape transformations accompanying the formation of martensite. The technique used to create such conditions needs an additional term in the Hamiltonian *viz.* the *glue* potential. In the next section we describe the nature of the glue potential. Section 7.3 deals with the effect of the *glue* potential on the equilibrium properties of the system. The results are obtained for both $\alpha = 0$ and $\alpha \neq 0$. Finite temperature calculations are discussed in section 7.4. To check for developing microstuctures, low and high temperature quench protocols are performed similar to those discussed in chapter 5. In the last section of the chapter, we further study the kinetics of shape recovery in our model solid undergoing transformations from a square to general rhombic lattice using molecular dynamics simulations. We determine the necessary and sufficient conditions for such shape recovery in terms of the nature and dynamics of transient and localized non-affine zones

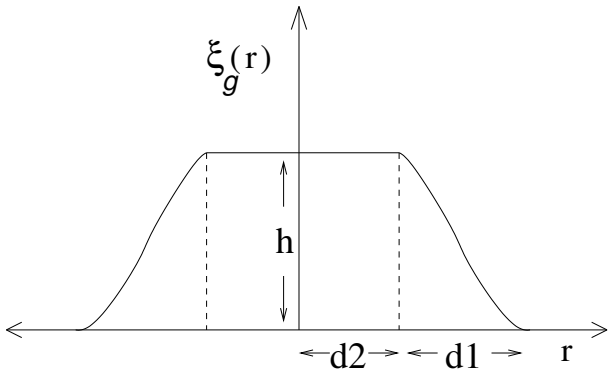

Figure 7.1: Schematic diagram showing the profile for the glue density used to set up the open boundary conditions.

(NAZs) which inevitably accompany the transformation.

7.2 The glue potential

In order to study the influence of martensitic structural transformations on external shape, we need an isolated solid with stress free boundaries. This allows for deformations of shape of the solid as it transforms. In this section we introduce the model potential which allows us to undertake this study and investigate its ground state and equilibrium properties. To this end we associate every particle in the lattice with a "glue" density $\xi_g(\mathbf{r})$ given by

$$\begin{aligned} \xi_g(\mathbf{r}) &= h \quad \text{for } \mathbf{r} < \mathbf{r}_{d2} \\ &= \sum_{n=0,3} A_n \mathbf{r}^n \quad \mathbf{r}_{d2} < \mathbf{r} < \mathbf{r}_{d1} \\ &= 0 \quad \mathbf{r} > \mathbf{r}_{d1} \end{aligned} \tag{7.1}$$

Here h refers to the amplitude of the glue density. The cutoffs $\mathbf{r}_{d2}$ and $\mathbf{r}_{d1}$ correspond approximately to the first and second nearest neighbour distances. In our lattice system we have taken both $\mathbf{r}_{d1}$ and $\mathbf{r}_{d2}$ equal to 1.5 and $h = 1.0$. Beyond $\mathbf{r}_{d1}$ the density reduces to zero. As defined peviously, $\mathbf{r} \equiv |\mathbf{r}_{ij}| \equiv |\mathbf{r}_j - \mathbf{r}_i|$. The coefficients A_n are chosen such that $\xi_g(\mathbf{r})$ is smooth and continuous for all $\mathbf{r}$. Matching the function $\xi_g(\mathbf{r})$ and its derivatives

we obtain,

$$\begin{aligned} A_0 &= 2h/((d1)^3) \\ A_1 &= -3h((d1)+2(d2))/((d1)^3) \\ A_2 &= (6h(d2))((d1)+(d2))/((d1)^3) \\ A_3 &= h(d1)^3 - 2h(d2)^3 - 3h(d1)(d2)^2/((d1)^3) \end{aligned} \tag{7.2}$$

The embedding energy of particle i in this glue is $V_g = -K_g \sum_{j=1,N} \xi_g(\mathbf{r}_{ij})$, where K_g is the cohesive energy. We have taken $K_g = 3.0$ for our calculations which produces an average solid density close to $\rho = 1.05$. The glue makes the particles stick to each other forming a two dimensional solid. The contribution of the glue potential to the total energy is $K_g \sum_{i=1,N} \rho(\mathbf{r}_i)\xi_g(\mathbf{r}_i) = K_g \sum_{i=1,N} \rho(\mathbf{r}_i) \sum_{j=1,N} C^g_{ij}\rho(\mathbf{r}_j)$, where $\rho(\mathbf{r}_i)$ is the local number density and C^g_{ij} is non-zero only upto the next nearest neighbour shell. This reduces to a quantity proportional to the average density ρ together with a boundary contribution scaling inversely with system size L. In the thermodynamic limit, this simply leads to a resetting of the chemical potential. The shape of the boundary of the solid is self-consistently determined by the many-body interaction among particles alone. The value of K_g is chosen to be large enough such that there is negligible loss of particles from the solid and the nearest neighbour distance is roughly maintained to be constant across the transformation. On the other hand the area A and shape of the solid may vary at fixed pressure and T.

7.3 Equilibrium properties

We now proceed to study the equilibrium properties at $T = 0$ temperature. We first consider the isotropic two-body, three-body and glue potential to get the the jump in the order parameter e_3 across the transition. Starting with an initial square lattice comprising of $N = 2500$ particles at $\rho = 1.05$ inside a box of size 243.975×243.975 we observe the square to rhombic transition for various values of the order parameter e_3. Due to the inclusion of the glue, we find that $|\Delta e_3|$ increases to ± 0.29 for the transition at $\alpha = 0.0$. Fig. 7.2 shows the jump in e_3 at $v_3 = 2.067$. For the same set of parameters we calculate the variation of pressure, $P = \sigma_1$, dilational stress, $\sigma_2 = \partial E/\partial e_2$ and effective shear,

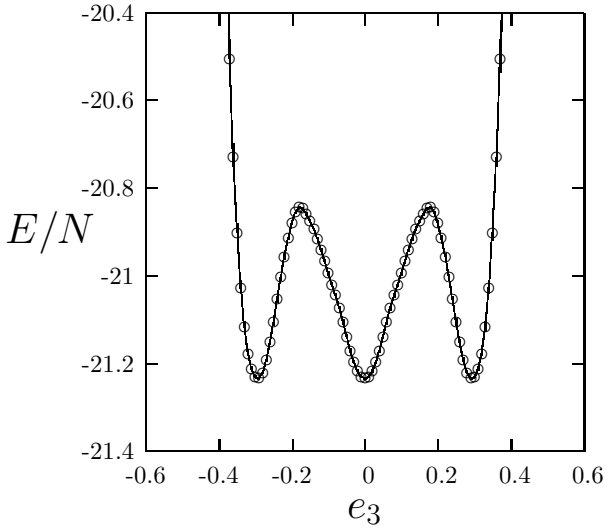

Figure 7.2: Figure shows the variation of E/N with the order parameter strain e_3 for calculations with the additional glue potential at $v_3 = 2.067, \rho = 1.05, T = 0, \alpha = 0.0$ for $N = 2500$ particles inside a box of size 243.975×243.975. The jump $|\Delta e_3| = \pm 0.29$.

$\sigma_3' = \sigma_3 + Pe_3$ with e_3 starting from the initial square lattice. Figure 7.3 shows the variation of these quantities as a result of including the additional glue potential. The dilational stress fluctuates around zero and the effective shear stress is also zero for lower values of the order parameter.

Considering the anisotropic two body potential at $T = 0.0$ with $\alpha = 1.0$ along with the three body and glue potentials, we find that the jump in the order parameter strain decreases as expected from our discussion in chapter 3. We obtain $|\Delta e_3| = \pm 0.065$ for a square lattice of $N = 14400$ particles at $\rho = 1.05, v_3 = 1.0935$ in a box of size 819.7561×819.7561 (fig 7.4).

7.3.1 T = 0 phase diagram

The zero temperature phase diagram in the $v_3 - \alpha$ plane with the additional glue potential is shown in fig. 7.5. As compared to earlier results, the inclusion of the glue potential shifts the line of transition to higher values of α such that the square phase is stable only at some-what larger α values. The tricritical point, α_c is now at $\alpha = 4.2, v_3 = T = 0$

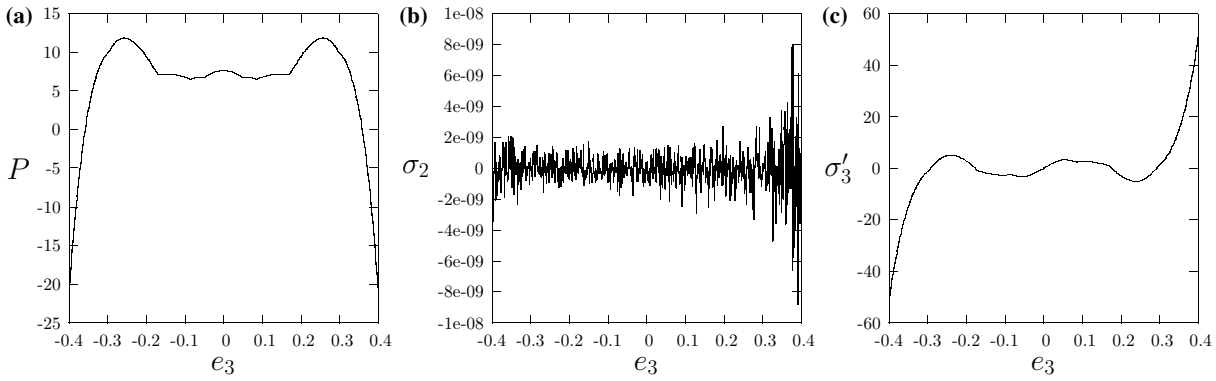

Figure 7.3: Variation of pressure, P (a), dilational stress, σ_2 (b) and effective shear σ_3' (c) as a function of the order parameter strain e_3. The calculations are done with the additional glue potential at $v_3 = 2.067, \rho = 1.05, T = 0, \alpha = 0.0$ for $N = 2500$ particles in a box of size 243.975×243.975.

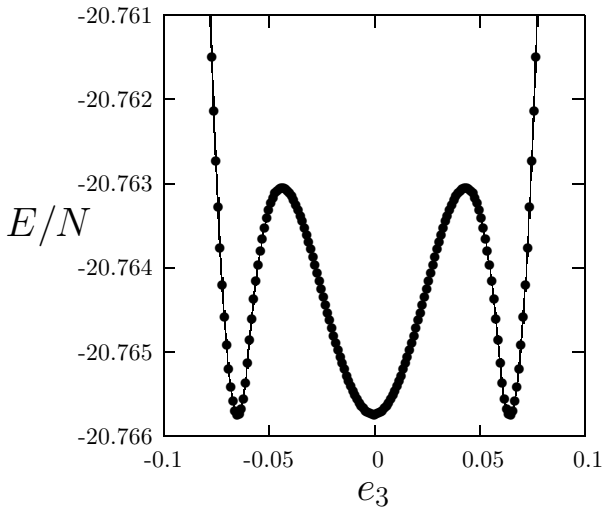

Figure 7.4: Variation of E/N with the order parameter strain e_3 for calculations with the additional glue potential at $\alpha = 1.0, v_3 = 1.0935, \rho = 1.05, T = 0$ for $N = 14400$ particles in a box of size 819.7561×819.7561. The jump during the transition decreases giving $|\Delta e_3| = \pm 0.065$.

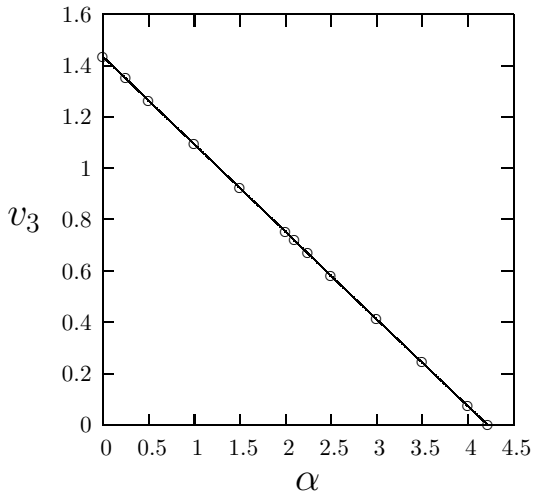

Figure 7.5: Phase diagram in the $v_3 - \alpha$ plane with the additional glue potential at $T = 0$. The line of transition shifts to higher values of α stabilizing the rhombic lattice for a larger range. The tricritical point α_c is at $\alpha = 4.2, v_3 = T = 0$. The calculations were done with $N = 14400$ particles at $\rho = 1.05$ in a box of size 819.7561×819.7561.

where the jump in e_3 becomes zero.

7.4 Finite temperature calculations

To perform finite temperature calculations, we first verify whether the glue potential is still able to bind the solid compactly without the loss of particles from the lattice. A close look at the equilibrium configuration snapshots in fig. 7.6 obtained for two different system sizes reveals that particles stick to each other forming a two dimensional solid.

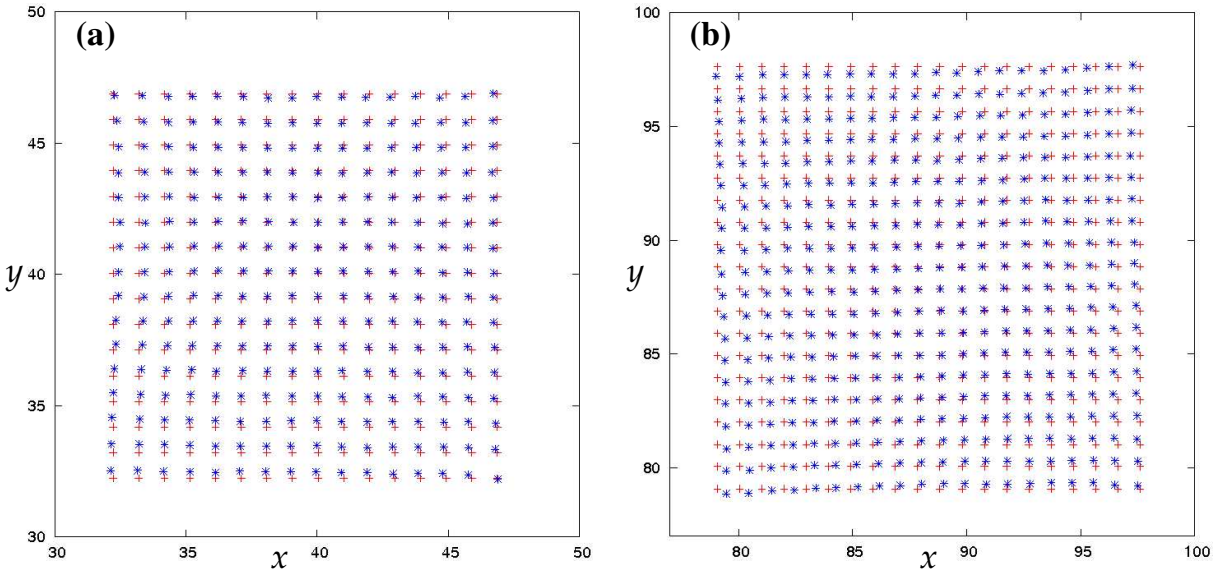

Figure 7.6: Equilibrated square lattice consisting of (a) $N = 256$ particles in a box of size 78.072×78.072 and (b) $N = 400$ particles in a box of size 175.662×175.662 at $v_3 = 5.0$ obtained using the glue potential along with two-body and three-body potentials. The lattice parameter is 0.9759 at $\rho = 1.05, T = 0.1$ and $\alpha = 0.0$. In both the figures (+) represents the initial square lattice while (*) represents the lattice after equilibration. Note the overall compression of the square lattice in the equilibrated configurations.

Next we equilibrate both the square and rhombic lattice configurations at $v_3 = 10.0$ and $v_3 = 0.5$ respectively. In both cases, the system consists of $N = 14400$ particles inside a simulation box of size 819.7561×819.7561 at $\rho = 1.05, T = 0.1, \alpha = 1.0$. The values of K_g and h are fixed at 3.0 and 1.0 respectively. During equilibration, we calculate the diffusion constant $D_c = Lt_{t\to\infty}(1/4t)(< |\mathbf{r}(t) - \mathbf{r}(0)|^2 >)$ to check whether particles at the boundary diffuse away. Also the average torque about the centre of mass of the system must be equal to zero. Figures 7.7 (a) and (b) shows the equilibrated lattices along with their respective D_c. Both the lattices remain as a perfect solid inside the box after equilibration. D_c is calculated for few surface layers along a side of the lattice and as the system equilibrates, it decreases indicating that particles stick to each other during the simulation. The spatial profiles for the glue density and glue energy for both the equilibrated square and rhombic lattice configurations are obtained as shown in figs 7.8 and 7.9. The averaged spatial profiles for both the glue density and glue energy in both types of lattice reveals that it is nearly constant and independent of the crystal structure throughout the interior of the solid with variations seen mainly at the periphery.

We now calculate the local stress components for both the equilibrated sqaure and rhombic lattice configurations at $T = 0.1$. Fig. 7.10 shows the plots for the data obtained after averaging over 101 equilibrium configurations. From the figure it is clear that σ_{xy} is almost zero spatially throughout the lattice in both types of configurations. Also the spatial profiles of $\sigma_{xx} + \sigma_{yy}$ and $\sigma_{xx} - \sigma_{yy}$ show fluctuations about zero. Thus for low temperatures, the spatial stress profiles show that it is possible to have the system with open boundary conditions in a stress-free ensemble with our model glue potential.

However, at higher temperatures *i.e.* $T = 0.6$, equilibration of the same system consisting $N = 14400$ particles at $v_3 = 10.0, \rho = 1.05$ and $\alpha = 1.0$ depicts a different picture. Fig. 7.11(a) shows the lattice snapshot at 600000 md-step. We find that at such high temperatures surface amorphization occurs. The solid lump stays inside the simulation box but the particles near or at the surface are located in several positions away from the solid. This is evident in figure 7.11(b) which shows that the diffusion constant evaluated for few surface layers decreases gradually but has a much higher value compared to that obtained at low temperatures ($T = 0.1$). Note that the diffusion constant equilibrates to a vanishingly small value indicating that our system of particles is, infact, a solid despite

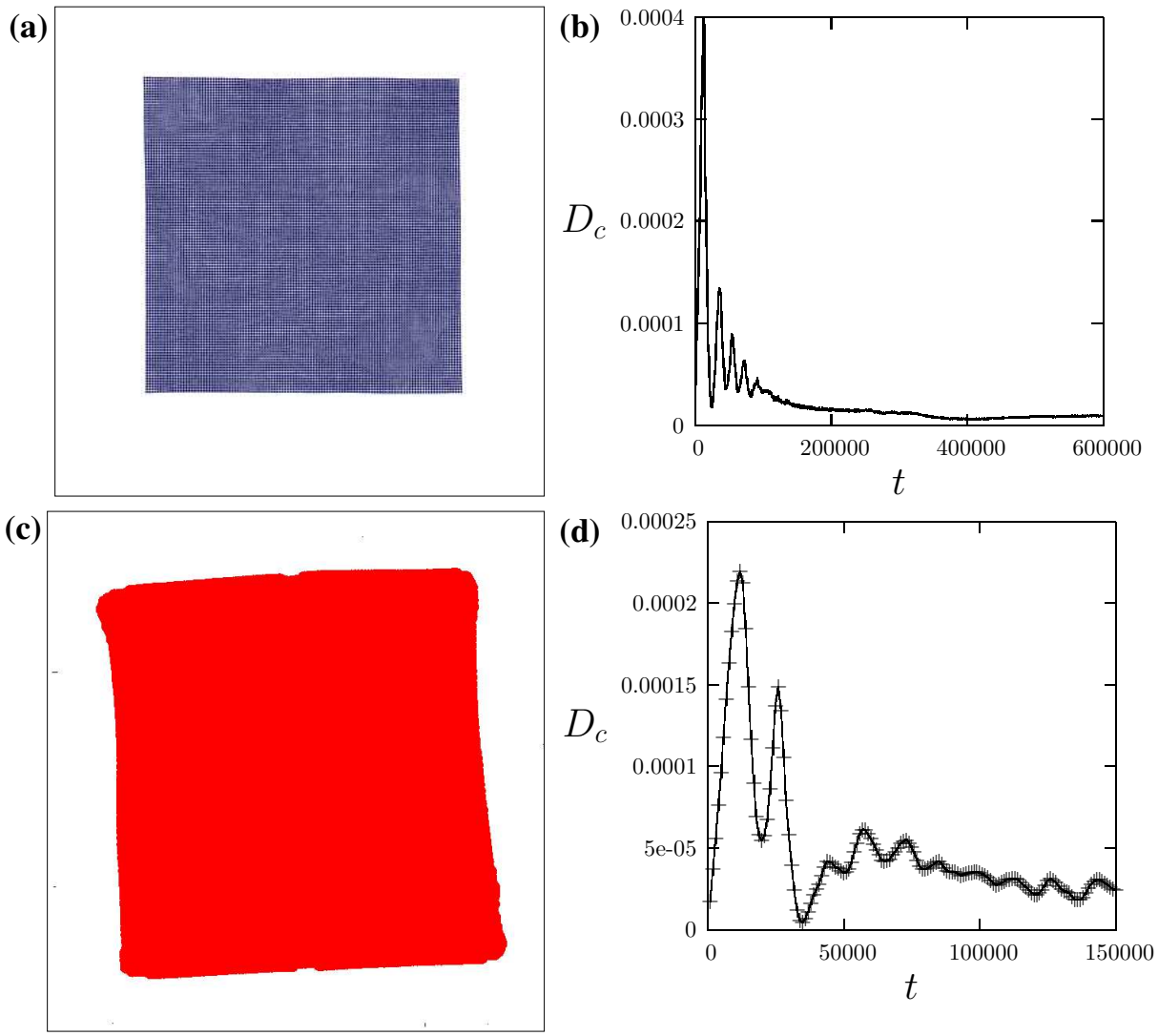

Figure 7.7: (a) Equilibrated square lattice with $N = 14400$ in a box $(819.7561 \times 819.7561)$ at $v_3 = 10.0, \rho = 1.05, T = 0.1, \alpha = 1.0$. The snapshot is at 401000 molecular dynamics time-step; (b) the diffusion constant D_c for the square lattice evaluated during the simulation. (c) Equilibrated rhombic lattice at 150000 molecular dynamics time-step consisting of $N = 14400$ particles in a simulation box of 819.7561×819.7561 at $v_3 = 0.5, \rho = 1.05, T = 0.1$ and $\alpha = 1.0$; (d) diffusion constant D_c for the rhombic lattice evaluated during the simulation.

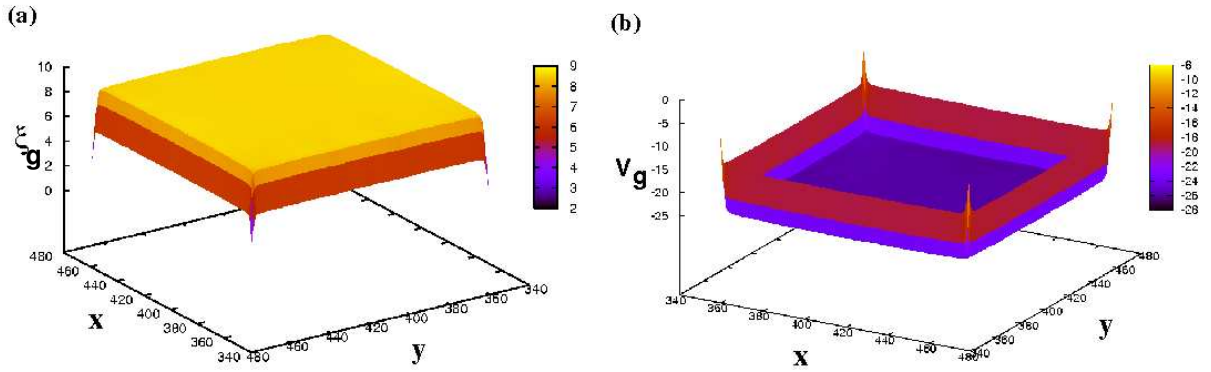

Figure 7.8: Average spatial profiles for glue density ξ_g and glue energy V_g obtained for a square lattice consisting of $N = 14400$ particles in a simulation box of 819.7561×819.7561 at $v_3 = 10.0, \rho = 1.05, T = 0.1$ and $\alpha = 1.0$. The average is over 100 equilibrated configurations.

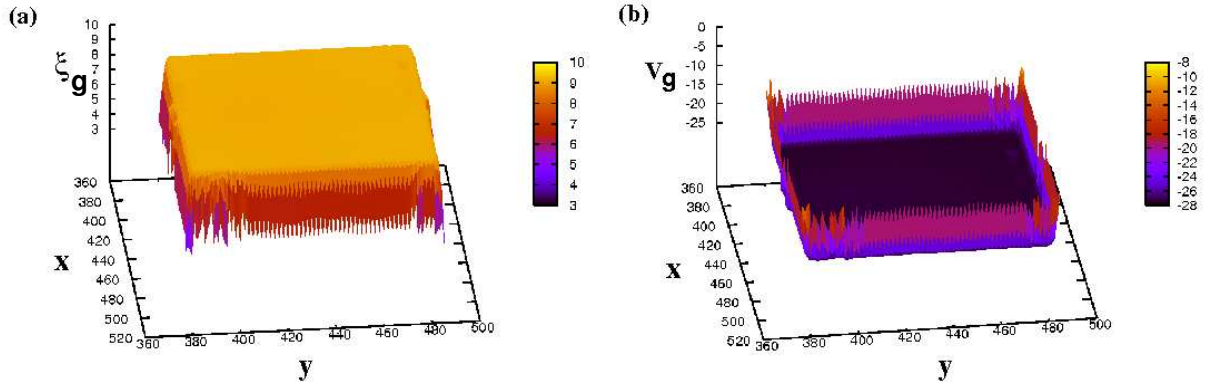

Figure 7.9: Average spatial profiles for glue density ξ_g and glue energy V_g obtained for a rhombic lattice consisting of $N = 14400$ particles in a simulation box of 819.7561×819.7561 at $v_3 = 0.5, \rho = 1.05, T = 0.1$ and $\alpha = 1.0$. The profiles are obtained after averaging over 100 equilibrium configurations.

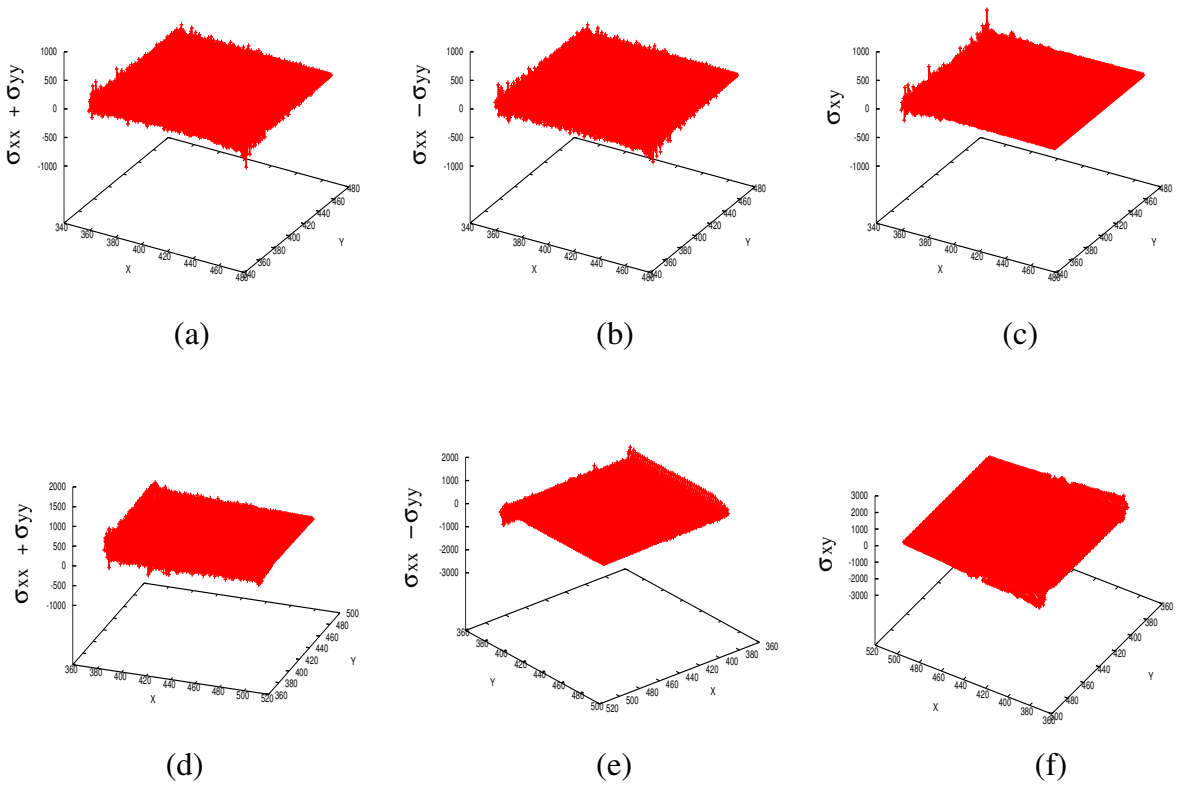

Figure 7.10: Spatial plot of the local stress components $\sigma_{xx} + \sigma_{yy}, \sigma_{xx} - \sigma_{yy}$ and σ_{xy} for a square and rhombic lattice consisting of $N = 14400$ particles in a simulation box of size 819.7561×819.7561 at $\rho = 1.05, T = 0.1$ and $\alpha = 1.0$. The square lattice data is represented by (a),(b),(c) while the rhombic lattice by (d),(e) and (f). From the plots it is inferred that with the glue potential it is possible to obtain stress-free conditions.

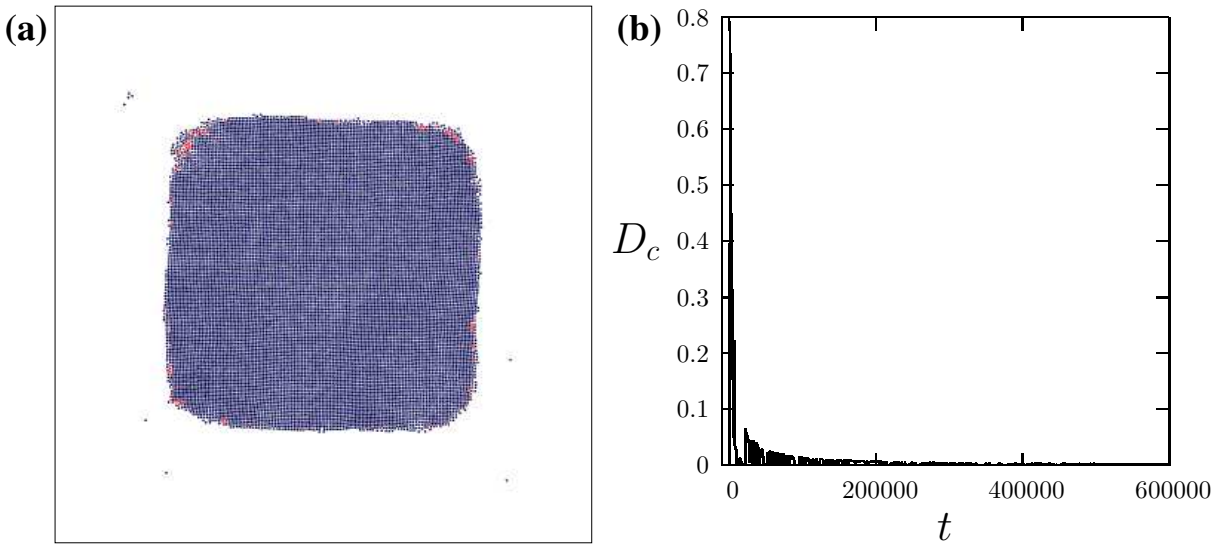

Figure 7.11: (a) Equilibrated square configuration at $T = 0.6$ consisting of $N = 14400$ particles in a box of 819.7561×819.7561. Surface amorphization occurs at $v_3 = 10.0, \rho = 1.05, \alpha = 1.0$. (b) The diffusion constant D_c has higher values as surface particles are scattered inside the box.

extensive atomic rearrangements occuring at the surface. The total torque about the centre of mass fluctuates around zero keeping the solid at the centre of the simulation box.

Hence we obtain satisfactory results with our formulation of the glue potential even at finite temperatures.

7.4.1 Phase diagram

The finite temperature phase diagram for the system subjected to the two-body, three-body ang glue potential is obtained by observing the final configuration during a square to rhombic structural transition. Starting from an initial square configuration consisting of $N = 14400$ particles at $\rho = 1.05$, we vary the value of the potential parameter v_3 for various temperatures. The final configuration at $25 \times 10^3 \Delta t$ is verified for the transformation. Figure 7.12 shows the phase transition line in the $v_3 - T$ plane for both $\alpha = 0$ and $\alpha = 1.0$. Due to the presence of the glue potential the line of transition shifts to higher

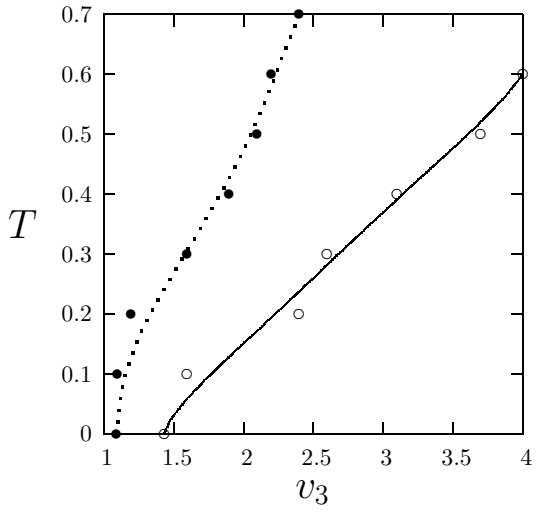

Figure 7.12: Phase diagram in the $v_3 - T$ plane obtained for the system subjected to the confining potential with $N = 14400$ particles at $\rho = 1.05$ for $\alpha = 0$ (open circle) and $\alpha = 1.0$ (filled circle). The line of transition shifts to lower values of v_3 stabilizing the square lattice for a larger range for $\alpha \neq 0$.

values of v_3 as compared to the phase diagram obtained without the confining potential (fig. 4.3). Also, for the anisotropic potential, the transition line shifts to lower values of v_3. Therefore, we conclude that even with the additional glue potential the nature of the phase diagram qualitatively remains the same. The three dimensional phase diagram in the $T - v_3 - \alpha$ planes is schematically represented in fig. 7.13. The equilibrium square and rhombic phases are separated by solid lines and the black dot marks the tricritical point. Following the phase curves we carry out the quench protocols Q_1 and Q_2 by starting with an initial square solid at $t = 0$.

7.4.2 Quenches and microstructures

In order to study shape reversibility in martensitic phase transformations we need to quench the lattice with $N = 14400$ particles subjected to the anisotropic two-body, three-body and glue potential. After equilibration is complete, we perform direct quenching protocols both at low and high temperatures. In case of the low temperature quenching at $T = 0.1$, the system with a single seed at the centre is quenched to $v_3 = 0.5$. The different

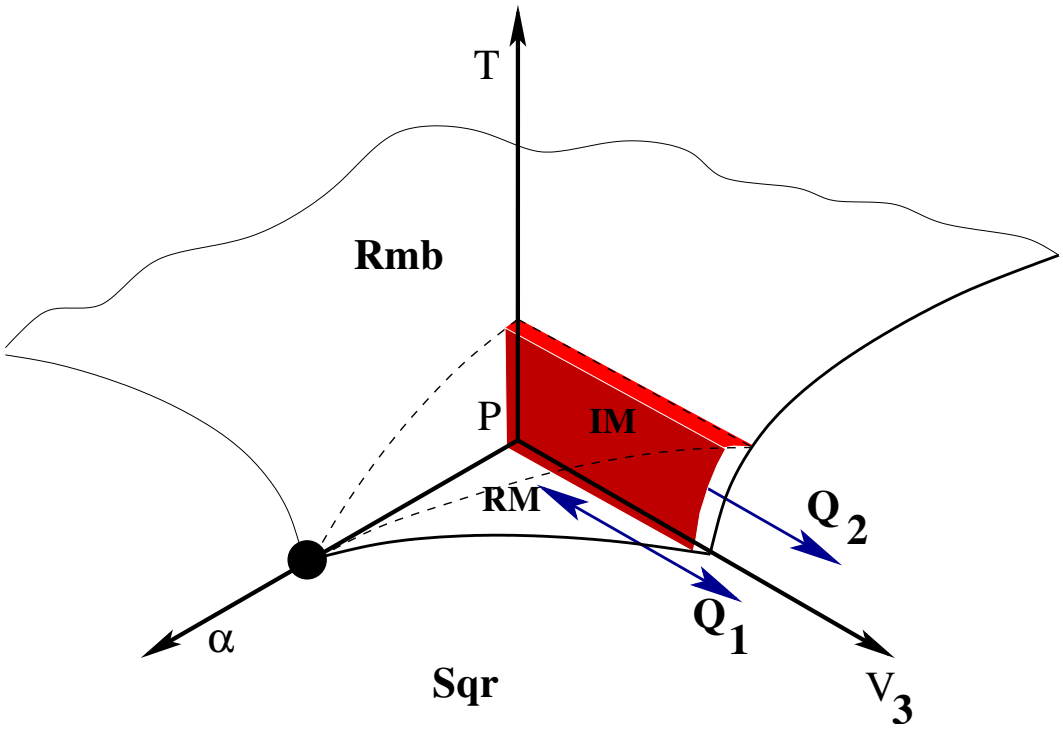

Figure 7.13: Schematic dynamical phase diagram in $T - v_3 - \alpha$ planes (*i.e.* similar to figs. 4.9 and 5.1), showing equilibrium phases (square (Sqr) and rhombus (Rmb)) by solid lines. The triangular (Trg) solid exists for $\alpha = v_3 = 0$ – point P. The black dot marks the location of a tricritical point at which the jump in the order parameter vanishes. The dynamical phase martensite is formed for quenches at T below the curved surface bounded by the dashed lines. Dynamical martensitic phases upon cycling: reversible (RM) and irreversible (IM) martensite (red region) are shown. The quench and cycling protocols Q_1 and Q_2 are denoted by arrows.

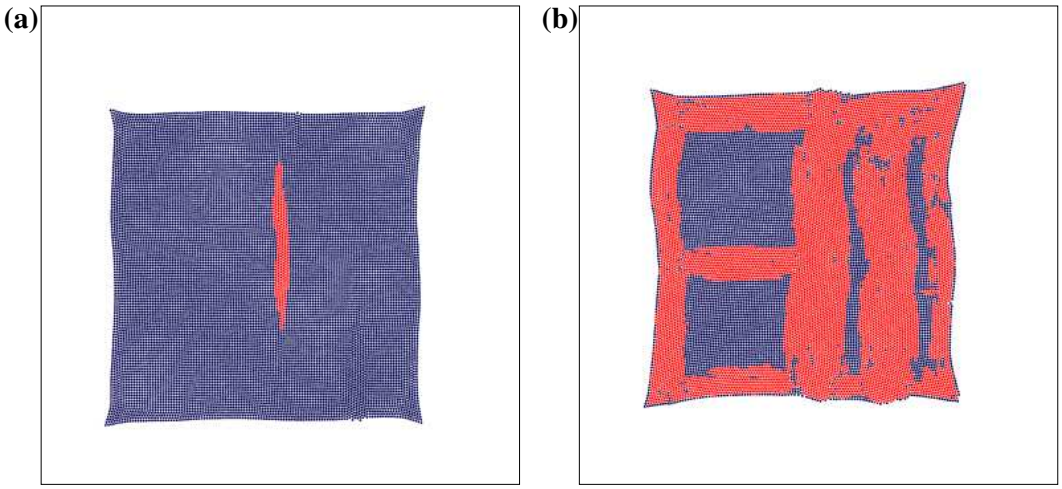

Figure 7.14: Molecular dynamics snapshots obtained at (a) 2600 and (b) 10000 timesteps. Colours blue to red correspond to the bond angle order parameter which is zero in the square and and non-zero in the rhombic phase. The system of $N = 14400$ particles with a seed at $\rho = 1.05, T = 0.1, \alpha = 1.0$ is quenched suddenly to $v_3 = 0.5$ after equilibration at $v_3 = 10.0$.

molecular dynamics snapshots are shown in fig .7.14. There is anisotropic growth giving rise to the martensite microstructure. As the box size of 819.7561×819.7561 is much larger and there is no periodic boundary conditions, the growing martensite spreads over the whole lattice if simulated for a reasonably long time. The high temperature direct quench molecular dynamics snapshots are shown in fig. 7.15. The quenching is from $v_3 = 10.0$ to $v_3 = 1.0$ at $T = 0.6$. Due to surface amorphization, there is no specific microstructural growth possible even with an initial seed inside the lattice. As time progresses, the amorphization increases and penetrates further into the lattice.

7.5 Shape recovery in solids undergoing martensitic transformations

Shape memory alloys [99] are examples of materials where the phase change is perfectly reversible. Such alloys and smart materials [100] have a wide range of technological applications ranging from medicine to information technology, robotics [101], actuators and

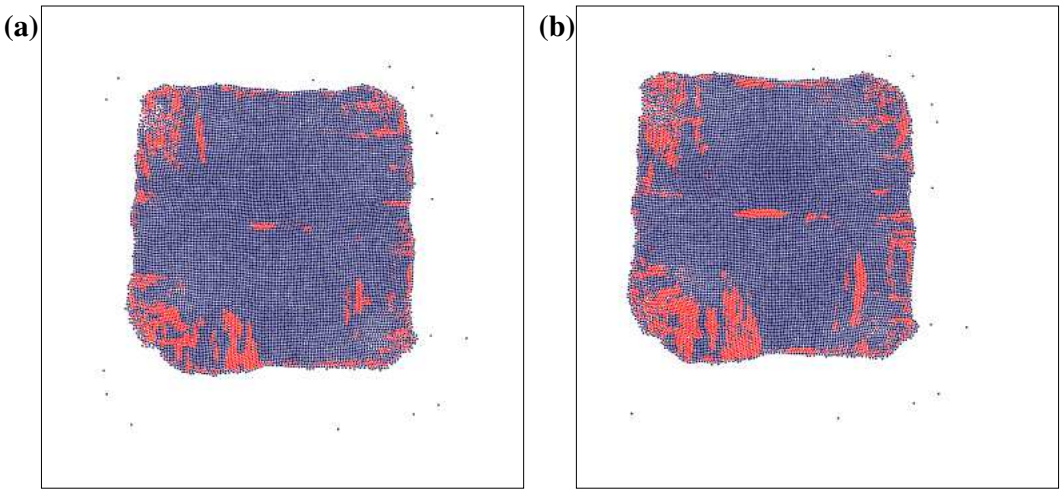

Figure 7.15: Molecular dynamics snapshots obtained at (a) 1500 and (b) 2000 timesteps for high temperature direct quench protocol. Colours blue to red correspond to the bond angle order parameter which is zero in the square and and non-zero in the rhombic phase. The system of $N = 14400$ particles with a seed at $\rho = 1.05, T = 0.6, \alpha = 1.0$ is quenched suddenly to $v_3 = 1.0$ after equilibration at $v_3 = 10.0$.

sensors [102, 103]. Martensites [8] are phenomenologically classified into two different classes. Based upon their ability to recover the external shape under thermal (or stress) quench cycle treatments, the classification gives *reversible* and *irreversible* martensites. A shape memory alloy such as Nitinol, belonging to the $Ni - Ti$ class of alloy, when cooled from the high temperature face-centered cubic phase undergoes a martensitic transformation forming twinned plate-like microstructures in the body-centered tetragonal form. With the application of load in the cold state along with heating, disappearence of the twinned microstructure occurs. In contrast, irreversible martensites such as steel, $CoNi$ do not show shape recovery. Also unlike the reversible transformations, the parent phase obtained after one complete thermal cycle in case of the irreversible transformations contains dislocations and twinning. Therefore reversible martensites are required to obatin shape memory in materials.

We are interested in investigating the conditions under which the above mentioned two different types of martensitic transformation takes place. In a recent study, Bhattacharya *et al* [43] suggested that a necessary condition for reversibility of martensitic transforma-

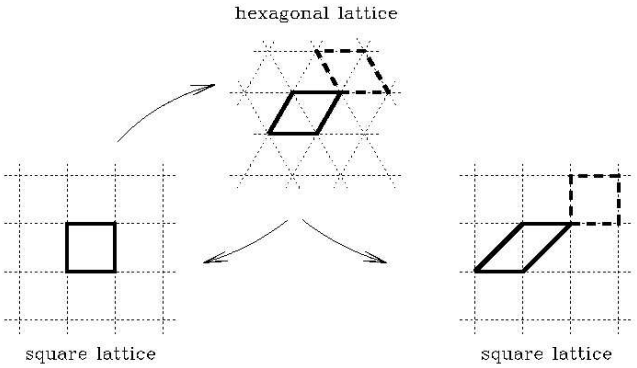

Figure 7.16: A reversible transformation of a square lattice to rhombic lattice and back can be obtained through the application of a lattice invariant shear. It is possible due to the presence of hexagonal symmetry which implies the equivalence of the solid rhombus with the dashed one in the middle figure. [Figure taken from [43]]

tions is simply related to the symmetry between the parent and product phases (fig. 7.16). If the parent and product are related by a group-subgroup relationship *viz.*, if they are derived from a common symmetry group then the resulting transformation is reversible. In such a case, a unique parent lattice can be identified for every transformed product. On the other hand, irreversibility implies that such an identification is impossible or ambiguous. We therefore argue that the necessary and sufficient conditions for reversibility depends on the dynamics of transformation during the thermal cycle [89].

7.5.1 Non-affine deformations and shape recovery

To study shape memory effect in martensitic transformations we need to perform gradual quenching schedules at low temperatures. Again for this purpose we use our two dimensional atomistic model along with the confining potential as descibed above to perform molecular dynamics simulations. Through it, we first check the validity of the symmetry-based criterion as a necessary condition for reversibility. Secondly we explore the dynamical conditions for reversibility linked with the sufficient condition for the transformation. This is done by simply changing a single potential parameter which allows us to explore

both reversible and irreversible martensites within the same model. Some of the issues concerning reversibility of microstructural patterns and the role of defects during martensitic transformations have been addressed using an effective spin Hamiltonian [104]. Our atomistic model goes beyond such studies enabling us to follow the transformation in microscopic detail. Also it takes care of the significant production of dislocations and growth of NAZs during irreversible martensitic transformations.

In our model solid we can change the group-subgroup relation of the parent product by changing the parameter α. Keeping $\alpha = 1.25$, we slowly quench the system by decreasing v_3 from $v_3 = 10.0 \rightarrow 0.5$ in steps of 0.5 holding the system for 10^4 molecular dynamics timesteps at each v_3. This is depicted by Q_1 in fig. 7.13. The square to rhombic phase transition at $v_3^* \approx 1.0$ breaks the Ising symmetry between the two degenerate rhombic minima. Since the presence of the surface breaks translational symmetry, nucleation predominantly proceeds from the surface or the corners. The crystal structure as well as the overall shape of the crystallite transform from square to rhombic as shown in fig. 7.17 (a). In the reverse quenching scheme when v_3 is gradually increased again, the shape change reverses in accordance with [43] to square as shown in fig. 7.17 (b).

The situation on the other hand, is quite different when $\alpha = 0.0$ shown by the Q_2 quenching protocol in fig. 7.13. The square to rhombic phase transtion occurs at $v_3^* = 1.4$ and as v_3 is further reduced in steps of 0.5 to zero, finally a triangular lattice results (fig. 7.18 (a)). The overall shape of the product crystal is not rhombic unlike the anisotropic case because the Ising symmetry is not completely broken and grain boundaries exist between different degenerate variants of the triangular phase formed at different portions of the crystallite. This is due to the fact that the energy of the grain boundary between the variants of the triangular product is low. During the reverse transformation, these grains tend to transform to different square lattices not necessarily the one which produced them in the first place. This sets up large internal stresses which are accomodated initially by shape deformations but cause the solid to rupture [105] when excessive (fig.7.18 (b)).

The overall shape change of the sample during a quench cycle, may be quantified as follows. We first identify boundary atoms by counting the number of nearest neighbours. The coordinates of the selected atoms are then used to define the shape function $r_S(\theta_S)$ with the angle θ_S measured from the x axis. The overall shape of the configuration as a

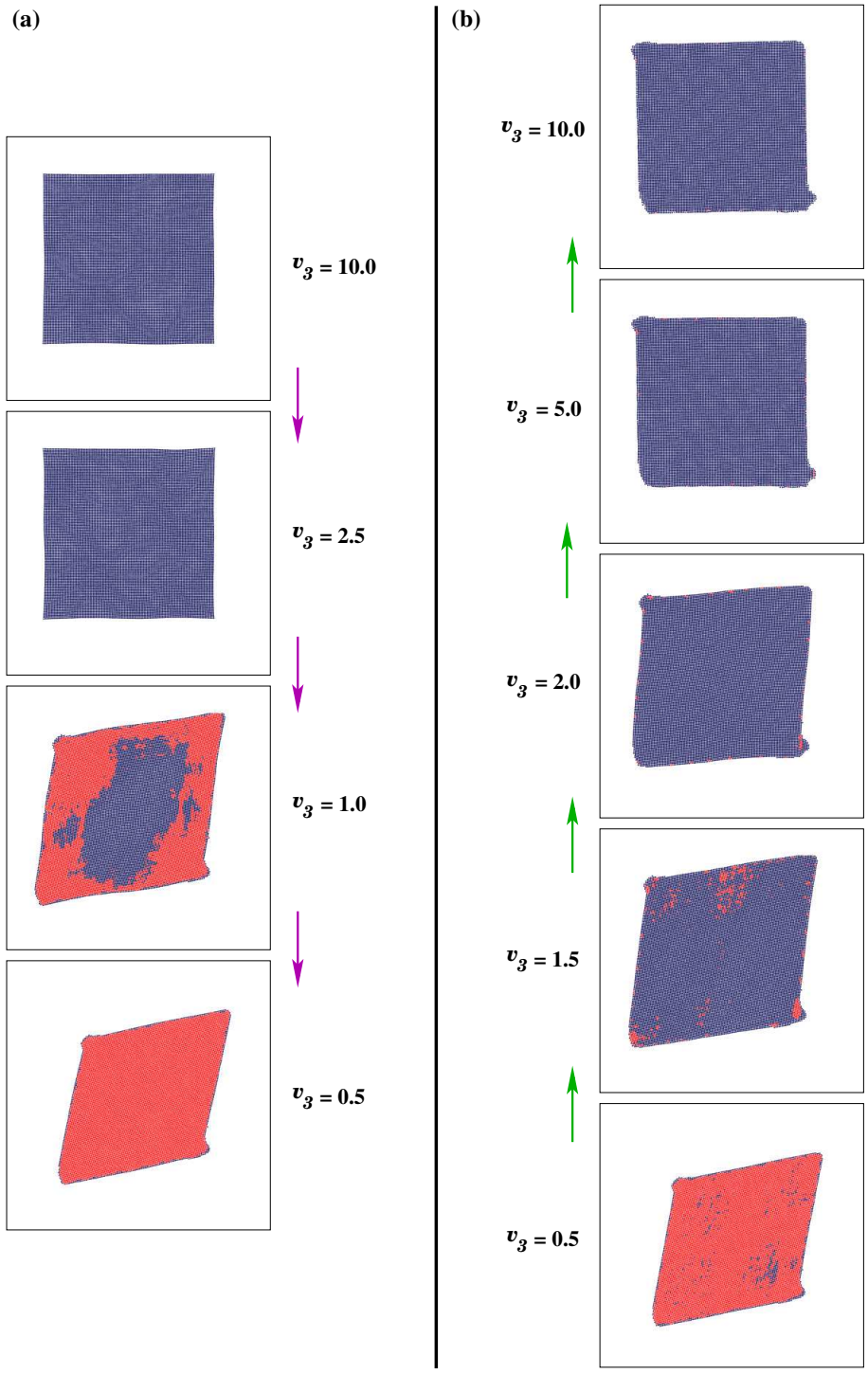

Figure 7.17: (a) Configurations of particles observed at various v_3 values during gradual quenching of the system from square to rhombic phase. v_3 is reduced from $10.0 \rightarrow 0.5$ in steps of 0.5. (b) Molecular dynamics snapshots at various values of v_3 during the reverse quenching procedure. v_3 is gradually increased from $0.5 \rightarrow 10.0$ in steps of 0.5. The system consists of 14400 particles at $T = 0.1, \rho = 1.05$ and $\alpha = 1.25$. The colours blue to red in the figures are again according to bond angle parameter which is zero for the untransformed square and non zero for the rhombic phase respectively.

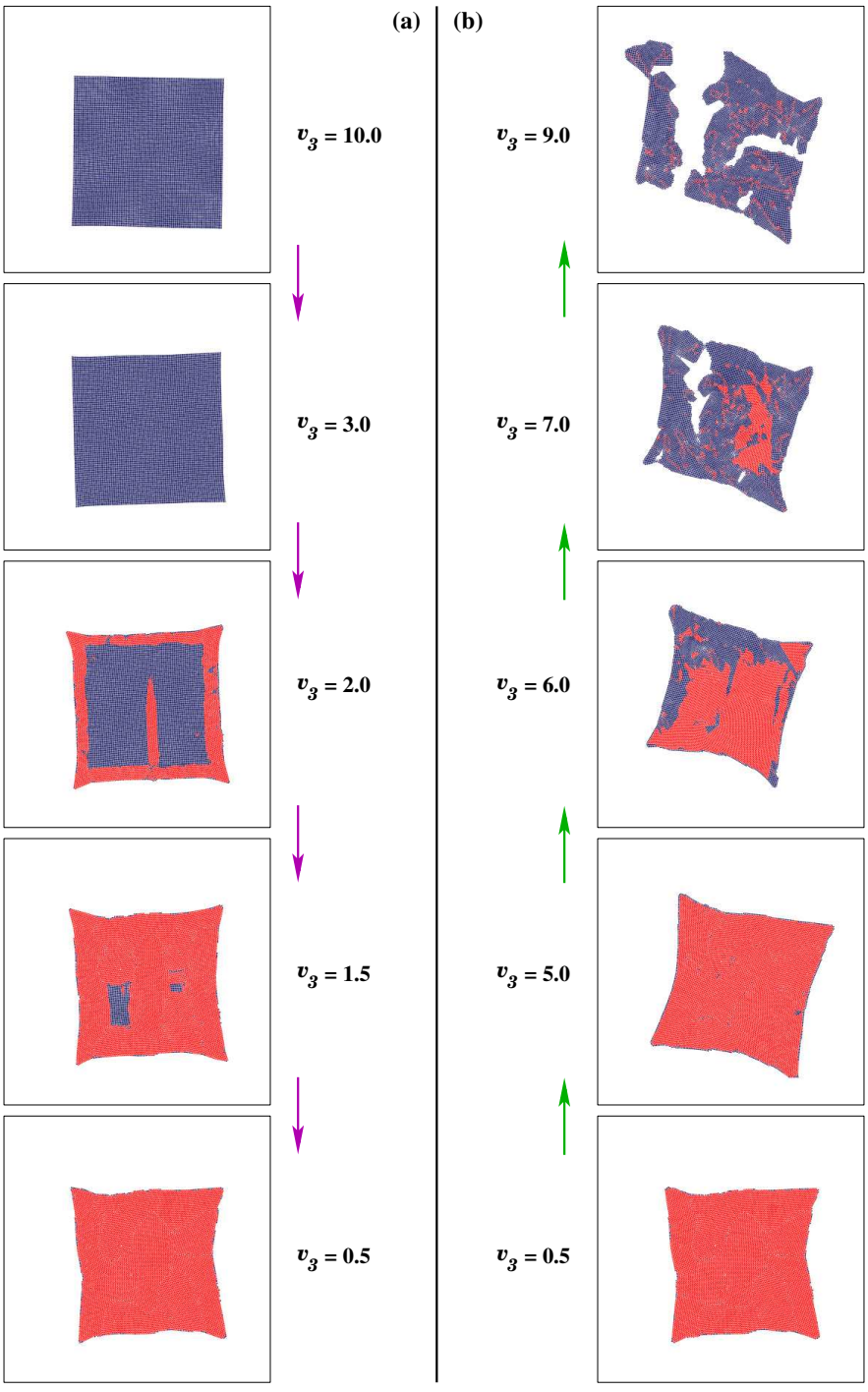

Figure 7.18: (a) Snapshots from molecular dynamics simulations obtained for isotropic gradual quenching protocol. v_3 is gradually reduced from 10.0 $\rightarrow$ 0.0 which ultimately gives the triangular lattice. (b) Molecular dynamics snapshots at various v_3 values obtained during the gradual reverse quenching procedure. v_3 is increased in steps of 0.5 from zero *i.e.* from the triangular phase. Due to the production of large internal stresses the solid ultimately ruptures before $v_3 = 10.0$ is reached. The quenching and reverse quenching procedures are done for a system of $N = 14400$ particles at $T = 0.1, \rho = 1.05$ and $\alpha = 0.0$. The colours blue to red are represented by the bond angle order parameter which is zero for square and non-zero for rhombic (triangular) phases respectively.

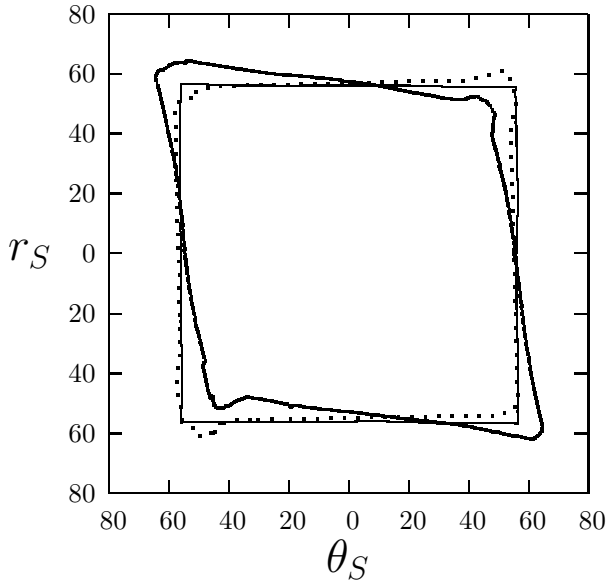

Figure 7.19: Polar plot showing the overall shape r_S for various configurations as a function of θ_S. The thin line represents the shape of the equilibrated square configuration at $v_3 = 10.0$. The thick line is for the quenched configuration obtained at $v_3 = 0.5$ after gradual quenching. The dotted curve is the shape of the configuration after gradual reverse quenching of the lattice at $v_3 = 10.0$. The confined system consists of $N = 14400$ particles at $\rho = 1.05, \alpha = 1.25, T = 0.1$.

function of θ_S is shown in the polar plot in fig. 7.19. Denoting as $r_S^{(0)}(\theta_S)$ as the shape of the initial square configuration, we have the overlap Δ_S given by

$$\Delta_S = \frac{1}{16L^2} \int \mathrm{d}\theta_S [r_S(\theta_S) - r_S^{(0)}(\theta_S)]^2 \tag{7.3}$$

where L is the system size and we have taken care to check for configurations related to the initial configuration by global translations and rotations. The result is plotted in fig. 7.20 for two values of α, as v_3 is reduced from a large initial value of 10 to 0.5 and then increased again for a system of $N = 14400$ particles. As expected, we observe that for $\alpha = 1.25$, the transformation is perfectly reversible. For $\alpha = 0.5$, when the product resembles the triangular phase, Δ_S tends to increase during the reverse transformation, showing that the shape change becomes irreversible. The value of Δ_S at the end of one cycle, Δ_{cycl} measures overall shape recovery at the end of the cycle. In fig. 7.22 we show the plot for Δ_{cycl} for a system of particles at $\alpha = 0.0$ as a function of N. In view of

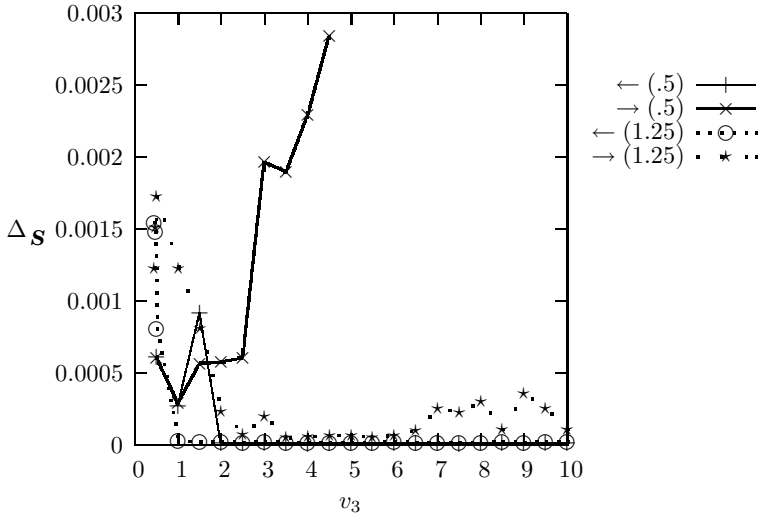

Figure 7.20: Overlap parameter Δ_S vs. v_3 at $T = 0.1$,$N = 14400$, and $\rho = 1.05$ for various values of α plotted during the forward ($\leftarrow$, decreasing v_3) and reverse ($\rightarrow$, increasing v_3) paths. The meaning of the symbols used are explained in the key to the left.

the conclusions drawn from [43], we observe a striking feature that the shape transformation, while irreversible for large N, becomes reversible as N decreases. This is shown in fig. 7.21 where we consider a system of $N = 100$ particles at $\rho = 1.05, \alpha = 0.0$ and $T = 0.1$ inside the simulation box subjected to the confining potential. After undergoing the gradual quenching and reverse quenching procedure the system almost regains its original shape. Increasing the cohesive energy K_g from 3.0 to 6.0 also reduces Δ_{cycl} and aids shape recovery (fig. 7.22).

We now demonstrate that all of these observations may be understood from the dynamics of non-affine zones (NAZs) which inevitably accompany the solid-solid structural transformation [85]. As described in chapter 5, we study the dynamics of NAZs by computing the local non-affine parameter using eqn. 5.2 by defining a neighbourhood Ω for every particle using a cut-off equal to the range of the potential ($\sim 2.5\sigma_0$).

The transformation connecting the square to rhombic phases is accompanied by NAZs as shown in fig. 7.23. Firstly, as in [33] and [85], these NAZs are in the non-order parameter sector, being associated with the local volume strain. They are mainly localized near the surface and rapidly disappear as the cystal transforms from square to the rhombic phase,

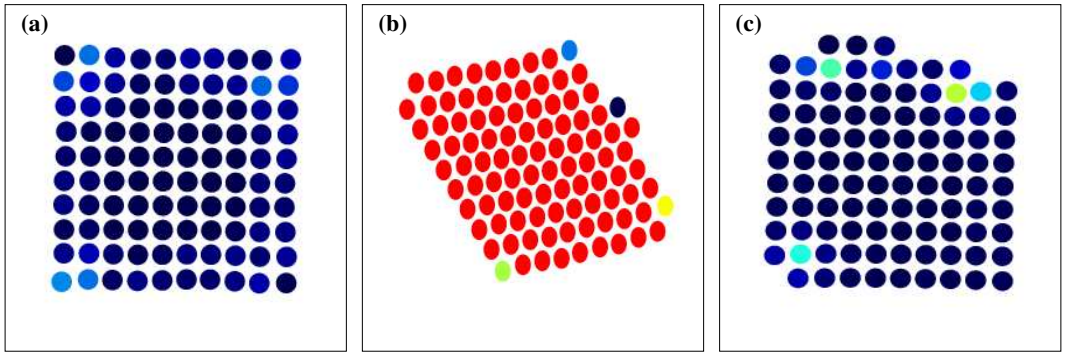

Figure 7.21: Configurations of $N = 100$ particles as v_3 is first reduced from (a) 10.0 to (b)0.5 and then increased to (c)10.0 for the square to rhombic transformation. The other parameters are : $\rho = 1.05, \alpha = 0.0, T = 0.1$. The colours are according to the bond angle parameter where blue represents a zero value (square) while red is for a nonzero value (rhombic). The small size of the system makes the system reversible even with $\alpha = 0.0$.

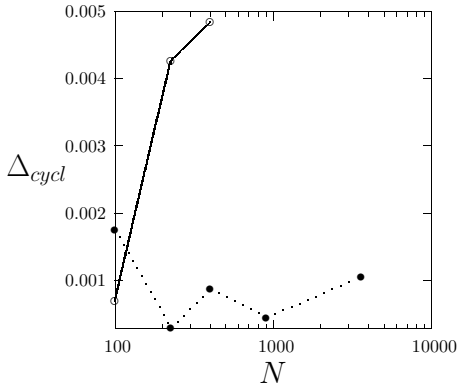

Figure 7.22: Shape recovery as measured by Δ_{cycl} – the difference in values of Δ_S after one cycle as a function of the size of the solid N for $\alpha = 0.0$, $K_g = 3$ (full line) and $K_g = 6$ (dashed line). Note that large cohesive energy (K_g) helps shape recovery.

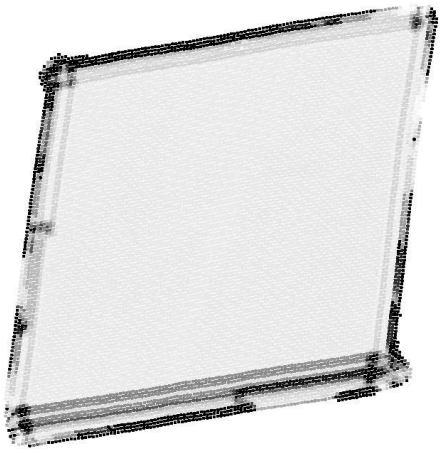

Figure 7.23: NAZs for the rhombic to square reverse transformation for $\alpha = 1.25, \rho = 1.05, T = 0.1, v_3 = 1.5$ for $N = 14400$ particles. Darker regions have larger D^2_Ω defined in eqn. 5.2. Note that the NAZs are confined mainly near the surface.

being advected out at the completion of the transformation. Secondly, as in [33] and [85], particles close to the NAZs within the transformed region move ballistically and in a coordinated manner. It is these two properties of the NAZs that ultimately render the square to rhombic martensitic transformation reversible, inspite of significant transient and localized plastic deformation.

Even the slightest amount of plasticity in the order parameter sector, on the other hand, would make the transformation irreversible. Within our model system, a deep quench to the $\alpha = 0.0, v_3 = 0.0$ region produces a triangular solid which is not related to the parent square lattice by a group-subgroup relation [106]. During the reverse transformation, therefore, there is no unique parent lattice that the system can revert to. This produces non-affineness in the order parameter sector due to a multiplicity of affine paths and hence destroys reversibility. The result from our molecular dynamics simulations is shown in fig. 7.24(a). It is interesting to note that the largest values of D^2_Ω exist along boundaries of isolated patches within which the transformation is to a single square lattice. Particles at the boundary of these patches are structurally frustrated and tend to follow seperate possible affine paths along trajectories which are disordered and 'diffusive' despite the temperature being low (fig. 7.24(b)). Unlike in reversible martensites, the creation of

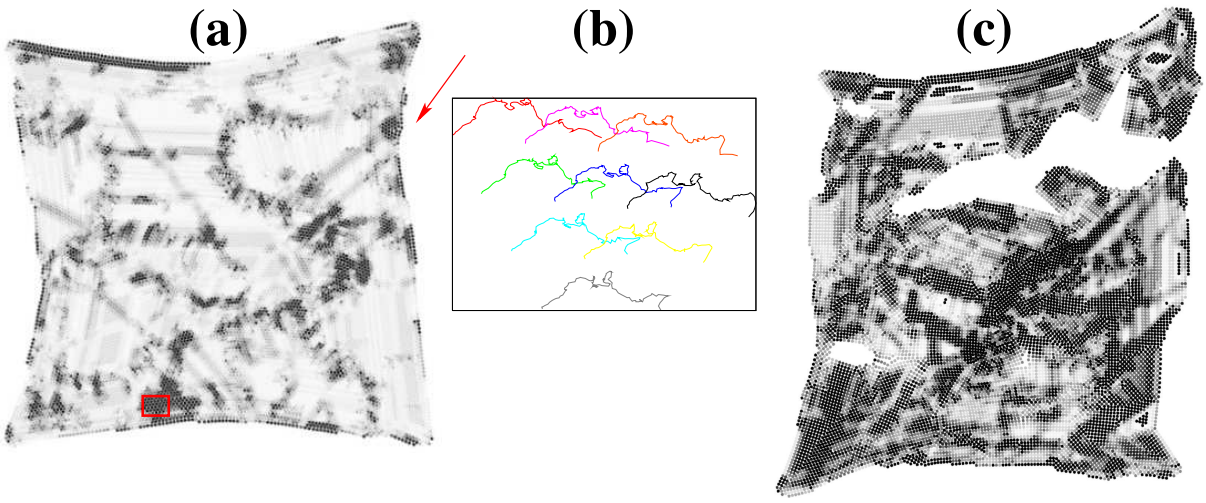

Figure 7.24: (a)The non affine parameter D^2_Ω for a triangular lattice during the reverse transformation at $v_3 = 5$, $\alpha = 0$, $\rho = N/L^2 = 1.05$ and $T = 0.1$. Dark regions correspond to large D^2_Ω within non-affine zones which surround isolated and disjoint regions where D^2_Ω is small. (b) Particle trajectories in a NAZ – red square in (a). Note that individual trajectories are disordered. (c) The same system as in (a) at a later time and $v_3 = 7.5$. Note that the system fractures along lines with high D^2_Ω; the crack nucleates at a spot on the surface, shown by the red arrow in (a), where D^2_Ω is particularly large.

these NAZs does not reduce stress. Indeed, the stress continues to increase, being set by the order parameter strain, and eventually the crystal fractures as shown in fig. 7.24(c). Examination of the fracture surface shows that the solid breaks apart precisely along regions of large D^2_Ω, so the NAZs provide seeds for the heterogenous nucleation of cracks. In essence, therefore, microstructural reversibility in martensites is related to the nature of the accompanying plastic deformation.

It is now easy to understand why shape recovery is restored for smaller and stiffer solids. Since NAZs are produced when the local stress increases beyond a threshold, the average distance between NAZs is determined by the statistics of the stress threshold and of the local stress. In general, one expects NAZs to be separated by some average length scale l_c determined by the yield strength of the material, with stiffer materials having larger l_c. It may thus be possible to avoid order parameter strain induced NAZs completely, either by reducing the system size or by increasing l_c by making the material stronger.

7.6 Summary and conclusion

In this chapter we have studied and analysed the possibility of reversible shape changes in martensitic transformations. The model solid of our study undergoes a structural transition from a square to either a rhombic (*i.e.* $p4mm \rightarrow p2$) or triangular (*i.e.* $p4mm \rightarrow p6$) phase. Examination of the regions of plasticity during the transformation helps to infer the necessary and sufficient conditions for shape recovery. Hence we conclude that the dynamics of the NAZs are responsible for determining shape recovery. We find that in agreement with [43], reversibility is obtained when there is a group-subgroup relationship between the parent and the product phases. This is because reversible NAZs are formed related to the slaved non-order parameter strains. For irreversible transformations with no group-subgroup relationship between the parent and product lattices, plastic zones are formed associated with the order parameter strains. Only when the size of the system is smaller than the typical distance between the NAZs, reversibility conditions are restored. We believe that our work has relevance to applications of real martensites [19, 8] as well as the general question of phase ordering dynamics of solid state transformations.

Bibliography

[1] R. Phillips, *Crystals, Defects and Microstructures: Modeling Across Scales*, (Cambridge University Press, Cambridge, 2001).

[2] R. W. Cahn and J. Haasen, *Physical Metallurgy*, 4^{th} Edition, (Elsevier, Amsterdam, 1996).

[3] K. Bhattacharya, *Microstructure of martensite. Why it forms and how it gives rise to the shape-memory effect*, (Oxford University Press, 2003).

[4] Z. Nishiyama, *Martensitic Transformation*, (Academic Press, New York, 1978).

[5] L. E. Tanner, A. R. Pelton and R. Gronsky, J. Phys. (Paris) Colloq. **43**, C4-169 (1982).

[6] R. Oshima, M. Sugiyama and F. E. Fujita, Metall. Trans. A **19**, 803 (1988).

[7] *Shape Memory Effect in Alloys*, edited by J.Perkins, (Plenum, New York, 1975).

[8] A. Roitburd, *Solid State Physics*, ed. Seitz and Turnbull (Academic Press, New York, 1958).

[9] G. R. Barsch and J. A. Krumhansl, Phys. Rev. Lett. **37**, 9328 (1974).

[10] G. S. Bales and R. J. Gooding, Phys. Rev. Lett. **67**, 3412 (1991).

[11] A. C. E. Reed and R. J. Gooding, Phys. Rev. B **50**, 3588 (1994).

[12] B. P. van Zyl and R. J. Gooding, http://xxx.lanl.gov/archive/cond-mat/9602109.

[13] *Metals Handbook*, 9th Edition, Vol. 4 (ASM, Ohio, 1981).

[14] M. Rao and S. Sengupta, http://xxx.lanl.gov/archive/cond-mat/9709022.

[15] M. Rao and S. Sengupta, Phys. Rev. Lett **78**, 2168 (1997).

[16] M. Rao, S. Sengupta and H. K. Sahu, Phys. Rev. Lett **75**, 2164 (1995).

[17] E. Ben-Naim and P. Krapivsky, Phys. Rev. Lett **76**, 3234 (1996).

[18] M. Rao and S. Sengupta, Phys. Rev. Lett **76**, 3235 (1996).

[19] G. B. Olson and W. S. Owen (ed), *Martensite*, (ASM International, Materials Park, OH, 1992).

[20] J. M. Ball and R. D. James, Arch. Rat. Mech. Anal. **100**, 13 (1987).

[21] J. M. Ball and R. D. James, Phil. Trans. Roy. Soc. London A **338**, 389 (1992).

[22] G. R. Barsch, B. Horovitz and J. A. Krumhansl, Phys. Rev. Lett. **59**, 1251 (1987).

[23] K. ø. Rasmussen, T. Lookman, A. Saxena, A. R. Bishop, R. C. Albers and S. R. Shenoy, Phys. Rev. Lett **87**, 055704 (2001).

[24] T. Lookman, S. R. Shenoy, K. ø. Rasmussen, A. Saxena and A. R. Bishop, Phys. Rev. B **67**, 024114 (2003), and references therein.

[25] R. Ahluwalia and G. Ananthakrishna, Phys. Rev. Lett. **86**, 4076 (2001).

[26] S. Sreekala and G. Ananthakrishna, Phys. Rev. Lett. **90**, 135501 (2003).

[27] S. Sreekala, R. Ahluwalia and G. Ananthakrishna, Phys. Rev. B **70**, 224105 (2004).

[28] P. Boullay, D. Schryvers and J. M. Ball, Acta. Mater. **51**, 1421 (2003).

[29] D. Schryvers, P. Boullay, P. L. Potapov, R. V. Kohn and J. M. Ball, Int. J. of Solids and Structures, **39**, 3543 (2002).

[30] J. M. Ball and D. Schryvers, J. de Physique IV, **112**, 159 (2003).

[31] M. Rao, M. and S. Sengupta, Curr. Sc. **77**, 382 (1999)

[32] S. Sengupta and M. Rao, Physica (Amsterdam) **318A**, 251 (2003).

[33] M. Rao and S. Sengupta, Phys. Rev. Lett. **91**, 045502 (2003).

[34] M. Rao and S. Sengupta, J. Phys: Condens. Mat. **16**, 7733 (2004).

[35] V. A. Lubarda, *Elastoplastic theory*, (CRC Press, Boca Raton 2002).

[36] J. Lubliner, *Plastic Theory*, (Macmillan Publishing Co., New York, 1990).

[37] M. L. Falk and J. S. Langer, Phys. Rev. E **57**, 7192 (1998).

[38] J. S. Langer, Phys. Rev. E **64**, 011504 (2001).

[39] J. S. Langer and L. Pechenik, Phys. Rev. E **68**, 061507 (2003).

[40] A. Lemaître, Phys. Rev. Lett. **89**, 195503 (2002).

[41] L. O. Hedges, R. L. Jack, J. P. Garrahan and D. Chandler, Science **323**, 1309 (2009).

[42] M. Merolle, J. P. Garrahan and D. Chandler, Proc. Natl. Acad. Sci. U.S.A. **102**, 10837 (2005).

[43] K. Bhattacharya, S. Conti, G. Zanzotto and J. Zimmer, Nature, **428**, 55 (2004).

[44] C. Ghatak and K.G. Ayappa, Phys. Rev. E **64**, 051507 (2001).

[45] K.G. Ayappa and C. Ghatak, J. Chem. Phys. **117**, 5373 (2002).

[46] M. Schmidt and H. Löwen, Phys. Rev. E **55**, 7228 (1997).

[47] A. Fortini and M. Dijkstra, J. Phys.: Condens. Matter **18**, L371 (2006).

[48] A.H. Marcus and S.A. Rice, Phys. Rev. E **55**, 637 (1996).

[49] C. D. Dewhurst, S. J. Levett, and D. McK. Paul, Phys. Rev. B **72**, 014542 (2005).

[50] L. Ya. Vinnikov, T. L. Barkov, P. C. Canfield, S. L. Bud'ko, J. E. Ostenson, F. D. Laabs and V. G. Kogan, Phys. Rev. B **64**, 220508 (2001).

[51] B. Rosenstein, B. Ya. Shapiro, I. Shapiro, Y. Bruckental, A. Shaulov and Y. Yeshurun, Phys. Rev. B **72**, 144512 (2005).

[52] S. P. Brown, D. Charalambous, E. C. Jones, E. M. Forgan, P. G. Kealey, A. Erb and J. Kohlbrecher, Phys. Rev. Lett. **92**, 067004 (2004).

[53] R. Gilardi, J. Mesot, S. P. Brown, E. M. Forgan, A. Drew, S. L. Lee, R. Cubitt, C. D. Dewhurst, T. Uefuji and K. Yamada, Phys. Rev. Lett. **93**, 217001 (2004).

[54] M. Rao, S. Sengupta, and R. Shankar, Phys. Rev. Lett. **79**, 3998, (1997).

[55] M. F. Laguna, P. S. Cornaglia, and A. A. Aligia, Phys. Rev. B **69**, 104524 (2004).

[56] S. Sankararaman and R. Shankar, Phys. Rev. B **67** 245102 (2003).

[57] W. Wen, L. Zhang, and P. Sheng, Phys. Rev. Lett. **85**, 5464 (2000).

[58] A. Yethiraj and A. van Blaaderen, Nature **421**, 513 (2003).

[59] A. Yethiraj, A. Wouterse, B. Groh and A. van Blaaderen, Phys. Rev. Lett. **92**, 058301 (2004).

[60] T. V. Ramakrishnan and M. Yussouff, Phys. Rev. B **19**, 2775 (1979).

[61] P. F. Tupper and M. Grant, Euro. Phys. Lett. **81**, 40007 (2008).

[62] T. A. Weber and F. H. Stillinger, Phys. Rev. E **48**, 4351 (1993).

[63] D. Frenkel and B. Smit, *Understanding Molecular Simulations*, 2$^{\text{nd}}$ Edition, (Academic Press, California, 2002).

[64] D. P. Landau and K. Binder, *A Guide to Monte Carlo Simulations in Statistical Physics*, (Cambridge University Press, Cambridge, UK, 2000).

[65] K. Binder and D. W. Heermann, *Monte Carlo Simulation in Statistical Physics*, (Springer-Verlag, Heidelberg, 1988).

[66] M. P. Allen and D. J. Tildesley, *Computer Simulation of Liquids*, (Oxford University Press, New York, 1987).

[67] N. Metropolis, A. W. Rosenbluth, M. N. Rosenbluth, A. N. Teller and E. Teller, J. Chem. Phys. **21**, 1087 (1953).

[68] W. H. Press, S. A. Teukolsky, W. T. Vetterling and B. P. Flannery, *Numerical Recipes in Fortran*, (Cambridge: Cambridge University Press, 1992).

[69] L. D. Landau and E. M. Lifshitz, *Theory of Elasticity*, 3rd Edition, (Oxford: Pergamon, 1986).

[70] P. M. Chaikin and T. C. Lubensky, *Principles of Condensed Matter Physics*, (Cambridge: Cambridge University Press, 1995).

[71] D. M. Hatch, T. Lookman, A. Saxena, and S. R. Shenoy, Phys. Rev. B **68**, 104105 (2003).

[72] J. F. Scott, Rev. Mod. Phys. **46**, 83, (1974).

[73] J. R. Morris and K. M. Ho, Phys. Rev. Lett. **74**, 940 (1995).

[74] S. Kartha, J. A. Krumhansl, J. P. Sethna and L. K. Wickham, Phys. Rev. B **52**, 803 (1995).

[75] J. P. Sethna, S. Kartha, T. Castán and J. A. Krumhansl, Physica Scripta, **T42**, 214 (1992).

[76] S. Kartha, T. Castán, J. A. Krumhansl and J. P. Sethna, Phys. Rev. Lett **67**, 3630 (1991).

[77] J. P. Hansen and I. R. McDonald, *Theory of Simple Liquids*, (London: Academic, 1986).

[78] R. Paul, S. Puri and H. Rieger, Phys. Rev. E **71**, 061109 (2005).

[79] J. Q. Broughton, G. H. Gilmer and J. D. Weeks, Phys. Rev. B **25**, 4651 (1982).

[80] H.K.D.H. Bhadeshia, *Bainite in steels*, (Institute of Materials, London, 1992).

[81] A. Heymann, A. Stipp, C. Sinn and T. Palberg, J. Coll., Int. Sc. **207**, 119127 (1998).

[82] J. Liu and T. Palberg, Progr. Colloid Polym. Sci. **123**, 222226 (2004).

[83] J. W. Cahn and J. E. Hilliard, J. Chem. Phys **28**, 258 (1957). (Academic

[84] A. G. Kachaturyan, *Theory of Structural Transformations in Solids*, (Wiley, New York, 1983).

[85] J. Bhattacharya, A. Paul, S. Sengupta, M. Rao, J. Phys: Condens. Mat. **20**, 365210 (2008).

[86] S. F. Edwards and D. V. Grinev,*Jamming and rheology*, Eds. A. Liu and S. R. Nagel (Taylor and Francis, New York, 2001)

[87] A. J. Liu and S. R. Nagel, Nature **396**, 21 (1998).

[88] A. Paul, J. Bhattacharya, S. Sengupta, M. Rao, J. Phys: Condens. Mat. **20**, 365211 (2008).

[89] J. Bhattacharya, S. Sengupta and M. Rao, J. Stat. Mech.: Theory and experiment **P06003** (2008).

[90] J. S. Langer, Phys. Rev. E **77**, 021502 (2008).

[91] A. Zippelius, B. I. Halperin and D. R. Nelson, Phys. Rev. B **22**, 2514 (1980).

[92] M. Abramovitz and I. A. Stegun, *Handbook of Mathematical Functions*, (Dover publications, New York, 1972).

[93] C. E. Maloney and A. Lemaî̂tre, Phys. Rev. E. **74**, 016118 (2006).

[94] J. S. Langer, Phys. Rev. Lett. **97**, 115704 (2006).

[95] F. Lechenault, O. Dauchot, G. Biroli and J. P. Bouchaud, Euro. Phys. Lett. **83**, 46003 (2008).

[96] R. Candelier and O. Dauchot, arXiv:0906.2679 (2009).

[97] J.S Langer In: C Godriche, Editor, *Solid far from Equilibrium*, (Cambridge University Press, Cambridge, UK, 1992).

[98] K. Binder, Rep. Prog. Phys. **50**, 783 (1987).

[99] K. Otsuka and C. M. Wayman, *Shape Memory Materials*, (Cambridge Univ. Press, Cambridge, 1998).

[100] E. K. H. Salje, *Phase Transitions in Ferroelastic and Co-elastic Crystals*, (Cambridge Univ. Press, Cambridge, 1993).

[101] C. P. Poole and F. J. Owens, *Introduction to Nanotechnology*, (Wiley, Hoboken, NJ, 2003).

[102] V. Balzani, M. Venturi, and A. Credi, *Molecular Devices and Machines: A Journey into the Nano World*, (Wiley- VCH, Weinheim, 2003).

[103] J. A. Pelesco and D. H. Bernstein, *Modeling Mems and Nems*, (CRC Press, Boca Raton, 2003).

[104] F-J Pérez-Reche, L. Truskinovsky and G. Zanzotto, Phys. Rev. Lett. **99**, 075501 (2007).

[105] Disintegration of real materials due to internal transformation stresses is well known as for example in http://en.wikipedia.org/wiki/Tin.

[106] D. M. Hatch, T. Lookman, A. Saxena and H. T. Stokes, Phys. Rev. B **64**, 060104(R) (2001).